

UNIVERSITY OF QUEBEC AT CHICOUTIMI

**A DISSERTATION PRESENTED TO THE UNIVERSITY OF
QUEBEC AT CHICOUTIMI IN PARTIAL FULFILLMENT
OF THE REQUIREMENTS FOR THE DOCTOR
OF PHILOSOPHY IN ENGINEERING**

BY

JING LAI

**DEVELOPING SC AND ZR CONTAINING Al-B₄C METAL
MATRIX COMPOSITES FOR HIGH TEMPERATURE
APPLICATIONS**

AUGUST 2011

UNIVERSITE DU QUEBEC A CHICOUTIMI

**THESE PRÉSENTÉ À L'UNIVERSITÉ DU QUÉBEC À
CHICOUTIMI COMME EXIGENCE PARTIELLE DU DOCTORAT
EN INGÉNIERIE**

PAR

JING LAI

**DÉVELOPPEMENT DE COMPOSITE À MATRICE MÉTALLIQUE
AL-B₄C DE TYPE CONTENANT SC ET ZR POUR DES
APPLICATIONS À HAUTE TEMPÉRATURE**

AOÛT 2011

RÉSUMÉ

Dans cette étude, nous nous intéressons principalement au développement de la coulée, et au durcissement structural des composites à matrice métallique Al-B₄C pour des applications à haute température. Le scandium et le zirconium ont été introduits dans le système Al-B₄C, comme éléments d'alliage, et leurs effets sur la microstructure, la réponse au vieillissement, les propriétés mécaniques et la stabilité thermique ont été étudiés.

Afin de réaliser cette étude, un microscope optique, un microscope électronique à balayage et un microscope électronique à transmission ont été utilisés dans le but d'observer la microstructure de brut de coulée et celle obtenue après vieillissement, d'analyser les réactions interfaciales, la distribution des éléments d'alliage entre l'interface et la matrice ainsi que pour examiner l'évolution des précipités lors de la coulée et le vieillissement.

La réponse au vieillissement et le durcissement structural de la matrice ont été suivis par des mesures de dureté 'Vickers'. Les propriétés mécaniques et la stabilité thermique à long terme des composites contenant Sc et Zr ont été évaluées en utilisant des essais de dureté Vickers et Rockwell ainsi que des essais de compression.

Dans le premier chapitre de cette étude, des plaques de B₄C ont été immergées dans l'aluminium liquide contenant Sc, Zr et Ti afin d'étudier les réactions interfaciales entre B₄C et l'aluminium liquide. Les effets de Sc, Zr et Ti à l'interface en terme d'apports individuels et combinés ont été examinés. Les résultats montrent que les trois éléments réagissent avec B₄C et forment des couches interfaciales, qui agissent comme des barrières de diffusion, dans le but de limiter la décomposition du B₄C dans l'aluminium liquide. Ainsi, les réactions interfaciales et les produits de réaction dans chaque système ont été identifiés. En combinant le Sc, Zr et Ti, une grande quantité de Ti est enrichie à l'interface, qui non seulement offre une protection appropriée au B₄C mais aussi une réduction de la consommation de Sc et Zr à l'interface.

Dans le second chapitre, le scandium et le zirconium ont été introduits dans le composite Al-15vol.% B₄C, présaturé par Ti et huit composites à différents teneurs en Sc et Zr ont été préparés par coulée conventionnelle. Il a été constaté que le scandium favorise les réactions interfaciales avec B₄C qui consomme partiellement le Sc. L'ajout de Sc procure un durcissement structural considérable dans les conditions de coulée conventionnelle et du pic de vieillissement. Afin d'obtenir un durcissement équivalent de Sc dans les alliages binaires, environ le double de la quantité de Sc est nécessaire pour les composites Al-B₄C. Par contre, aucun produit de réaction majeur de Zr n'a été trouvé aux interfaces. En effet, la majeure partie de Zr se concentre dans la matrice pour le durcissement structural. La combinaison de Sc et Zr augmente de manière significative le durcissement structural. Deux types de précipités nanométriques, Al₃Sc et Al₃(Sc, Zr), ont été observés dans la

microstructure obtenue après coulée, qui contribue à une augmentation significative de la dureté de la matrice.

Dans le troisième chapitre, les composites à différentes teneurs en Sc et Zr ont été vieillies en condition isotherme à 300, 350, 400 et 450 °C après homogénéisation/mise en solution. Les résultats démontrent que l'ajout de Sc induit un durcissement par précipitation considérable à la matrice des composites, pour toutes les températures de vieillissement appliquées. L'effet du durcissement par précipitation augmente avec l'augmentation de la quantité de Sc et diminue lorsque la température de vieillissement est surélevée. La combinaison des éléments d'alliage Zr et Sc dans les composites Al-B₄C produit un effet synergique.

L'addition de Zr fournit non seulement une augmentation de la résistance mécanique au pic de vieillissement mais aussi une amélioration de la stabilité thermique. Les composites ayant un rapport Zr:Sc élevé (≥ 1) présentent une excellente stabilité thermique de la résistance mécanique jusqu'à 400 °C. Le survieillessement est retardé d'environ ~ 100 °C par rapport aux composites sans Zr pour la même teneur en Sc. La fraction volumique de précipités, le rayon moyen et la distribution de la taille des précipités nanométriques Al₃Sc et Al₃(Sc,Zr) ont été mesurés au cours du processus de vieillissement. Les précipités Al₃(Sc,Zr) montrent généralement une résistance au grossissement bien meilleure que celle des précipités Al₃Sc. Il est également confirmé que le contournement d'Orowan est le principal mécanisme qui contrôle le durcissement par précipitation des deux précipités.

Dans le quatrième chapitre, deux composites contenant chacun 0.4% Sc et 0.4% plus 0.24 % Zr ont été élaborés pour examiner leurs propriétés mécaniques au cours d'une exposition de longue durée (2000h) à des températures élevées, allant de 250 à 350 °C. Ainsi, pour une stabilité thermique prolongée, les propriétés mécaniques du composite contenant Sc et Zr sont stables jusqu'à 300 °C, pendant que le composite contenant uniquement Sc montre une bonne résistance à l'adoucissement jusqu'à 250 °C. Pour des températures élevées la résistance mécanique des deux composites diminue en fonction du recuit prolongé. La dégradation des propriétés mécaniques des composites pendant une longue période de recuit et à haute température est dominée par le grossissement des précipités.

Enfin, deux composites contenant chacun 0.58 % Sc et 0.58 % Sc plus 0.24 % Zr, ont été laminés à chaud jusqu'à une épaisseur de 2 mm avec une réduction totale de 93%. Les résultats montrent que les composites contenant Sc et Zr possèdent une bonne aptitude à la mise en forme par laminage à chaud. La réponse au vieillissement et au renforcement par précipitation au cours des traitements thermiques subits après laminage ont été examinés et l'impact des paramètres sur le durcissement par vieillissement a été défini.

ABSTRACT

The study presented in this thesis focuses on developing castable, precipitation-strengthened Al–B₄C metal matrix composites (MMCs) for high temperature applications. Scandium and zirconium, as effective alloying elements, were introduced into the Al–B₄C system and their effect on the microstructure, aging response, mechanical properties and thermal stability was investigated.

In this study, an optical microscope, a scanning electron microscope and a transmission electron microscope were used to observe the as-cast and aged alloy microstructures and to analyze the interfacial reactions and the distribution of alloying elements between the interface and the matrix. The evolution of precipitates during casting and aging was also examined. The aging response and precipitation strengthening of the matrix were monitored by the Vickers hardness measurements. Mechanical properties and long-term thermal stability of composites containing Sc and Zr were evaluated using Vickers and Rockwell hardness tests as well as compression tests. The results of the present thesis are divided into five parts.

In the first part, B₄C plates were immersed in liquid aluminum alloyed with Sc, Zr and Ti to investigate the interfacial reactions between B₄C and liquid aluminum. The influences of Sc, Zr and Ti on the interfacial microstructure in terms of individual and combined additions were examined. Results reveal that all three elements reacted with B₄C and formed interfacial layers that acted as a diffusion barrier to limit the decomposition of B₄C in liquid aluminum. The interfacial reactions and the reaction products in each system were identified. With the combined addition of Sc, Zr and Ti, most of the Ti was found to enrich at the interface, which not only offered appropriate protection of the B₄C but also reduced the consumption of Sc and Zr at the interface.

In the second part, Sc and Zr were introduced into Al–15vol.% B₄C composites presaturated by Ti, and eight experimental composites with different Sc and Zr levels were prepared via a conventional casting technique. It was found that Sc was involved in the interfacial reactions with B₄C that partially consume Sc. The Sc addition yielded considerable precipitation strengthening in the as-cast and peak aged conditions. To achieve an equivalent strengthening effect of Sc in binary Al–Sc alloys, approximately double the amount of Sc is required in Al–B₄C composites. On the contrary, no major Zr reaction products were found at the interfaces and the major part of Zr remained in the

matrix for the precipitation strengthening. The combination of Sc and Zr enhanced the precipitation strengthening. Two kinds of nanoscale precipitates, Al_3Sc and $\text{Al}_3(\text{Sc}, \text{Zr})$, were found in the as-cast microstructure and contributed to the increase in the matrix hardness.

In the third part, all the experimental composites were isothermally aged at 300, 350, 400 and 450 °C after a homogenization/solution treatment. Results demonstrate that the addition of Sc generated a considerable precipitation hardening of the matrix of the composites for all aging temperatures applied. The precipitation hardening effect increased when increasing the Sc content and decreased with increase in aging temperature. The combination of alloying Sc and Zr in Al-B₄C composites produced a remarkable synergistic effect. The addition of Zr provided not only a strength increase at peak aging but also an improvement of thermal stability. The composites with a high Zr:Sc ratio (≥ 1) showed excellent thermal stability of the strength up to 400°C. The overaging in these materials was delayed by ~100°C compared with the Zr-free composites at the same Sc level. The precipitate volume fraction, the average radius and the size distribution of nanoscale Al_3Sc and $\text{Al}_3(\text{Sc}, \text{Zr})$ precipitates during the aging process were measured. The $\text{Al}_3(\text{Sc}, \text{Zr})$ precipitates generally showed a much better coarsening resistance than the Al_3Sc precipitates. It was also confirmed that Orowan bypassing is the main controlling mechanism for the precipitation hardening of both precipitates types.

In the fourth part, two experimental composites with 0.4wt.% Sc and 0.4wt.% Sc plus 0.24wt.% Zr were selected to examine the mechanical properties during long-term exposure (2000h) at elevated temperatures from 250 to 350°C. For long-term thermal stability, the mechanical properties of the Sc and Zr containing composite were stable up to 300°C, while the composite containing only Sc exhibited a good softening resistance up to 250°C. At higher temperatures the strengths of both composites decreased with prolonged annealing time. The reduction of the composites' mechanical properties during long-time annealing at higher temperatures was dominated by the precipitate coarsening.

Finally, two experimental composites with 0.58wt.% Sc and 0.58wt.% Sc plus 0.24wt.% Zr, were respectively hot-rolled to a 2 mm thick sheet with a total reduction of 93%. Results indicate that the Sc- and Zr-containing composites possessed a good hot rolling processability. The aging response and precipitation strengthening in the post-rolling heat treatment were examined and the impact of the solution parameters on age hardening are outlined.

ACKNOWLEDGEMENTS

This research would not have been possible without the guidance of my thesis advisors, Profs. X-Grant. Chen, and Z. Zhang. I would like to express my deepest respect and gratitude for their scientific guidance, their trust and support all along the path.

Many thanks to my colleagues for their insight, scientific discussions, and time (in alphabetical order): Emad Elgallad, Jeffrey Guo, Yu-Mei Han, Gao Feng Li, Kun Liu, Jian Qin, Cang-ji Shi, Peng Shen. Special thanks to Mehand Tebib for providing support of French language. I especially thank Martin Bouchard, Émélie Brideau, and Dany Racine, for their assistance with the casting, sample preparation and data analysis.

Thanks also to all my friends I met in Chicoutimi for long-time encouragement and support. Warm wishes to my parents and my whole family for their unending love and trust throughout my education. Finally, this thesis is dedicated to Kai, for putting up with me and standing by my side all the time.

This research was supported by the Natural Sciences and Engineering Research Council of Canada (NSERC) and Rio Tinto Alcan.

PUBLICATIONS

In the current Ph.D. work, eight publications in the form of journal articles, conference papers and posters were prepared. Full details are provided below.

I. Peer-Reviewed Journal Articles

1. **Jing Lai**, Zhang Zhan, X. Grant Chen, “Effect of Sc, Zr and Ti on the interfacial reactions of the B_4C/Al system”, *Journal of Material Science*, 2011, **46** (2): 451-459.
2. **Jing Lai**, Zhang Zhan, X. Grant Chen, “Microstructure and precipitation strengthening of Al- B_4C metal matrix composites alloyed with Sc and Zr: Part I - As-cast microstructure and precipitation evolution”, Prepared for Submission.
3. **Jing Lai**, Zhang Zhan, X. Grant Chen, “Microstructure and precipitation strengthening of Al- B_4C metal matrix composites alloyed with Sc and Zr: Part II - Precipitation strengthening during isothermal aging at 300–450°C”, Prepared for Submission.
4. **Jing Lai**, Zhang Zhan, X. Grant Chen, “The thermal stability of mechanical properties of Al- B_4C composites alloyed with Sc and Zr at elevated temperatures”, Prepared for Submission.

II. Conference Presentations / Proceedings

5. **Jing Lai**, Zhang Zhan, X. Grant Chen, “Effect of Sc and Zr Addition on Strengthening of Al- B_4C Composites at Elevated Temperatures”, in *Proceedings of Material Science & Technology 2009 (MS&T'09) Conference*, Pittsburgh, PA, USA, October 25–29, 2009, pp.1898-1907.

III. Scientific Posters

6. **Jing Lai**, Zhang Zhan, X. Grant Chen, “Thermal stability of Al- B_4C composites alloying with Sc and Zr at Elevated Temperatures”, *The Encyclopaedia of Research on Aluminium in Quebec – 2010 Edition*, Les Presses de l’aluminium, p. 48.
7. **Jing Lai**, Zhang Zhan, X. Grant Chen, “Effect of Sc and Zr Addition on Strengthening of Al- B_4C Composites at Elevated Temperatures”, *The*

Encyclopaedia of Research on Aluminium in Quebec – 2009 Edition, Les Presses de l'aluminium, p. 49.

8. **Jing Lai**, Zhang Zhan, X. Grant Chen “The effect of Sc, Zr, and Ti on the interface of Al/B₄C couples”, The Encyclopaedia of Research on Aluminium in Quebec – 2008 Edition, Les Presses de l'aluminium, p. 24.

TABLE OF CONTENTS

RÉSUMÉ.....	i
ABSTRACT	iii
ACKNOWLEDGEMENTS	v
PUBLICATIONS.....	vi
TABLE OF CONTENTS	viii
LIST OF SYMBOLS	xii
LIST OF FIGURES	xv
LIST OF TABLES.....	xxi
Chapter 1	
Introduction	2
1.1 Background	2
1.2 Objectives.....	5
Chapter 2	
Literature review	9
2.1 General strengthening requirements for thermally stable composites.....	10
2.1.1 Strengthening mechanisms in MMCs.....	10
2.1.2 General strengthening mechanism of Al matrix.....	11
2.1.3 Precipitate coarsening theory	18
2.1.4 Requirement for high temperature MMCs.....	19
2.2 Thermal stability of matrix alloys.....	20
2.2.1 Selection of matrix alloys.....	20
2.2.2 Al–Sc binary alloys.....	21
2.2.3 Al–Sc–Zr ternary alloys	27
2.2.4 The influence of titanium.....	32

2.3 Al–B ₄ C composites.....	33
2.3.1 Al-matrix composites.....	33
2.3.2 B ₄ C reinforcement	34
2.3.3 Matrix/reinforcement interface in Al–B ₄ C composites	35
2.3.4 Properties of Al–B ₄ C composites.....	40

Chapter 3

Experimental.....	43
3.1 Experimental composite design and sample preparation.....	43
3.1.1 Al/B ₄ C couples	43
3.1.2 Al–B ₄ C composites.....	45
3.2 Heat treatment	47
3.2.1 Aging for precipitation-strengthening	48
3.2.2 Long time annealing	49
3.2.3 Post-rolling heat treatment	50
3.3 Microstructure observation	50
3.3.1 Optical microscopy.....	50
3.3.2 Scanning electron microscopy (SEM)	51
3.3.3 Electron backscatter diffraction (EBSD)	51
3.3.4 Transmission electron microscopy (TEM).....	52
3.4 Evaluation of mechanical properties.....	53
3.4.1 Hardness.....	53
3.4.2 Compression test.....	53
3.5 Hot rolling process.....	54

Chapter 4

Effect of Sc, Zr and Ti on the interfacial reactions.....	57
4.1 Introduction	57
4.2 Results.....	58
4.2.1 Morphology and type of interfacial layers.....	58
4.2.2 Interfacial microstructure of B ₄ C/Al–Sc alloy	62
4.2.3 Interfacial microstructure of B ₄ C/Al–Zr alloy	65
4.2.4 Interfacial microstructure of B ₄ C/Al–Ti alloy	66
4.2.5 Interfacial microstructure of B ₄ C/Al–Sc–Zr–Ti alloy	67

4.3 Discussion	70
4.4 Summary	74
 Chapter 5	
As-cast microstructure and precipitation evolution	77
5.1 Introduction	77
5.2 Results	78
5.2.1 Microstructure of prefabricated material	78
5.2.2 Microstructures of as-cast composites	79
5.2.3 Precipitation strengthening.....	90
5.3 Discussion	92
5.3.1 Interfacial reactions.....	92
5.3.2 Solute concentration of Sc and Zr in the matrix.....	94
5.3.3 Precipitation strengthening in as-cast condition.....	96
5.4 Summary	98
 Chapter 6	
Precipitation strengthening during isothermal aging at 300 – 450 °C.....	101
6.1 Introduction	101
6.2 Results.....	102
6.2.1 Age hardening response	102
6.2.2 Evolution of precipitates	109
6.3 Discussion	115
6.4 Summary	122
 Chapter 7	
Thermal stability of mechanical properties at elevated temperature	125
7.1 Introduction	125
7.2 Results.....	127
7.2.1 Age hardening response	127
7.2.2 Long time annealing	130
7.2.3 Microstructural analysis.....	136
7.3 Discussion	142
7.3.1 Effect of the grain size on mechanical properties.....	142

7.3.2 Effect of the interfaces on mechanical properties	143
7.3.3 Effect of precipitate coarsening on mechanical properties	144
7.4 Summary	146
 Chapter 8	
Hot rolling of Sc and Zr containing composites and the post-rolling heat treatment	149
8.1 Introduction	149
8.2 Results	150
8.2.1 The hot rolling processability of composites	150
8.2.2 Microhardness of hot-rolled composites	150
8.2.3 Influence of the post-rolling heat treatment on the microhardness of hot-rolled composites	151
8.2.4 Microstructural evolution	156
8.3 Discussion	159
8.4 Summary	160
 Chapter 9	
Conclusions and Suggestions for future work	162
9.1 Conclusions	162
9.2 Suggestions for future work	166
Appendix A	170
Appendix B	172
REFERENCES	174

LIST OF SYMBOLS

a, c :	Lattice parameter
b :	Burgers vector
C :	Concentration of specific element in the matrix (Al)
D :	Diffusion coefficient
d :	Average grain size
ε, δ :	Lattice parameter misfit
G :	Shear modulus
ΔG_i :	Gibbs formation energy of the compound i
Γ :	Line tension of a dislocation
γ_s :	Energy of a matrix-precipitate interface
γ_{APB} :	Anti-phase boundary energy
γ_m :	Stacking-fault energy of the matrix
γ_p :	Stacking-fault energy of the precipitates
$\Delta\gamma$:	$ \gamma_p - \gamma_m $
H :	Microhardness value
θ :	Contact angle
k :	A coarsening rate constant
k_{PH} :	A constant representing the relative hardening contribution of the grain boundaries

κ :	Boltzman constant
L_{p-p} :	Inter precipitate spacing
M :	Taylor mean orientation factor
m, χ :	Dimensionless constants
n :	Time exponent for coarsening
ν :	Poisson's ratio
r :	Precipitate radius
\bar{r}_0 :	Initial mean precipitate radius
\bar{r}_t :	Mean precipitate radius at a specific time
$\langle r \rangle$:	Average radius of precipitate
R :	Mean radius of a circular cross section in a random plane for a spherical precipitate
σ :	Flow stress
σ_0 :	Original yield stress
σ_m :	Stress of matrix
σ_p :	Stress of precipitates
$\Delta\sigma_{cs}$:	Stress of coherency strengthening
$\Delta\sigma_{ms}$:	Stress of modulus strengthening
$\Delta\sigma_{om}$:	Orowan stress
$\Delta\sigma_{os}$:	Stress of order strengthening

$\Delta\sigma_{PH}$: Increment of yield stress caused by the change of grain size

$\Delta\sigma_{ps}$: Peierls stress

T : Absolute temperature

t : Time

Vp : Precipitate volume fraction

LIST OF FIGURES

Figure	Title	Page
2.1	Al–Sc binary phase diagram [89].	22
2.2	Change in microhardness of binary Al–Sc alloys reported in literature with different scandium contents during an isothermal hold at 300 °C [18, 19, 21, 84, 104-110].	26
2.3	Microhardness of a 134 mm diameter Al–0.41wt.% Sc alloy ingot vs. annealing time at various temperatures [78].	26
2.4	Polythermal section of the Al–Sc–Zr phase diagram from Al–0.4 wt.% Sc to Al–0.8 wt.%Zr [115].	28
2.5	Polythermal section of the Al–Sc–Zr phase diagram from Al–0.4 wt.% Sc to Al–0.8 wt.%Zr [11].	29
2.6	Relationship of the microhardness of billets of Al–0.4wt.% Sc (□) and Al–0.4wt.% Sc–0.15wt.% Zr (○) alloys to annealing time at 350°C (redrawn from Ref [84]).	31
2.7	Kinetics of the variation of microhardness of Al–0.2wt.% Sc(○) and Al–0.2wt.%Sc–0.15 wt.%Zr (●) alloys in annealing at 400°C a and 450°C b (redrawn form Ref [111]).	31
2.8	Schematics of a stirring technique, and b solidification process in particulate composites [135].	36
3.1	Schematic diagram of the experiment set-up.	45
3.2	The electric resistance furnace used for casting.	47
3.3	STANAT CX–100 laboratory scale rolling mill used for rolling.	55
3.4	The original rectangular cast a and the final rolling sheet b .	55
4.1	SEM micrographs of the deep-etched samples revealing the morphology of the interface after 10 hours reaction time: a B ₄ C/Al–0.3Sc, b B ₄ C/Al–0.3Ti, c B ₄ C/Al–0.3Zr, and d B ₄ C/Al–0.3Sc–0.3Zr–0.3Ti. e Schematic diagram illustrating	59

- interfacial layers.
- 4.2 SEM images showing the interfacial layers at different reaction times: **a** 2 hours and **b** 10 hours in $B_4C/Al-Ti$ system; **c** 2 hours and **d** 10 hours in $B_4C/Al-Zr$ system. 61
- 4.3 The thickness evolution of the fine crystal layer in different alloy systems after 2 and 10 hours reaction times. 61
- 4.4 **a** Bright-field STEM image of interfacial layers in Sc-containing $Al-B_4C$ couple, **b** EDS line scan of Al, Sc, B and C along the arrow in **a**, **c** SAED ring pattern from selected area I: 1, $Al_3BC(101)$; 2, $Al_3BC(102)$; 3, $Al_3BC(001)$; 4, $B_4C(104)$, **d** SAED ring pattern from selected area II: 1, $ScB_2(110)$; 2, $ScB_2(100)$; 3, $ScB_2(201)$; 4, $ScB_2(211)$; 5, $Al_3BC(116)$; 6, $Al_3BC(203)$; 7, $Al_3BC(101)$; 8, $Al_3BC(104)$; 9, $Al_3BC(112)$; 10, $Al_3ScC_3(004)$; 11, $Al_3ScC_3(002)$; **e-f** Al_3ScC_3 phase electron diffraction patterns corresponding to the selected area III at the respective zone axes $[2\bar{1}\bar{1}0]$ and $[1\bar{1}00]$; **g-i** ScB_2 phase electron diffraction patterns from the selected area IV at the respective zone axes $[000\bar{1}]$, $[11\bar{2}\bar{6}]$ and $[01\bar{1}4]$. 64
- 4.5 **a** Dark-field STEM image of interfacial layers in Zr-containing $Al-B_4C$ couple, **b** EDS line scan of Al, B, C, Zr along the arrow indicated in **a**, **c** SAED ring pattern from region I showing: polycrystalline Al_3BC : 1, (101); 2, (102); 3, (103), **d** SAED ring pattern from region II: 1, Al (200); 2, $ZrB_2(102)$; 3, $ZrB_2(200)$; 4, $ZrB_2(211)$, 5, $ZrB_2(104)$, **e-g** ZrB_2 electron diffraction patterns corresponding to the selected area III at the respective zone axes of $[22\bar{4}3]$, $[11\bar{2}1]$, and $[25\bar{7}6]$. 66
- 4.6 **a** SEM image of interfacial layer of $B_4C/Al-Ti$ couple. **b** EDS line profiles showing major element distributions along the white arrow in **a**. 67
- 4.7 **a** Bright-field STEM image of interfacial layers in Sc, Zr, and Ti containing $Al-B_4C$ couple, **b** EDS line scan of Al, B, C, Sc, Zr, and Ti along the arrow indicated in **a**, **c** SAED ring pattern from region I showing polycrystalline Al_3BC : 1, (101); 2, (105); 3, (103); 4, (110), **d** SAED ring pattern from region II showing polycrystalline Al_3BC and TiB_2 : 1, $TiB_2(101)$; 2, $Al_3BC(110)$; 3, $TiB_2(201)$; 4, $Al_3BC(201)$, **e-g** TiB_2 electron diffraction patterns corresponding to the selected area III at the 69

- respective zone axes of $[01\bar{1}0]$, $[\bar{2}13\bar{1}13]$, and $[\bar{1}5\bar{4}0]$.
- 5.1 Optical micrographs of prefabricated AA1100–25 vol. % B₄C with 2.0 wt. %Ti cast billets. 79
- 5.2 Optical microstructures of as-cast composite samples: S58 (**a** and **b**), S40 (**c** and **d**), and S29 (**e** and **f**). 80
- 5.3 Optical microstructures of as-cast composite samples of SZ58 (**a** and **b**), SZ40 (**c** and **d**), S29 (**e** and **f**) and Z24 (**g** and **h**). The arrows in **a**, **c**, **e** and **g** show the primary Al₃Zr intermetallic particles. 81
- 5.4 SEM micrographs of S58: **a** light-etched, **b** deep-etched; and SZ58: **c** light-etched and **d** deep-etched. 83
- 5.5 **a**, **b** Bright-field STEM images of typical interfacial morphologies in as-cast composite S58. **c** Composition profiles along the arrow indicated in **a**. **d** SAED ring pattern from selected area I: 1, ScB₂(100); 2, TiB₂(101); 3, TiB₂(110); 4, TiB₂(201); 5, TiB₂(112); 6, ScB₂(211). **e** TiB₂ phase electron diffraction patterns corresponding to the selected area II at the zone axis $[2\bar{1}\bar{1}0]$; **f** Al₃ScC₃ phase electron diffraction patterns corresponding to the selected area III at the zone axis $[2\bar{1}\bar{1}0]$. 84
- 5.6 **a**, **b** Bright-field STEM images of typical interfacial morphologies in as-cast composite SZ58. **c** Composition profiles along the arrow indicated in **b**. **d** SAED ring pattern from selected area I: 1, TiB₂(001); 2, ScB₂(100); 3, TiB₂(101); 4, TiB₂(002); 5, ScB₂(102); 6, ScB₂(201). **e** TiB₂ phase electron diffraction patterns corresponding to the selected area II at the zone axis $[\bar{1}2\bar{1}0]$. **f** Al₃ScC₃ phase electron diffraction patterns corresponding to the selected area III at the zone axis $[10\bar{2}\bar{8}3]$. 86
- 5.7 Dark-field TEM images showing the precipitates in the matrix of the composites S58 **a** and SZ58 **b** and **c**. 88
- 5.8 A precipitate free zone existed near the grain boundary (S58) using the superlattice reflection (100) of Al₃Sc particles near the $[100]$ zone axis. 89
- 5.9 A precipitate free zone at the interface of the composite S58. **a** bright-field STEM image of the interface; (**b**, **c**, and **d**) enlarged dark-field images of zoom-in areas (squares) in (**a**) taken from locations away from the interface by 4.5 μm, 2.5 90

	μm and 300 nm, respectively.	
5.10	Vickers microhardness of the matrix of experimental composites in as-cast, as-homogenized and peak-aged conditions.	92
5.11	Peak microhardness at 300 °C vs. Sc concentration of experimental composites in comparison with that reported in binary Al–Sc alloys.	95
6.1	Aging curves of the Al–Zr composite (Z24) at 300 and 450°C.	103
6.2	Vickers hardness vs. aging time at: a 300 °C, b 350 °C, c 400 °C and d 450 °C for the three Al–Sc composites.	104
6.3	Vickers hardness vs. aging time at: a 300 °C, b 350 °C, c 400 °C and d 450 °C for the three Al–Sc–Zr composites.	106
6.4	Hardness increment of the peak aging for six Al–Sc and Al–Sc–Zr composites isothermally aged at a 300, b 350, c 400 and d 450° C.	108
6.5	Dark-Field TEM images show the evolution of precipitates in the matrix of the composites S58 (a–c) and SZ58 (d–f) during aging at 450°C for different exposure times. All of the images are taken utilizing (100) superlattice reflections near [011] zone axis.	110
6.6	Precipitate size distributions in the composites S58 (a , c and e) and SZ58 (b , d and f) aged at 450°C for 5min, 10h and 100h.	113
6.7	Distribution of precipitates at the grain boundary and in front of the interface in the composite S58 aged at 450 °C for 5 min: a Superlattice dark-field image illustrating a PFZ with variable widths at the grain boundary (using 100 reflections of precipitates near [011] axis); b STEM image demonstrating particle distribution in front of interface, c Superlattice dark-field image illustrating magnified view of precipitates distribution in the area mark by white square in b .	115
6.8	Average precipitate radii formed in two composites as a function of aging time on a double logarithmic plot at 450 °C.	117
6.9	Microhardness yield stress increment as a function of the average precipitate radius $\langle r \rangle$ for the composite: a S58 ($V_p = 0.20 \%$) and b SZ58 ($V_p = 0.33 \%$). The lines represent the	121

	theoretical predictions of Eqs. (6.1)–(6.5) for $V_p = 0.20$ and 0.33%.	
7.1	Vickers hardness vs. aging time at: a 300 °C, b 350 °C, c 400 °C and d 450 °C for composites SZ40 and S40.	128
7.2	Hardness vs. annealing time. Vickers hardness: a composite SZ40 and c composite S40; Rockwell hardness: c SZ40 and d S40. The initial values of both SZ40 and S40 are from the peak aging at 350 and 300°C for 10h, respectively.	132
7.3	True stress–strain curves of SZ40 from compression tests in different conditions.	133
7.4	Yield and compressive strengths vs. annealing time, a yield strength of SZ40, b compressive strength of SZ40, c yield strength of S40, d compressive strength of S40.	134
7.5	EBSD micrograph of SZ40 composite after: a aging at 350°C for 10 h, b annealing at 350°C for 2000 h.	137
7.6	Optical micrographs of a S40 peak aging, b SZ40 peak aging, c S40 annealing at 300 °C for 2000 h, and d SZ40 annealing at 350 °C for 2000h.	138
7.7	SEM micrographs of composite SZ40 revealing the morphologies of the interfaces and B_4C particles in the condition of: a and b peak aging; c and d annealing at 300°C for 2000h; e and f annealing at 350°C for 2000 h.	140
7.8	TEM dark-field images showing the precipitates in composite SZ40: a upon peak aging , and b after 2000 h annealing at 350°C.	141
7.9	Particle size distributions of $Al_3(Sc,Zr)$ precipitates in composite SZ40: a after peak aging, and b after 2000 h annealing at 350°C. The inset in b shows an enlargement of the PSD in the particle radius range of 10 to 45nm.	141
8.1	Vickers hardness of composite S58 and SZ58 in as-rolled condition and after solution treatment.	152
8.2	Comparison of aging responses of composite S58 and SZ58 at 300 °C prior to and after hot rolling.	152

8.3	Hardness evolution as a function of heat treatment of the as-cast samples of composite S58..	155
8.4	Influence of the solution treatment time on the precipitation strengthening of as-rolled S58 composites.	155
8.5	Optical microstructures of as-rolled composites S58 (a & c) and SZ58 (b & d), showing the distribution of B ₄ C particles and reaction products in the aluminum matrix.	157
8.6	SEM image of as-rolled composite S58 after deep etching.	157
8.7	The observation of precipitates formed in the matrix of composite S58 after rolling: a Bright-field STEM image showing that a large amount of precipitates existed in the matrix of the as-rolled samples. b Dark-field TEM image showing the typical morphology of precipitates in as-rolled condition. c The absence of precipitates after solution treatment at 640°C for 24 h, and d following aging process at 300°C for 10 h.	158

LIST OF TABLES

Table	Title	Page
2.1	Microhardness of the Al ₃ Sc phase [92]	24
2.2	Room temperature mechanical properties of Al-B ₄ C composites	40
3.1	The chemical composition of B ₄ C powder (wt.%)	44
3.2	Chemical compositions of Al alloys used	45
3.3	Nominal chemical compositions of eight model composites	46
3.4	Heat treatment parameters applied in this study	49
3.5	Heat treatment parameters for the long-term annealing	49
3.6	Applied heat treatment parameters for aging-response investigation	50
3.7	Applied heat treatment parameters for solution-treatment investigation	50
5.1	Measured cooling rates of cast ingots from 730 °C to 300 °C	97
6.1	Average radii of precipitates as a function of aging time at 450 °C in two composites (S58 and SZ58)	111
7.1	Grain size of SZ40 in different conditions	137
7.2	Increment of yield stress caused by grain size	142
7.3	Mechanical properties of aluminum and Al-B ₄ C composites at ambient temperature.	144
8.1	Parameters of the heat treatment	151
A.1	Parameter selection for mounting of specimens	170
A.2	Polsihing procedure and parameter	171

B.1	Hot-rolling procedure and parameter
-----	-------------------------------------

173

CHAPTER 1

INTRODUCTION

Chapter 1

Introduction

1.1 Background

Particulate reinforced aluminum metal matrix composites (MMCs) have been widely used for various structural and functional applications in automotive, marine, aerospace and nuclear industries. This is due to their higher specific strength and stiffness, excellent thermal, electrical and wear properties compared to conventional monolithic aluminum alloys [1, 2]. Requirements for a more efficient composite material to be functionalized within unfriendly environments (high temperature and pressure, radioactivity, etc.) constitute the primary driving force for developing advanced aluminum MMCs that can offer enhanced strength at elevated temperatures. One example is to develop high-temperature Al-B₄C composites that are used as neutron absorber materials for the transport and storage of spent nuclear fuels in the nuclear industry [3, 4]. In this application, the Al-B₄C composite materials are placed between the spent fuel assemblies in order to realize neutron absorption, to maintain enough structural strength to support the fuel assemblies, as well as to dissipate the extra heat [5-7]. During the service, absorption of the

thermal neutrons generates heat and increases the temperature, and the Al-B₄C composites may thus experience long-term exposure at elevated temperatures (250 to 350°C) [8]. To improve the performance of the materials and increase the specific storage capacity of spent fuels, it is desirable to maximize the operating temperature while minimizing the overall weight of the storage containers. There is presently a growing interest in the development of lightweight Al-B₄C MMCs to survive under the load of high temperatures, of 300°C or above, and to be thermally stable for long periods of time [4, 8].

It is well known that the strength of aluminum MMCs is primarily derived from the strength of the matrix alloys. However, commercial aluminum MMCs commonly use 2000, 6000 and 7000 series matrix alloys, which have limited strength at elevated temperatures. Their strength degrades quickly as the temperature approaches 300°C due to an overaging effect where rapid coarsening of the strengthening precipitates occurs [9, 10]. Historically, most efforts to develop high-temperature aluminum alloys have been made using non-equilibrium fabrication methods, such as rapid solidification, mechanical alloying, and powder metallurgy, by adding a large amount of low diffusivity alloying elements in Al [11, 12]. These include the Al-Fe based alloys with ternary and quaternary additions of Ni, V, Ce, W, Mo, Cr [13-16]. The high-temperature strength of these alloys is contributed by a large volume fraction of incoherent intermetallics (oftentimes 20 to 30%) [17]. However, none of these alloys have been widely accepted for reasons of affordability and performance.

As an alternative, Al–Sc alloys offer a significant strengthening effect and reasonable stability of mechanical properties up to 300°C. This is due to the formation of a number of hard and coherent Al₃Sc precipitates with an ordered face-centered cubic (L1₂) structure [18-20]. Above this temperature, however, the Al–Sc alloys undergo rapid coarsening of the precipitates, which leads to the weak thermal stability of the alloys [19, 21]. To improve the thermal stability, Zr was introduced into Al–Sc binary alloys. The Al–Sc–Zr alloys show better precipitation strengthening and enhanced stability by forming more stable Al₃(Sc,Zr) precipitates [22-24]. Furthermore, by alloying both elements into the alloy matrix enables the manufacture of composite materials using ingot metallurgy techniques. The conventional ingot metallurgy route for manufacturing the MMCs has several major benefits, from processing, performance, and economical points of view. Therefore, it is considered that Al–Sc and Al–Sc–Zr based matrix are among promising candidates to develop advanced Al–B₄C composites with multiple merits including excellent high-temperature strength, thermal stability, good castability and hot-deformation properties.

During recent years, substantial progress has been made in the development of durable Al–B₄C composites as quality neutron absorber materials via an ingot metallurgy route [5, 6, 25, 26]. It is reported that liquid aluminum has poor wettability on boron carbide, and severe interfacial reactions between B₄C and Al occur during the casting process [25, 27, 28]. A certain amount of Ti is thus added to the composite to prevent the B₄C decomposition by forming an *in-situ* barrier layer of TiB₂ around the B₄C particulate surfaces. This improves the wettability and castability of Al–B₄C composites [25, 29].

Based on the information mentioned above, concepts for alloying Sc, Zr and Ti in the Al–B₄C system to manufacture high-temperature composites are proposed. However, due to the fact that both Sc and Zr are located close to Ti in the periodic table, these three alloying elements are expected to show similar behaviors in aluminum alloys. When Sc and Zr are introduced into the B₄C/Al system, interfacial reactions between the alloying elements and B₄C particles in the liquid aluminum may occur and can affect the capability to form strengthening precipitates in the matrix. Moreover, as a series of new materials, their basic material characteristics, such as the microstructures during casting and heat treatment, aging behavior, mechanical properties and thermal stability, should be examined in detail.

1.2 Objectives

This study focuses on developing the thermally stable Al–B₄C composites which can be applied at elevated temperature for long-term holding. In order to achieve this goal, the following objectives are proposed:

1. Investigate the influence of alloying elements (Sc, Zr and Ti) on the interface reactions between Al–B₄C couples:
 - Verify the interfacial reactions and identify the reaction products at the interface of Al–B₄C couples with the three alloying elements;
 - Analyze the alloying elements and their distribution across the interface of Al–B₄C couples;
 - Evaluate the potential of Sc and Zr for precipitation strengthening in the presence of

Ti;

2. Investigate the microstructures and mechanical properties of Al–B₄C composites alloyed with Sc and Zr in the as-cast condition:
 - Prepare Al–B₄C composites alloyed with Sc, Zr, and Ti;
 - Analyze the interfacial reactions and identify the reaction products;
 - Examine the nature of precipitates formed in the matrix during casting;
 - Analyze the distribution of alloying elements (Sc and Zr) between the interface and the matrix;
3. Study the effect of Sc and Zr on the precipitation-strengthening of the Al–B₄C composites during heat treatment:
 - Evaluate the influence of Sc and Zr additions on precipitation-strengthening of the matrix at temperatures of 300 to 450 °C for up to 200 h;
 - Examine the morphology, size, volume fraction and distribution of the precipitates and their evolution during the aging process;
 - Apply the shear and Orowan mechanisms to understand the principles of the strengthening;
4. Investigate the long-term thermal stability of mechanical properties of Sc and Zr containing Al–B₄C composites at elevated temperatures:
 - Evaluate the mechanical properties during long-term holding (2000 h), including hardness, yield strength and compressive strength;
 - Investigate the evolution of the microstructure, including the interface, grain structure and precipitates, during the long-term holding (2000 h) process;

5. Investigate the hot rolling process of Sc- and Zr-containing Al-B₄C composites and their precipitation strengthening effect during the post-rolling heat treatment.

CHAPTER 2

LITERATURE REVIEW

Chapter 2

Literature review

It is of great technical and economical interest to improve the efficiency and performance of materials at elevated temperatures. The Al-based metal matrix composites (MMCs) have several remarkable features that make them attractive for the development of high temperature materials. First, the aluminum matrix is naturally oxidation resistant due to a stable protective oxide layer and most ceramic particles in the composites are high-temperature resistant. For weight-sensitive structural applications, the low density of the aluminum matrix and the presence of a certain amount of ceramic particles allow the materials having high specific strength and stiffness. Moreover, aluminum-based MMCs are more economical than existing high temperature aerospace materials (example, Ni- and Ti-based alloys). So far, most efforts have focussed on developing high-strength, thermally-stable Al alloys and can be taken as a favourable groundwork for the development of MMCs. Given the complexity and some unique features of MMCs (for example, ceramic particles and interfacial reaction), the development of a thermally-stable MMC exhibits its own criteria that suitable alloying additions to an Al-based MMC must meet. Therefore,

before discussing the challenges to produce a specific material, a full comprehension of the general requirements for achieving thermally stable MMCs is important.

2.1 General strengthening requirements for thermally stable composites

2.1.1 Strengthening mechanisms in MMCs

The strengthening of materials is related to the introduction one or several kinds of obstacles to hinder the mobility of dislocations [30-34]. The stress field due to the interactions between dislocations and solute atoms, as well as physical barriers (such as grain boundaries and second phase precipitates) may play a role in effectively pinning dislocation motion. The strengthening of Al-based MMCs is mainly contributed by two parties: Al matrix and dispersed ceramic reinforcements. This section will focus on the strengthening mechanisms related to the reinforcement, and the strengthening mechanisms of matrix alloys will be discussed in detail in the following section.

When compared with the corresponding unreinforced materials [1, 35-38], it is well known that the introduction of ceramic particulate reinforcements in the metal matrix results in the enhancement of physical and mechanical properties of composites. The influence of reinforcement on the strength may be divided into two categories: direct and indirect strengthening. These ceramic reinforcements usually exhibit higher stiffness, hardness and strength [39, 40]. If the applied load can efficiently transfer from the relatively “soft” matrix alloys across the matrix/reinforcement interface to these higher stiffness reinforcements, an obvious strengthening effect could be observed in the

composites. This strengthening mechanism in particulate reinforced materials is an extension of the classical composite strengthening mechanism used to describe the behavior of continuous fiber reinforced composites [36, 41]. In addition to this direct strengthening, the ceramic reinforcements also exhibit a significantly lower thermal expansion coefficient than the metal matrix materials, which introduces a large amount of dislocations around the ceramic particulates due to the thermal mismatch. These types of thermal-induced dislocations could also be a strengthening source, referred to as “indirect strengthening” of the matrix [42, 43].

2.1.2 General strengthening mechanism of Al matrix

Besides the strengthening effect contributed by the reinforcement, it is well known that the strength of MMCs is primarily derived from the strength of matrix alloys in MMCs with a low volume fraction of ceramic particles (< 25%). With respect to the strengthening matrix, there are four major strengthening mechanisms, *i.e.*, work hardening, solid-solution strengthening, grain boundary strengthening, and precipitation strengthening. For most of these mechanisms, a range of theoretical expressions is available in the literature [31]. In the present study, an extended assessment of each possible strengthening mechanism has been performed as it is very relevant to the high-strength, high-temperature matrix alloys.

2.1.2.1 Work hardening

Plastic deformation produces a great number of dislocations, which by virtue of their interaction, results in a higher state of internal stress [31]. Hence, when a metal is strained beyond the yield point, an increasing stress is required to produce additional plastic

deformation, and the magnitude of the strengthening effect increases with the degree of deformation [31, 32]. However, annealing at high-temperature leads to the relief of the stored energy in the metal and finally reverts to a strain-free condition [31]. Therefore, work hardening is considered to be thermodynamically unstable and not suitable for application in this work.

2.1.2.2 Solid-solution hardening

The introduction of solute atoms into a crystal lattice invariably provides an increase in strength to the material [44]. These foreign atoms occupy the crystal lattice points of the solvent atoms or interstitial positions in the solvent lattice, and form a substitutional or interstitial solid solution, respectively [31]. Hence, an attractive or repulsive strain field is created around the solute atom which acts as an obstacle to pin the motions of dislocations [30, 31]. Although increasing the temperature weakens the solid solution strengthening, these effects persist up to high temperatures and keep constant when the exposure time is prolonged [10]. However, in order to produce considerable solid-solution strength, a large amount of solute atoms is required. The solid-solution hardening effect produced by the minor addition of the alloying elements is thus expected to be very limited.

2.1.2.3 Grain boundary strengthening

In general, the crystals are separated by a thin non-crystalline region consisting of planar defects. An atomic disorder at the boundary causes a discontinuity in the slip planes [45]. Therefore, as the deformation progresses, a dislocation moves in a common slip plane within one grain while trying to pass through the grain boundary and continues moving in a similar slip plane to the adjacent grain. It thus encounters obstacles: (1) the dislocation has

to change its direction of motion since the two grains are of different orientations; and (2) the discontinuity of the slip planes in the two adjacent grains results in the difficulty of consecutive dislocation slipping [46]. Hence dislocations are unable to traverse a grain boundary, and tend to pile up against it to form grain-boundary ledges [31, 47].

For many materials, the grain-size dependence of the flow stress in terms of the Hall-Petch equation can be mathematically described as [31, 47]:

$$\sigma = \sigma_0 + k_{PH} d^{-1/2} \quad (\text{Eq. 2.1})$$

where k_{PH} is a constant representing the relative hardening contribution of the grain boundaries, d is the average grain diameter and σ_0 is the original yield stress.

Recently, aluminum alloys with nanostructured (< 100 nm) and ultrafine grains (in the range of 100 and 500 nm) were developed and yielded high strength at room temperature [48, 49]. However, grain growth occurred at high temperatures and led to the loss of mechanical properties [50, 51]. Therefore, the fine grains were also considered to be thermally unstable at high temperatures.

2.1.2.4 Precipitation strengthening

Another common source of strengthening is the introduction of alloying elements into the material to form fine second-phase precipitates [31]. Generally, the alloying elements introduced exhibit relatively high solid solubility at an elevated temperature, which reduces as the temperature decreases. Therefore, after solution treatment and quenching from a high temperature, a supersaturated solid solution of solute atoms forms and decomposes during the isothermal aging process at a lower temperature and produces fine precipitates. Lattices

of the precipitate are usually atomic matching, or coherent with the lattices of the matrix. The case where second-phase particles completely lose their coherency with the matrix is referred to as dispersion-hardening [31].

In the case where the precipitates are small and/or soft, the dislocations may cut through the precipitate particles. There are six properties of the particles which affect the ease with which they can be sheared, including coherency strains, stacking-fault energy, ordered structure, modulus effect, interfacial energy and morphology, and lattice friction stress [31, 52].

- Coherency strains: In general, the lattice parameters of precipitates are different from those of the matrix materials. Thus the strain field resulting from the mismatch between a precipitate and the matrix becomes a source of strengthening [53]. The increase of strength can be expressed as [52]:

$$\Delta\sigma_{cs} = 1.2V_p^{1/2} \left(\frac{\Gamma^3 G \varepsilon}{b^3 \langle r \rangle^3} \right)^{1/4} \quad (\text{Eq. 2.2})$$

where V_p is the volume fraction of precipitates, $\Gamma = Gb^2 / 2$, in which G is the shear modulus of the matrix alloy, ε is the lattice parameter misfit between the matrix material and the precipitates, b represents the magnitude of Burgers vector of the matrix material, $\langle r \rangle$ is the average size of precipitates.

- Stacking-fault energy: This stacking-fault energy plays an important role in determining the amount of dislocation splitting into partials and, accordingly, influences the motion of dislocations when the glide dislocations enter the precipitate

and a change in dislocation splitting is required [54]. The contribution of this mechanism on the yield strength is expressed as [52, 55]:

$$\Delta\sigma_{se} = \Delta\gamma^{3/2} \left(\frac{3\pi^2 V_p \langle r \rangle}{32\Gamma b^2} \right)^{1/2} \quad (\text{Eq. 2.3})$$

where $\Delta\gamma = |\gamma_p - \gamma_m|$ represents the differentials of stacking-fault energies between the precipitates and the matrix in the form of an absolute value.

- Ordered structure: The energy is required to create an anti-phase boundary (APB) for the particles with an ordered structure when they are cut through [31]. The increment of hardening is given by [52]:

$$\Delta\sigma_{os} = 0.81 \frac{\gamma_{APB}}{2b} \left(\frac{3\pi V_p}{8} \right)^{1/2} \quad (\text{Eq. 2.4})$$

where γ_{APB} is the APB energy of the precipitate phase.

- Modulus effect: The dislocation energy is proportional to the shear modulus and to the surrounding Burgers vector. If the modulus of the particles differs from that of the matrix, the dislocation energy will change as it shears the particles. The degree of variation depends on the modulus and size of the precipitates. The contribution to the strength by this factor is calculated as [52, 56]:

$$\Delta\sigma_{ms} = 0.0055(\Delta G)^{3/2} \left(\frac{V_p}{\Gamma} \right)^{1/2} b \left(\frac{\langle r \rangle}{b} \right)^{-1+3m/2} \quad (\text{Eq. 2.5})$$

where m is a constant related to the type of the dislocations.

- Interfacial energy and morphology: An external energy must be provided to supply the surface energy increase due to the surface raise after the dislocation threads through the particulates [53]. This strengthening effect is calculated by [52]:

$$\Delta\sigma_{cs} = \left(\frac{6\gamma_s^3 b V_p}{\pi l}\right)^{1/2} \langle r \rangle^{-1} \quad (\text{Eq. 2.6})$$

where γ_s is the precipitate-matrix interfacial energy produced by a dislocation cut through a precipitate.

- Lattice friction stress: This stress is the increment in strength related to the Peierls stress, the minimum stress required to move a dislocation one lattice site [57]. The expression is given by [31]:

$$\Delta\sigma_{ps} \approx \frac{5.2V_p^{1/3} \langle r \rangle^{1/2}}{G^{1/2} b^2} (\sigma_p - \sigma_m) \quad (\text{Eq. 2.7})$$

where σ_p and σ_m are related to the strength of the precipitate and the matrix, respectively.

The accumulation of these mechanisms leads to the increase in strength along with the increase of particle size. A point is eventually reached where precipitates become incoherent and impenetrable so that dislocations are no longer able to cut through them.

Instead, dislocations must find ways to move around the precipitate by one of many possible mechanisms, such as bowing, climbing and cross-slip [58, 59]. Dislocations leave a dislocation loop around each particle after by-passing them. This process repeats itself as long as a dislocation glides over the slip plane and consequently results in dislocations

piling-up around the particle [31]. A back stress exerted by these loops on the dislocation sources must be overcome to trigger the additional slip, which requires an increase in shear stress and leads to a rapid strain-hardening of the matrix [31-34, 45]. This mechanism was first proposed by Orowan and the corresponding Orowan stress, $\Delta\sigma_{om}$, is given by [33]:

$$\Delta\sigma_{om} = \frac{0.81G_{Al}b \ln(2R/b)}{2\pi L_{p-p} \sqrt{1-\nu}} \quad (\text{Eq. 2.8})$$

where ν is the Poisson's ratio of the matrix [60], $R = \frac{\pi}{4}\langle r \rangle$ is the mean radius of a circular crosssection in a random plane for a spherical precipitate [61], and L_{p-p} is the inter-precipitate spacing [52, 61]

$$L_{p-p} = \sqrt{\frac{2\pi}{3V_p}} \cdot \langle r \rangle - 2R = \left(\sqrt{\frac{2\pi}{3V_p}} - \frac{\pi}{2} \right) \langle r \rangle \quad (\text{Eq. 2.9})$$

It is well known that the coherent precipitate produces an increased strain field in the matrix and a further increase in hardness [31]. These incoherent particles exhibit lower hardness than at the stage where coherent particles were present. Continued aging beyond this stage produces particle growth and a further decrease in hardness. In this manner, the precipitates are expected to exhibit a similar crystal structure to the Al solid solution. The similarity in crystal structure between the precipitated phases and the matrix allows for a coherent interface between the two phases and also promises the maximum strengthening efficacy of the dispersed phase [11].

2.1.3 Precipitate coarsening theory

In general, any first-order phase transformation process results in a two-phase mixture consisting of a dispersive second phase in a matrix. However, since a large surface area is present, the mixture is not initially in thermodynamic equilibrium. The total energy of the two-phase system can be decreased via an increase in the size of the second phase, or a decrease in the total interfacial area. Such a process is referred to as *Ostwald ripening* or *coarsening* [62].

In their classic work on the coarsening of binary alloys, Lifshitz and Slyozov [63] and Wagner [64] assumed a common case of spherical precipitates growth by volume diffusion. The LSW theory predicted a mean precipitate radius coarsening from an initial value \bar{r}_0 , to \bar{r}_t with time t , expressed as [65-67]:

$$\bar{r}_t^n - \bar{r}_0^n = kt \quad (\text{Eq. 2.10})$$

where, k is a coarsening rate constant related to the temperature and the composition of the material [67-69], and n is the inverse time exponent [70]. Usually, \bar{r}_0^n is much smaller than \bar{r}_t^n , and is therefore neglected [71]. Equation 2.10 is simplified as

$$\bar{r}_t^n = kt \quad (\text{Eq. 2.11})$$

A log-log plot of Equation 2.11 yields a slope of $1/n$. This slope is also reported to be an indication of the coarsening behavior of precipitates, often called the time exponent of coarsening. For example, the value of $1/n$ was predicted to be $1/3$ according to the classic LSW theory, which well met the experimental value in the Al-Sc binary alloys [67, 71].

However, lower values of the time exponents of coarsening in Al–Sc–X ternary systems were reported. Their values varied from 0.02 to 0.26 depending on the ternary additions (Zr, Er, Mg, etc.) and on the aging temperatures (300, 350, 400 °C, etc.) [70-72].

2.1.4 Requirement for high temperature MMCs

According to the above discussion, and to develop such precipitation-strengthened, high-temperature Al–B₄C composites the following four criteria are expected for the selection of suitable alloying elements.

- (1) **Ability to form nano-size intermetallic precipitates.** To effectively pinpoint the movement of dislocations, certain volume fractions of nano-size precipitates are required. These must be hard enough to prevent shearing by dislocation. In addition, this type of intermetallic precipitates should also have coherent or semicoherent structures with the matrix. Otherwise, when the precipitates transform to the equilibrium structure, the coherency will be lost and result in the decreasing thermal stability of the mechanical properties.
- (2) **Low diffusivity in aluminum.** For diffusion-controlled coarsening, the lower diffusivity of the element leads to a lower coarsening rate of the precipitates, and thus results in a better softening resistance of the material at high temperature.
- (3) **Limited reactions with B₄C.** For any high temperature MMCs, the reinforcement and its interfaces with Al must be stable above the intended service and heat treatment temperatures. In practice, the introduction of certain alloying elements may cause severe reactions with boron carbide reinforcements, resulting in the degradation of

ceramic particles and the consumption of alloying elements at the interface rather than exhibiting a precipitation strengthening effect on the matrix.

- (4) **Capability of casting through traditional ingot metallurgy.** The aim of this study is to develop a series of Al–B₄C composites using conventional ingot metallurgy routes. These composite materials are therefore expected to be conventionally cast and then processed by secondary fabrication techniques such as extrusion and rolling.

2.2 Thermal stability of matrix alloys

2.2.1 Selection of matrix alloys

Based on previous discussions, transition elements and/or rare earth metals are the most promising candidates because of their low solubility and diffusivity in aluminum. Since the 1990s, a large number of studies have been published regarding alloying elements Fe, Cr, V, Zr, Ce, Hf, Y, etc. [15, 73-76]. With the aid of non-equilibrium fabrication techniques, these low-diffusivity additives can strengthen the alloy matrix by forming a large amount of incoherent intermetallics during solidification [17] or by forming fine and uniformly distributed aluminide intermetallics from high supersaturated solid solutions with proper heat-treatments [15, 16, 75, 77]. However, due to the high fabrication cost, the aluminum alloys containing these elements have not been widely accepted.

It is worth mentioning that solid-state precipitation during aging offers potential to generate a much finer dispersion of the strengthening phases than those formed during solidification, and hence provides a good high strength potential of the material [11].

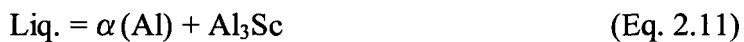
Trialuminide intermetallic compounds of the type Al_3M (where M is an element of transition metals) formed in the solid-state are excellent candidates for use as secondary strengthening phases in the development of high temperature materials [12, 78].

It is desirable that these trialuminide precipitates have the cubic L1_2 structure, which allows a coherent interface between the matrix and the precipitates [11]. In addition, the coherent structure minimizes the surface energy per interface unit and reduces the driving force for precipitate coarsening at high temperature [11].

In 1971, Willey pointed out in his patent that suitable additions of scandium could remarkably improve the mechanical properties of Al alloys [79]. After several years, Russian scientists, Drits [73, 80, 81], Elagin and Zakharov [82-85], started to work on the strengthening effects and the optimization of the Sc content in this system. It was reported that within up to ~0.4 wt.%, each 0.1 wt.% Sc addition produced an average increase in the ultimate strength of 50 MPa [84]. However, the medium diffusivity of scandium relatively lowered the coarsening resistance of the strengthening phase [11]. Based on this fact, ternary or quaternary systems were developed [86-88].

2.2.2 Al–Sc binary alloys

The Al–Sc binary phase diagram is illustrated in the Figure 2.1. There are four intermetallic phases in the diagram: Al_3Sc , Al_2Sc , AlSc , and AlSc_2 . A eutectic reaction occurs at 665°C in the Al-rich region:



in which, the eutectic composition and the solid solubility are approximately 0.46 and 0.38 wt.% Sc, respectively [11, 89, 90].

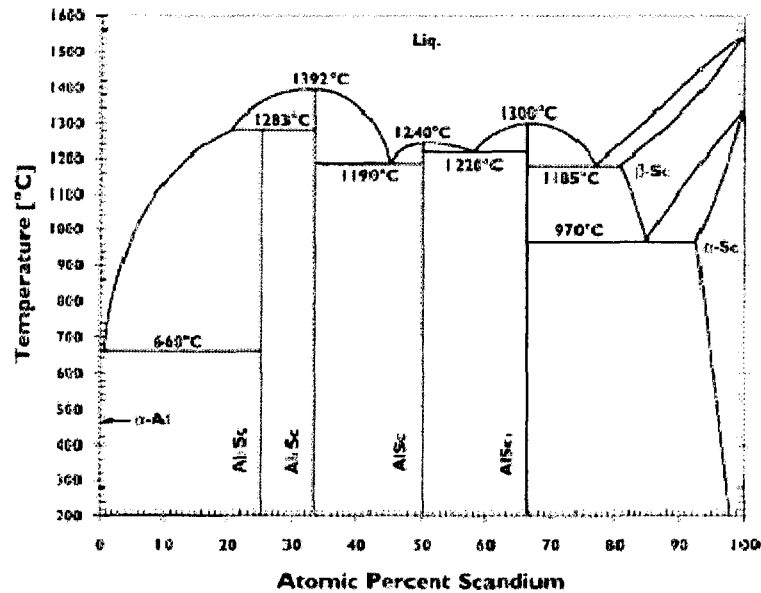


Figure 2.1 Al–Sc binary phase diagram [89]

2.2.2.1 Al₃Sc phase

As the strengthening phase, Al₃Sc is thermodynamically stable, and has a L₂ structure with a lattice parameter $a = 4.103 \text{ \AA}$, and shows an Al misfit of 1.34% at 24°C and 1.05% at 300°C [86, 91]. The orientation relationship between Al₃Sc and the matrix is suggested as being $(110)_{Al_3Sc} \parallel (100)_{matrix}$, $[010]_{Al_3Sc} \parallel [010]_{matrix}$ [92]. There are three possible Al₃Sc formation modes, known as the primary [93], the eutectic [80] and the precipitation [67, 94, 95].

After incubation, the Al_3Sc phase homogeneously nucleates from the supersaturated solid solution at a constant rate [94, 96] with a size range of 4–10 nm [68, 92]. In these studies, most of the precipitates were reported to be spherical. However, their morphology also varied depending on specific conditions. Novotny and Ardell [95] reported that cauliflower-shaped precipitates containing 0.2 wt.% Sc appeared after several hours holding at 350°C and then became spherical after a longer period. The shape of the precipitates containing 0.30 wt.% Sc evolved from spherical to cuboidal as the aging time increased. Marquis and Seidman [68] also observed the cauliflower-shaped and cuboidal precipitates (Al–0.1 wt.% Sc) during 350°C aging, and spherical precipitates (Al–0.3 wt.% Sc) during 300°C aging. Based on high-resolution electron microscope analyses, a type of faceted shape was proposed [68]. In summary, the morphology of Al_3Sc precipitates varies with the change in Sc, the transformation temperature and aging time.

Watanabe *et al.* [67] studied the Ostwald ripening of Al_3Sc precipitates in Al–0.28 wt.% Sc alloy during aging at 400, 425, and 450°C. It was found that the average radius of the precipitates obeys the $t^{1/3}$ time law, as predicted by the LSW theory. The same time dependence of the coarsening behavior has also been reported in several research works [68, 94–96]. Iwamura and Miura [97] investigated the coarsening behavior of Al_3Sc precipitates in Al–0.2 wt.% Sc alloy aged at 400–490°C based on detailed TEM observations. It was shown that the mean radius for coherent/semi-coherent transition of the precipitates was 15–40 nm. The average radius $\langle r \rangle$ of the Al_3Sc precipitates obeyed the r^3 growth law in both the coherent stage ($\langle r \rangle < 15$ nm) and semicoherent stage ($\langle r \rangle > 40$ nm). However,

when the coherent and the semi-coherent precipitates coexisted ($15 < \langle r \rangle < 40$ nm), the coarsening was delayed. Moreover, studies from Novotny *et al.* [95] showed that the size of the precipitates remained in a submicron scale, even for aging times up to 4663 hours.

The mechanical properties of the Al₃Sc phase have not been extensively studied. Drits and Toropova *et al.* examined the microhardness of this phase obtained after 30 s and 60 min aging at 20, 150, 200, 300°C and with a 20 g load. The results are shown in Table 2.1 [92]. According to these results, the Al₃Sc phase can be considered as a high-temperature compound with a hardness loss of less than 50% of its initial value.

Table 2.1 Microhardness of the Al₃Sc phase [92]

Temp. (°C)	20°C		150°C		200°C		300°C	
Time	30 s	60 min	30 s	60 min	30 s	60 min	30 s	60 min
<i>H</i> (MPa)	3990	3500	3310	2370	2690	1830	1980	1040
Softening (%) [*]	12		28		32		47	

*: The softening of the compound was calculated as $(H^{30s} - H^{60\text{ min}}) / H^{30s} \times 100\%$

2.2.2.2 Mechanical properties of Al–Sc binary alloys

Alloying Sc in aluminum results in several attractive mechanical property improvements, such as grain refinement [93], enhanced superplasticity [98, 99], better recrystallization resistance [100], and remarkable precipitation hardening [20, 21, 84, 85, 101-103].

A number of works have been published on the effect of Sc addition on structures and properties of Al alloys. Figure 2.2 illustrates the tendency of hardness as a function of the Sc content in Al. It is obvious that as the Sc content increases from 0.1 to 0.5 wt.%, the

microhardness increases accordingly. This suggests that a higher Sc concentration leads to larger amount of Al_3Sc precipitates generated from the supersaturated solid solution, which can be more effective in hindering a movements of the dislocations so as to significantly increase the strength.

In addition to the Sc content, aging temperatures and holding times can also influence the performance of Al–Sc alloys, as illustrated in Figure 2.3 [78]. After aging at 300°C , the Al–Sc alloys exhibit a maximum strengthening effect. But after prolonging the holding time, overaging represented as a continuous decrease of the strength occurs. A higher aging temperature accelerated the occurrence of peak-aging and reduced the duration of peak-value. In addition, the maximum hardness value of the alloys was less than those obtained at lower temperatures, which is due to the decreased volume fraction of the precipitates [23].

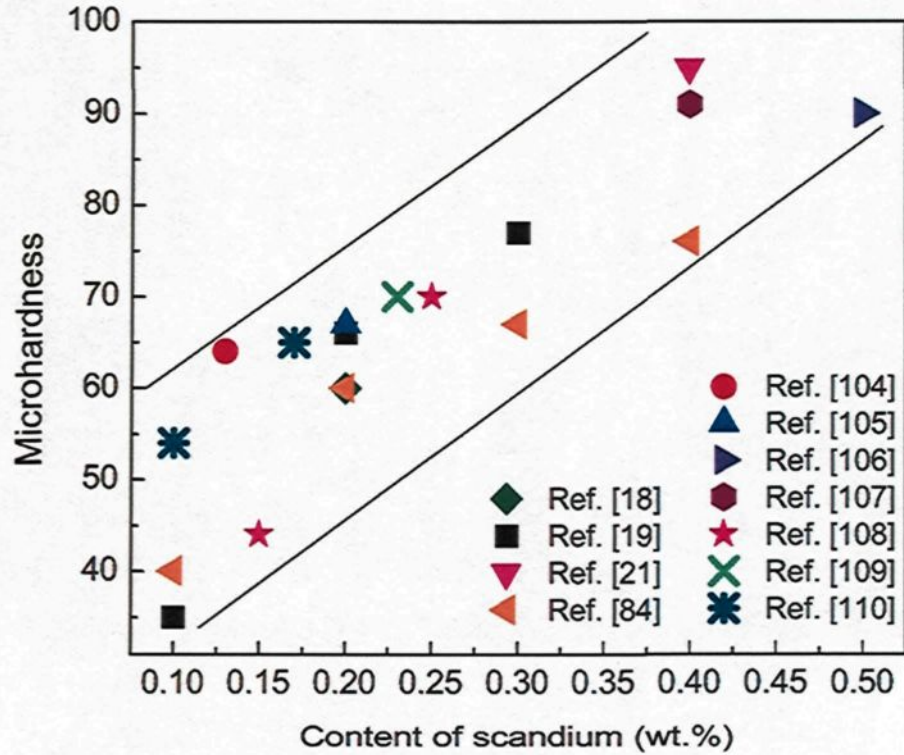


Figure 2.2 Change in microhardness of binary Al-Sc alloys reported in literature with different scandium contents during an isothermal hold at 300 °C [18, 19, 21, 84, 104-110].

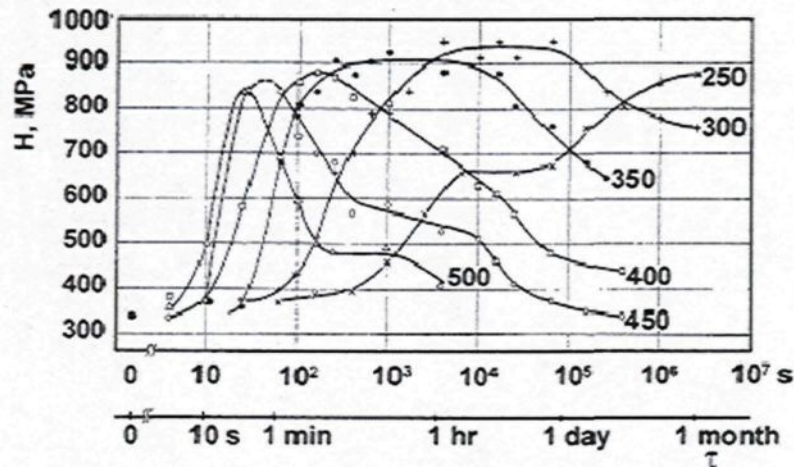


Figure 2.3 Microhardness of a 134 mm diameter Al-0.41wt.% Sc alloy ingot vs. annealing time at various temperatures [78].

2.2.3 Al–Sc–Zr ternary alloys

Although the Al–Sc binary alloys displayed promising properties, especially at elevated temperatures, the utilization of these binary alloys was limited because of (1) the medium diffusivity of scandium in the aluminum and (2) the high cost of scandium [111, 112]. On account of this, ternary alloys have been developed.

Elagin *et al.* first reported that zirconium improved the thermal stability of Al_3Sc precipitates [107]. Thereafter, other researchers confirmed the positive effects of Zr in Al–Sc systems in terms of decreasing the coarsening rate [72, 107], increasing the strength and the recrystallization resistance [23, 113, 114].

2.2.3.1 $\text{Al}_3(\text{Sc}_{1-x}\text{Zr}_x)$ phase

The phase diagram constructed from Al–0.4 wt.% Sc to Al–0.8wt.% Zr is shown in Figure 2.4 [115]. It was found that the Al_3Sc and Al_3Zr phases were in equilibrium with the corresponding Al solid solution. An electron microprobe analysis provided strong evidence that Zr atoms substituted for Sc atoms for the maximum solid-solubility of 13.7–14.2 at.% in the Al_3Sc . In contrast, Sc achieved 3 at.% solid-solubility in the Al_3Zr compound [116, 117]. A further study using atom-probe tomography [118] showed that the maximum Zr concentration within $\text{Al}_3(\text{Sc}_{1-x}\text{Zr}_x)$ precipitates was only 1.5 ± 0.2 at.% after a 576 h soak at 300 °C, which was much lower than the values in previous reports.

Based on the research of Galun *et al.* [116], when $x \leq 0.5$, the trialuminide intermetallics $\text{Al}_3(\text{Sc}_{1-x}\text{Zr}_x)$ exhibited a single L1_2 structure, as shown in Figure 2.5 [11];

whereas, if $x > 0.5$, two $\text{Al}(\text{Sc}_{1-x}\text{Zr}_x)$ phases coexisted: one had a cubic $L1_2$ structure and the other had a tetragonal $D0_{23}$ structure.

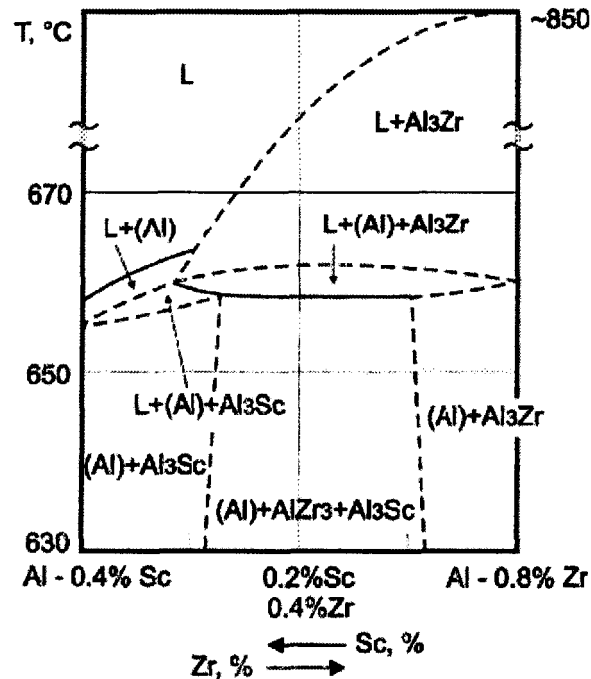


Figure 2.4 Polythermal section of the Al–Sc–Zr phase diagram from Al–0.4 wt.% Sc to Al–0.8 wt.% Zr [115].

These complicated intermetallics show various morphologies according to different alloying compositions and aging conditions. In initial studies, the shape of $\text{Al}_3(\text{Sc}_{1-x}\text{Zr}_x)$ was described to be spherical [113, 116]. Raju *et al.* [119] and Yu *et al.* [120] independently observed cubic morphologies of $\text{Al}_3(\text{Sc}_{1-x}\text{Zr}_x)$ precipitates. By means of high-resolution electron microscopy, Fuller *et al.* proposed a faceted structure whose facets were parallel to the (100) and (110) planes in Al–0.15 wt.% Sc–0.16 wt.% Zr alloy aged at 300 °C [72].

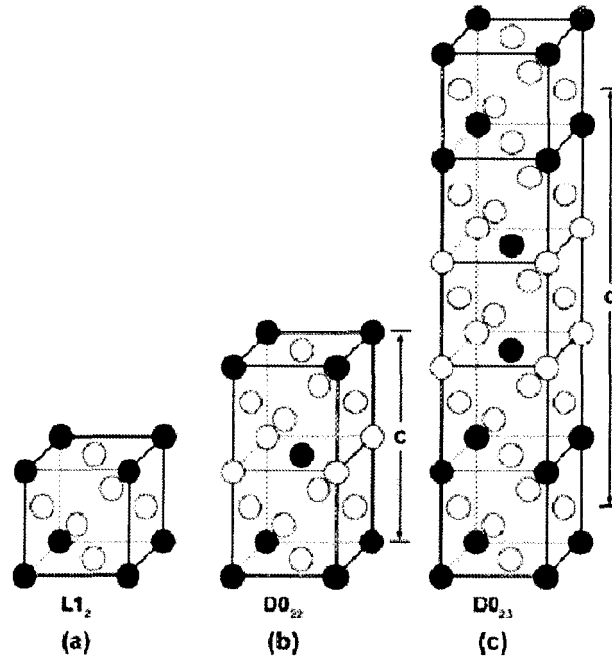


Figure 2.5 The (a) L1₂, (b) D0₂₂, and (c) D0₂₃ structures [11].

Recent studies revealed that Al₃(Sc_{1-x}Zr_x) crystals consisted of a Al₃Sc core surrounded by a Zr-rich shell [118, 121, 122]. The calculated diffusivity of Sc and Zr using Equations 2.12 and 2.13 [123-125] demonstrates that Zr diffuses four orders of magnitude slower than Sc in Al at 300 °C [11, 72]. Thus, the thermal stability of the Al₃(Sc_{1-x}Zr_x) phase is expected to be much higher than that of the Al₃Sc.

$$D_{Sc} = 5.31 \times 10^{-4} \exp(-1.79eV / \kappa T) m^2 s^{-1} \quad (\text{Eq. 2.12})$$

$$D_{Zr} = 728 \times 10^{-4} \exp(-2.51eV / \kappa T) m^2 s^{-1} \quad (\text{Eq. 2.13})$$

2.2.3.2 Mechanical properties of Al–Sc–Zr ternary alloys

During the aging process, Al₃(Sc_{1-x}Zr_x) nanocrystals should be able to uniformly distribute in the matrix and effectively obstruct the dislocation movement. In addition, Zr

substitutions should decrease the lattice parameter of the Al_3Sc precipitates, resulting in the decrease of the lattice parameter misfit [86]. The reduced lattice parameter mismatch was observed to decrease the Ostwald ripening of precipitates rates and benefit the thermal stability of materials [11].

Figure 2.6 shows the influence of Zr on the thermal stability of Al–Sc alloys isothermally aged at a given temperature [84]. In this case, the addition of Zr did not greatly enhance the hardening effect but remarkably improved the stability for up to 10^6 s (about 277 h) holding at 350 °C. However, many works [22, 23, 84, 92, 126] have suggested that the ternary alloys could display higher hardness values than those of the corresponding binary Al–Sc alloys, in addition to the softening resistance improvements shown in Figure 2.7 [111]. The maximum precipitation hardening effect can be achieved during annealing at temperatures ranging from 300 to 350 °C [23]. Toropova [92] reported optimum concentrations of 0.2–0.3 wt.% Sc and 0.15 wt.% Zr for the Al–Sc–Zr system, while Belov [114] suggested that the total concentration of Sc and Zr in commercial Al alloys should not exceed 0.3–0.4 wt% with the ratio $\text{Zr}:\text{Sc} \geq 2$.

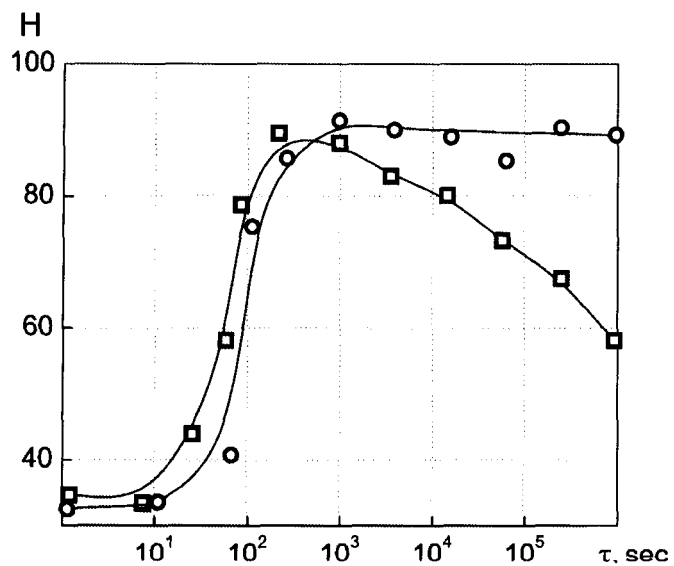


Figure 2.6 Relationship of the microhardness of billets of Al-0.4wt.% Sc (\square) and Al-0.4wt.% Sc-0.15wt.% Zr (o) alloys to annealing time at 350°C (redrawn from Ref [84]).

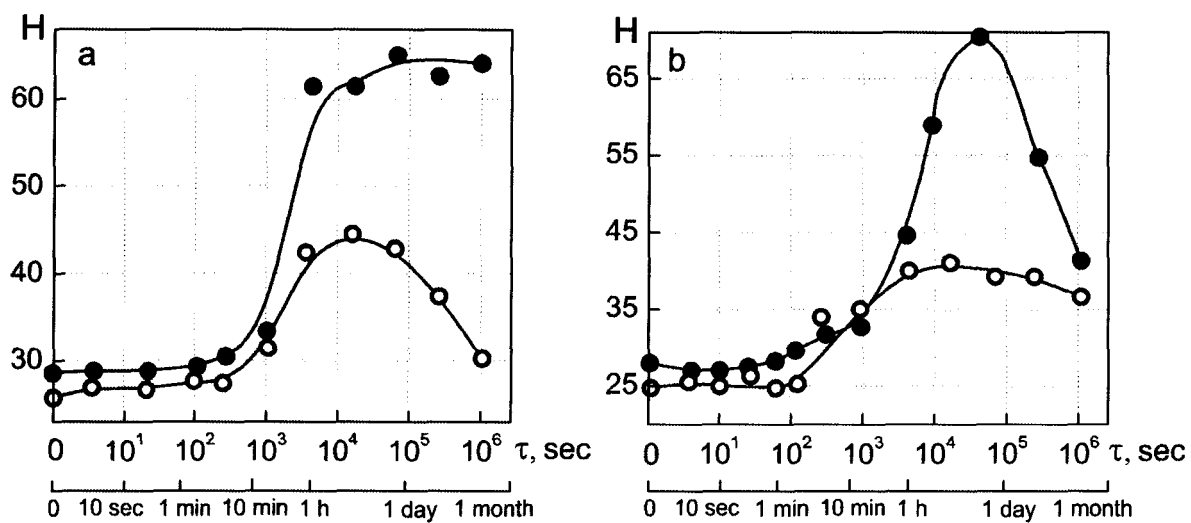


Figure 2.7 Kinetics of the variation of microhardness of Al-0.2wt.% Sc (O) and Al-0.2wt.% Sc-0.15 wt.% Zr (●) alloys in annealing at 400°C a and 450°C b (redrawn from Ref [111]).

2.2.4 The influence of titanium

Due to the limited liquid solubility (0.17 wt.%) and the large solid solubility (1.7 wt.%) of Ti in Al, Al–Ti has a strong tendency to generate primary Al_3Ti during solidification in the conventional ingot metallurgy process, when the concentration of Ti is higher than the maximum liquid solubility [11]. Furthermore, the solid solubility of Ti is still large at a lower aging temperature (for example, $C_{400} = 0.18$ wt.% Ti [11]). Thus, the formation of precipitates is not expected in the subsequent aging process, and the supersaturation is dramatically reduced, leading to the limited chemical driving force for solid-state nucleation as well as the small equilibrium volume fraction of the strengthening phases. This phenomenon has already been reported [127, 128].

Despite the fact that the addition of Ti did not contribute to the increase of strength in Al–Ti binary alloys, van Dalen et al. [129] and Hyde et al. [130] found that Ti indeed exhibited a positive influence to enhance the hardening effect in Al–Sc binary alloys. According to van Dalen et al. [129], after aging at 300 °C for 1534 hours (64 days), Ti substituted for Sc in the Al_3Sc phases and formed the precipitates of $\text{Al}_3(\text{Sc}_{1-x}\text{Ti}_x)$ with a maximum solubility of 0.06 at.%. Even though such a low substitution was reached, there was still an obvious increase of hardness compared to Al–Sc binary alloys. The distribution of Ti in $\text{Al}_3(\text{Sc}_{1-x}\text{Ti}_x)$ precipitates was inhomogeneous and the precipitates consisted of an Al_3Sc core surrounded by a spherical Ti-enriched outer shell, which is similar to the situation in Al–Sc–Zr alloys [122, 131].

2.3 Al–B₄C composites

2.3.1 Al-matrix composites

The concept of a composite material, in general, is to synergize certain properties of its constituents, and to suppress the shortcomings of each of the constituents [40]. This combination can result in a newly synthesized material having unique and useful properties for a spectrum of structural applications [132]. The MMCs have combined metallic properties (ductility and toughness) with ceramic properties (high strength and high modulus), leading to greater strengths in shear and compression and higher service temperature capabilities [1, 133, 134]. Commonly used reinforcement materials include carbides (e.g., SiC, B₄C, TiC), nitrides (e.g., Si₃N₄, AlN), oxides (e.g., Al₂O₃), as well as elemental materials (e.g., C, B, W). The reinforcements may be in the form of continuous fibers, chopped fibers, whiskers, or particulates [134, 135].

Early studies on MMCs addressed the development and behavior of continuous fiber reinforcement with the motivation of dramatically extending the structural efficiency of metallic materials while retaining their advantages, including high chemical inertness, high shear strength, and good property retention at high temperatures [40]. Unfortunately and despite encouraging results, extensive industrial application of these composites has been hindered by high manufacturing costs, namely, high costs of the reinforcement fibers and advanced fabrication methods [40], as well as fabrication problems such as fiber damage, microstructural nonuniformity, fiber to fiber contact, and extensive interracial reactions [1].

In the late 1970s, efforts were renewed on discontinuously reinforced MMCs using whisker reinforcements [40]. Although whisker-reinforced MMCs were shown to have attractive combinations of strength and thermal stability relative to those of particulate reinforced materials, the high cost of the whiskers [1] and the difficulty in avoiding whisker damage during consolidation led to the concept of particulate reinforcements.

2.3.2 B₄C reinforcement

The reinforced B₄C composite has a lower specific gravity of 2.51 g/cm³ [136] (less than that of Al, 2.7 g/cm³), compared to 3.20 g/cm³ for SiC, and 3.96 g/cm³ for Al₂O₃ [2], as well as a high impact and wear resistance [137, 138], a high melting point [139], a good resistance to chemical agents, and a high capacity for neutron absorption [139-141], making itself a promising candidate for the reinforcement in an Al matrix composite [142].

Compared to many works on the Al matrix composite system using reinforcing SiC or Al₂O₃ particles, the studies on the B₄C reinforced composites are relatively limited. This is probably due to the fabrication problems of Al–B₄C composites via commercial casting. Since the initial wetting angle is large, it is difficult to obtain Al–B₄C composites of full density [143]. Moreover, severe interfacial reactions between B₄C particles and liquid Al have led to the increase of reaction products during the casting process and consequently harmed the fluidity of the melt [25]. Thus, several non-equilibrium methods, such as powder metallurgy [136], infiltration [144-147], cryomilling [138, 142, 148], and the shock-compacted method [137] have been utilized.

However, the traditional casting techniques are still attractive in light of their outstanding merits, as for example their low-cost, net-shape fabrication, and flexibility in designing the structure [149]. A liquid-mixing process involving the incorporation of ceramic particulates into a metallic melt by means of mechanical agitation was therefore developed [135, 150], and the schematic of the process is shown in Figure 2.8. This process has the advantages of producing a homogeneous microstructure, increasing the wettability of liquid aluminum on the reinforcement surface [151], and is convenient to operate [1]. Even through this process favors casting soundness, some defaults still exist: extensive interfacial reactions [152], particle agglomeration [5], and poor interfacial bonding strength resulting from poor wettability [153]. As an additive, Ti was reported to enhance the wettability of liquid Al on boron carbide and to restrain the interfacial reactions between the Al melt and B_4C , which was attributed to the formation of an *in-situ* layer of Ti-B compounds [140, 143, 152].

2.3.3 Matrix/reinforcement interface in Al- B_4C composites

The nature of interfaces is critical for optimizing the performance of a composite [154]. A good interfacial bond plays an important role in reducing the external stress transferred from the matrix to the reinforcements [2, 36, 135, 154], and increasing the crack resistance of the composites during deformation [1]. In order to promote interfacial bonding, enhanced wetting and control of interfacial reactions are two key factors which will be reviewed in the following sections.

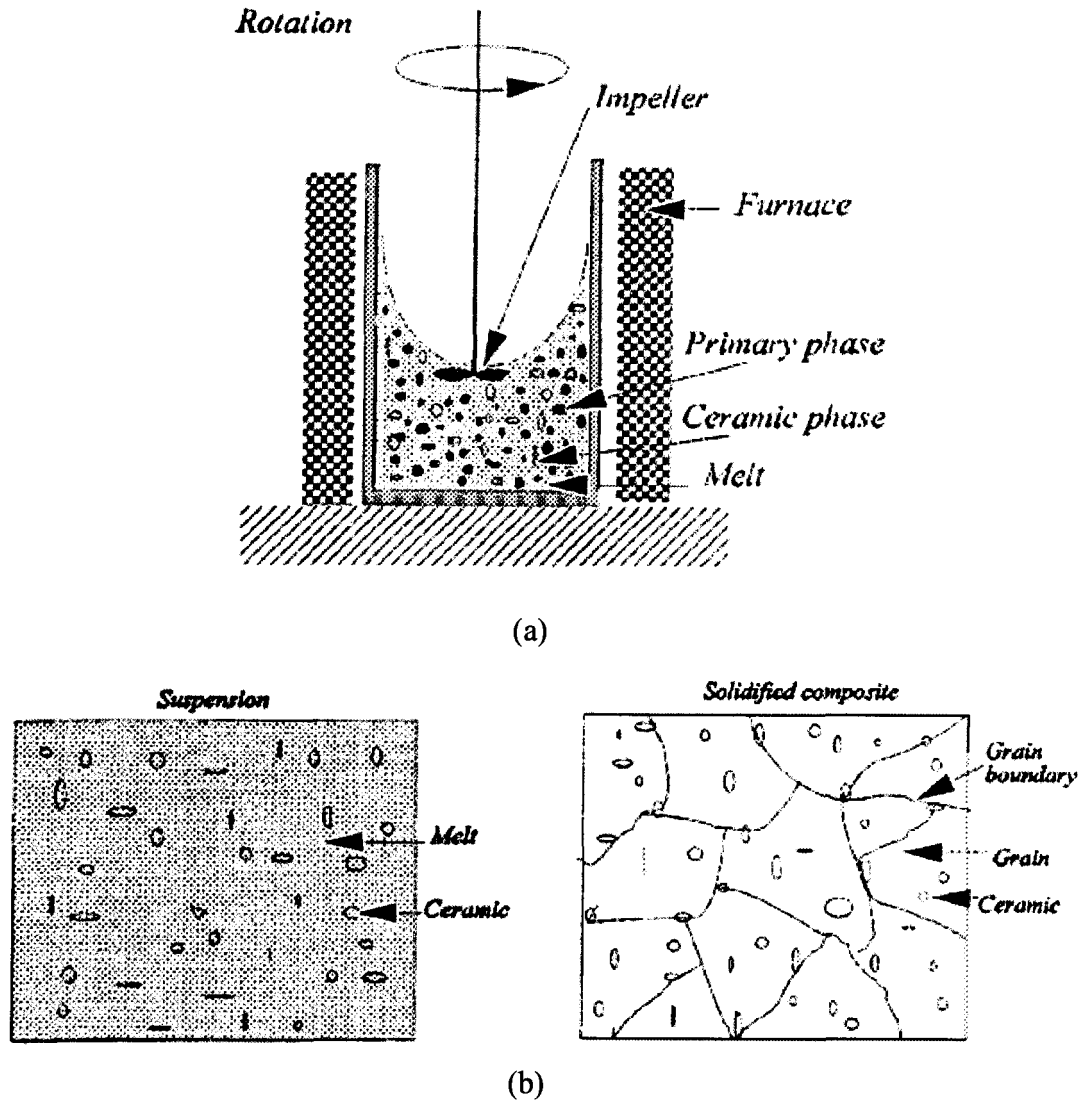


Figure 2.8 Schematics of **a** stirring technique, and **b** solidification process in particulate composites [135].

2.3.3.1 Wetting

Wetting occurs between a metal and a liquid when the strength of the interfacial bond exceeds the surface tension of the liquid [1]. Good wetting often provides a good bonding strength at the matrix/reinforcement interfaces of the final composite [155]. However,

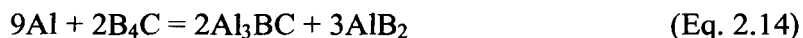
molten metal usually exhibits a high surface tension, resulting in the difficulty of wetting in molten metal-ceramic systems [1]. Halverson *et al.* [156] reported that the pressureless fabrication of Al–B₄C composites below 1000°C was remarkably difficult because the wetting (contact angle $\theta < 90^\circ$) was not obtained during a reasonable time. A similar conclusion was also drawn by Lin *et al.* [157].

Nevertheless, wetting can be favored by introducing strong chemical bonds at the interfaces [155, 158]. With respect to Al–B₄C composites, Ti was found to improve the wetting characteristics between liquid Al and boron carbide particles [5, 27, 159]. Ti was supposed to partially replace the reactions between Al and B₄C and to introduce a new reaction product of TiB₂ enclosing the entire B₄C particles [25, 152, 160]. The Al was able to strongly wet TiB₂ even at temperature below 1000 °C [161, 162]. This process obviously enhanced the wettability of Al on the ceramic reinforcements.

2.3.3.2 Reaction thermodynamics

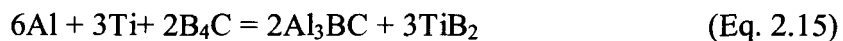
In 1989, Halverson [156] studied the reaction thermodynamics of Al–B₄C in a larger temperature range from 800 to 1400°C. It was confirmed that two major reaction compounds, AlB₂ and an unknown phase x, formed after the reactions occurred below 900°C. According to Sarikaya's work [163], this phase was identified as Al₄BC which tied up most of the free carbon required to form Al₄C₃. Although this ternary phase was adapted during the next several years [164], Viala *et al.* were finally able to verify the formula of this phase as Al₃BC [28, 165]. This trialuminide was a specific feature that differentiated the Al–B₄C couple from other Al-carbide couples, such as Al–TiC [2] and Al–SiC [166,

167], at the interface where Al_4C_3 appeared as a major reaction product. Therefore, the interfacial reaction in the Al– B_4C system in this temperature range should be actually expressed as [25, 28, 168]:



When the temperature was in the range of 900–980°C, Al_3BC was still formed, while a B-rich phase $\text{Al}_3\text{B}_{48}\text{C}_2$ ($\beta\text{-AlB}_{12}$) [28] replaced AlB_2 . A further rise in temperature, beyond 1000°C, would result in the formation of $\text{AlB}_{24}\text{C}_3$ and Al_4C_3 along with the severe depletion of B_4C [164, 169].

Based on the Ti– B_4C phase diagram [170], Ti reacts with B_4C and yields two reactions at temperatures below 920°C, *i.e.*, TiB_2 and TiC . Taking into account that Ti has a much higher affinity with B than Al (Gibbs energies of the formation at 750°C, $\Delta G_{\text{TiB}_2} = -331.0$ kJ/mol, $\Delta G_{\text{AlB}_2} = -108.8$ kJ/mol [26]), and when an additive is introduced into the Al– B_4C system at 730–750°C, Ti will react with Al and B_4C , to form two phases (Al_3BC and TiB_2) in a relatively short time, whereas prolonging the reaction time further will lead to the appearance of AlB_2 [25, 29]. Therefore, by introducing a sufficient amounting Ti addition into the Al– B_4C system, the interfacial reaction would then modified as [26]:



The reactions between the three-component systems of Al–Zr– B_4C and Al–Sc– B_4C have never been reported, although a few works concerning the Zr– B_4C system may be found [171, 172]. Similar to Ti, molten Zr may be expected to react with boron carbide and yield two reaction products ZrB_2 and ZrC [171, 173].

2.3.3.3 Reaction Kinetics

During the liquid-phase processing of MMCs, chemical interactions between the reinforcement and the liquid matrix occur chiefly through the processes of dissolution, precipitation and compound formation [166]. The early stage of chemical interactions of solid ceramics and liquid metals is usually controlled by the process of dissolution of solid phases; however, once a sufficiently thick layer of an interphase is formed at the interface, the reaction kinetics is dominated by solute-diffusion [154].

At the initial stage, the reaction between liquid Al and B_4C is carried out at some location [28], where B_4C is decomposed into B and C atoms to rapidly saturate the molten metal. In this stage, C and B atoms migrate by the liquid-phase dissolution from the surface of B_4C , and thus called “dissolution”. Nucleation and growth of Al_3BC and AlB_2 crystals then occur immediately from the liquid Al, and the mechanism is referred to as “precipitation” [28, 166]. Since nucleation of Al_3BC on the B_4C surface is easier than that of AlB_2 , Al_3BC would grow much faster on the B_4C particles [28]. When the growths of Al_3BC crystals tend to join together and form a dense layer at the B_4C surface, this “dissolution-precipitation” mechanism would no longer be suitable. Further growth of reaction product crystals (Al_3BC and AlB_2) is controlled by the diffusion of B, C, and Al atoms through the growing Al_3BC layer [28]. Thus, it is suggested that the formation of Al_3BC should be reaction-rate controlled, while the formation of AlB_2 should be diffusion controlled [174].

2.3.4 Properties of Al-B₄C composites

In general, particulate-reinforced composites exhibit enhanced stiffness and strength compared to unreinforced matrix materials [1, 2, 37, 40]. However, the improvement in stiffness and strength is generally obtained at the expense of ductility and fracture resistance. Table 2.2 shows the dependence of the composites' mechanical properties in terms of different B₄C concentrations. It is obvious that the strengths of the composites increase with the increase of B₄C concentrations, while the ductility shows a contrary tendency. This relationship is independent of the fabrication process, because more load would be transferred to the reinforcement when the volume fraction is increased, which results in a higher ultimate tensile strength [36].

Table 2.2 Room temperature mechanical properties of Al-B₄C composites

Matrix materials	Fabrication	V_{B_4C} (vol.%)	YS (MPa)	UTS (MPa)	Elongation (%)	Ref.
Al-7Si-0.3Mg (wt.%)	Casting, with K-Al-Ti-F flux adding, as-cast	5	106	165	2.8	[146]
		10	120	188	1.6	
AA6063	Liquid mixing process, extruded	6	241	276	10.1	[175]
		10.5	253	286	4.2	
AA6063	Liquid mixing process, extruded	10.5	265	290	7	[5]
AA6351	Liquid mixing process, extruded	16	325	360	2.5	
AA1100	Liquid mixing process, hot rolling	15	152	165	–	[176]
AA1100	Liquid mixing process, cold rolling	30	199	190	–	[6]

Previous studies have revealed that smaller particles may provide more strengthening effects than the larger particles [40, 168, 177, 178]. For example, Kouzeli *et al.* [168] reported that given a similar B₄C volume fraction of approximately 50%, the Al–B₄C composites with the average particles size of 29 μm yielded a UTS of 219 MPa, that the UTS value was decreased to 161 and 130 MPa, when the particle size was increased to 58 and 82 μm, respectively.

In addition, the strengths of the composites are strongly structure-sensitive with fabrication defects and the matrix structure [135]. Large volume fractions of fine reinforcements can yield dislocation strengthening in a manner similar to precipitation-strengthened materials, whereas the segregation of particles during the solidification process reduces this strengthening advantage. Thermomechanical processes, such as forging, extrusion and rolling, have been applied to decrease these structure defects and improve the composite strength and ductility, by homogenizing the reinforcement distribution, declustering the agglomerates, eliminating the porosity and yielding fine matrix subgrain structures [37, 179-181].

CHAPTER 3

EXPERIMENTAL

Chapter 3

Experimental

3.1 Experimental composite design and sample preparation

There are two parts in the investigation. In part I, the effect of Sc, Zr and Ti on the interfacial reactions between B_4C and liquid aluminum was studied. In this study, a series of Al/ B_4C couples alloyed with varying amount of Sc, Zr and Ti were prepared to examine their interfacial reactions. In Part II, the influence of the additions of Sc and Zr on the microstructure and the mechanical properties of Al-15 vol.% B_4C composites was investigated. In this stage, eight Al-15 vol.% B_4C experimental composites containing different levels of Sc and Zr were designed to understand the evolution of their properties and examine their microstructures in the as-cast and heat-treated conditions. The details of the experimental processes were described in the following.

3.1.1 Al/ B_4C couples

The boron carbide plates used in this study were prepared by hot pressing with 98% of theoretical density, fabricated by Feldco International (Ladera Ranch, CA, USA) under the lot# 255BC. The feedstock powder has an average particle size of 7 μm and a purity of

99.15 wt.% B₄C. The chemical composition of the B₄C powder, provided by the manufacturer, is listed in Table 3.1. The plate was cut into a few of rectangular pieces 30 mm long by 3 mm wide by 3 mm thick. All B₄C pieces were degreased in alcohol and ultrasonically cleaned for 5 minutes.

Table 3.1 The chemical composition of B₄C powder (wt.%)

B ₄ C			B ₂ O ₃	Fe	O	N	Ca	Si
B	C	Total						
80.44	18.71	99.15	0.196	0.202	0.107	0.115	0.084	0.065

Four aluminum alloys with designed compositions (demonstrated in Table 3.2) were made from pure Al (99.99%) and different master alloys, namely Al–2 wt.% Sc, Al–15 wt.% Zr, and Al–10 wt.% Ti. To prepare the experimental alloy bath, approximately 100 g of pure Al was first melted in an alumina crucible. Desired amounts of Sc, Zr and Ti were then added into the liquid Al in the form of master alloys. After the molten alloy stabilized at 730°C, the B₄C piece was carefully immersed in the alloy bath and was suspended by a fixed unit using the experimental set-up shown in Figure 3.1. The molten alloy temperature was maintained at 730°C for each test. The solid-liquid reaction was stopped after a fixed reaction time t ($t = 2$ and 10 h), following the solidification and cooling of the crucible sample in the air.

Table 3.2 Chemical compositions of Al alloys used

No.	Alloying elements (wt.%)			Pure Al
	Sc	Zr	Ti	
1	0.30	/	/	Balance
2	/	0.30	/	
3	/	/	0.30	
4	0.30	0.30	0.30	

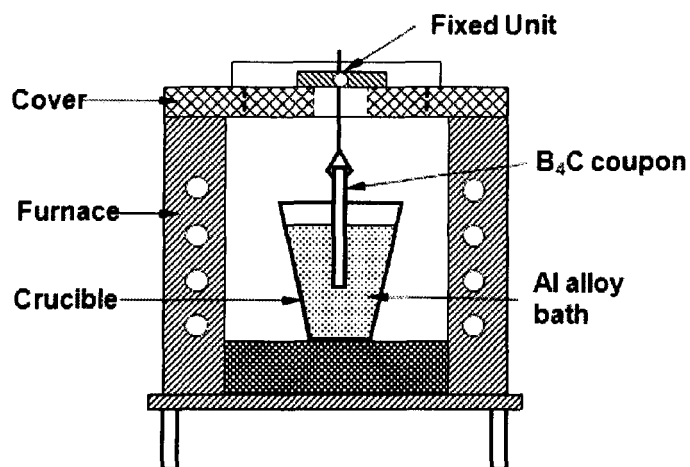


Figure 3.1 Schematic diagram of the experimental set-up.

3.1.2 Al-B₄C composites

Prefabricated AA1100–25 vol. % B₄C with 2.0 to 2.5 wt. % Ti cast billets, supplied by Rio Tinto Alcan, were used to prepare the experimental composites. The average B₄C particle size (F360) was approximately 23 μm . During the batch operation, commercially pure aluminum (99.2%) was first melted in a SiC crucible placed in an electric resistance furnace (Figure 3.2). The master alloys, namely Al–2 wt.% Sc, Al–15 wt.% Zr, and Al–10 wt.% Ti, were then added into the liquid aluminum and held at 800 °C for 40 min to ensure

dissolution of the alloying elements. Afterwards, the prefabricated Al-B₄C billet was added into the liquid metal and the composite melt was held at 730 °C for 30 min. Mechanical stirring was used in order to ensure a uniform distribution of B₄C particles in the liquid. The composite melt was then cast into a rectangular permanent steel mold with internal dimensions of 30 × 40 × 80 mm. The commercially pure aluminum, master alloys and prefabricated Al-B₄C billets were used in such proportions that the final eight composites consisted of 15 vol. % B₄C and 1.5 wt.% Ti, while the Sc and Zr levels varied accordingly. The total amount of liquid composites for each batch was approximately 2.5 kg. The nominal chemical compositions of the Al-B₄C materials are shown in Table 3.3.

Table 3.3 Nominal chemical compositions of eight model composites

Composites code	Element (wt.%)				Al
	Sc	Zr	Ti	B ₄ C (vol.%)	
Base	–	–	1.45	15	
Z24	–	0.24	1.45	15	
S29	0.29	–	1.45	15	
S40	0.40	–	1.45	15	
S58	0.58	–	1.45	15	Balance
SZ29	0.29	0.24	1.45	15	
SZ40	0.40	0.24	1.45	15	
SZ58	0.58	0.24	1.45	15	

Note: Z represents the alloying element Zr
 S series contain Sc only
 SZ series contain both Sc and Zr

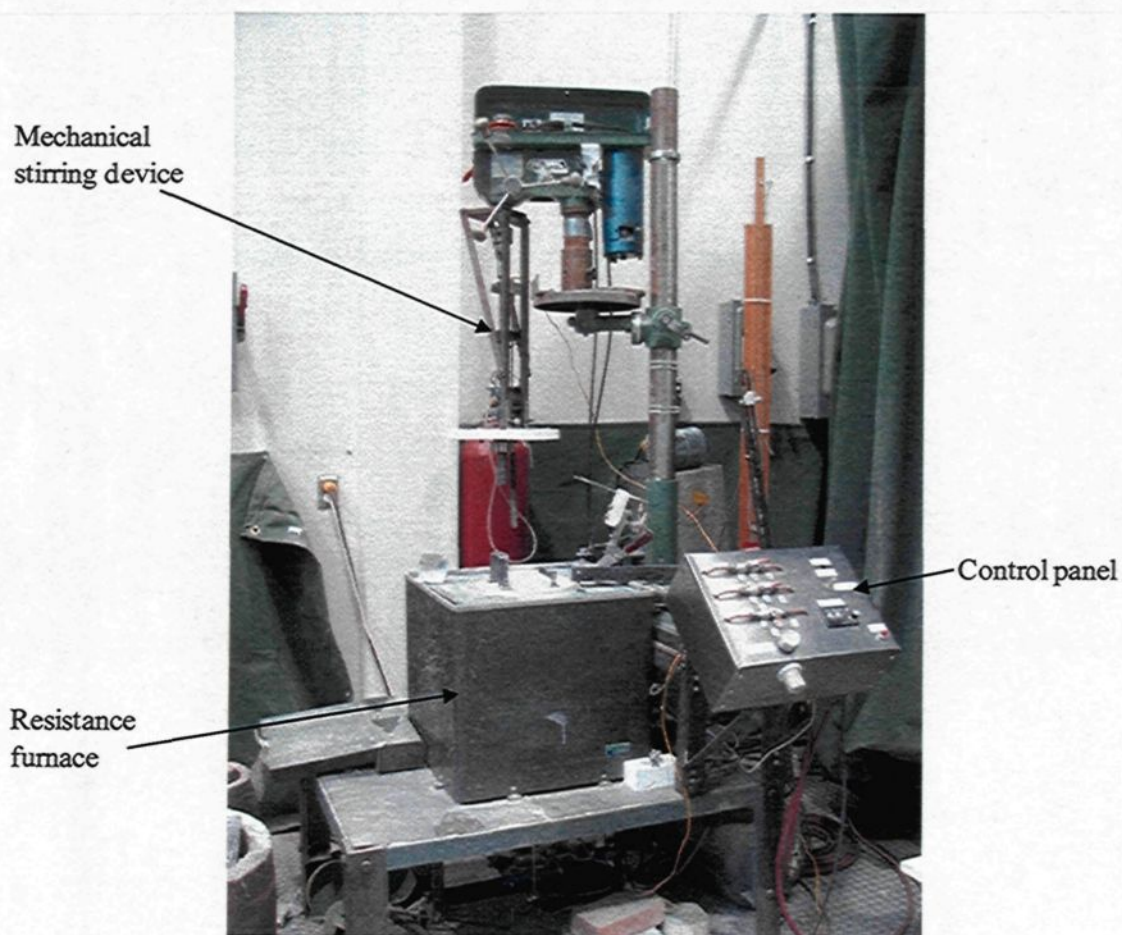


Figure 3.2 The electric resistance furnace used for batching liquid composites.

3.2 Heat treatment

Heat treatments were conducted to yield the precipitation-strengthening for the Al-B₄C composites. The homogenization and precipitation-strengthening aging procedures for the castings were carried out in a BLUE-M ELECTRIC furnace with $\pm 5^\circ\text{C}$ temperature variation. The temperature was recorded by a unit provided by NATIONAL INSTRUMENT NI-SCXI-1303. The long-term annealing procedures were conducted in a

THERMOLYNE electric furnace, with a temperature variation of $\pm 2^\circ\text{C}$, connected with a GRAPHTEC midi LOGGER GL200A system to acquire the temperatures.

3.2.1 Aging for precipitation-strengthening

To evaluate the precipitation hardening responses, the cast samples were homogenized and aged. It is widely accepted that homogenization temperature and time have an influence on the subsequent aging process, which is reported to be in the range of $640\text{--}658^\circ\text{C}$ for the Al-Sc-(Zr) alloys [23, 129]. To better determine the homogenization temperature, the solidus temperatures of two composites with the highest Sc content (S58 and SZ58) were measured using a differential scanning calorimeter (PERKIN ELMER DSC7). Results showed that two materials have similar solidus temperature around 650°C . Hence, the homogenization temperature of Zr-containing materials was fixed at 640°C , while temperature of Zr-free ones was set to 635°C . In addition, considering much lower diffusion rate of Zr in the Al-matrix, the holding time of homogenization of Zr-containing materials was selected as 96 hrs, and that for the Zr-free ones was kept at 24 hrs. After homogenization, samples were immediately quenched into water at room temperature and subsequently aged at temperatures ranging from 300°C to 450°C at intervals of 50°C for up to 200 hrs, as listed in Table 3.4.

Table 3.4 Heat treatment parameters applied in this study

Step	Temperature (°C)	Time (h)	Cooling
Homogenization (Solution treatment)	635	24 h (S series)	Quenched into water at room temperature
	640	96 h (SZ series)	
Aging	300	15 min, 30 min, 1, 4, 10, 24, 50, 100, 150, 200	Cooling in air
	350		
	400	5min, 15 min, 30 min, 1, 4, 10, 24, 50, 100, 150, 200	
	450		

3.2.2 Long time annealing

To assess the long-term thermal stability of experimental composite mechanical properties at elevated temperatures, a long time annealing process up to 2000 hrs was performed. Prior to the annealing, samples were heat-treated in the peak aging condition using homogenization followed by aging. The parameters of the annealing as well as the homogenization and peak aging steps are shown in Table 3.5. It should be mentioned that the peak aging parameters are based on the experimental results of Table 3.4.

Table 3.5 Heat treatment parameters for the long-term annealing

Model composites	Homogenization*		Aging		Annealing	
	T (°C)	Time (h)	T (°C)	Time (h)	T (°C)	Time (h)
S40	640	24	300	10	250	200, 500, 1000, 1500, 2000
					300	
SZ40	640	96	350	10	300	1500, 2000
					350	

*: After homogenization, samples were immediately quenched into water at room temperature

3.2.3 Post-rolling heat treatment

The aging responses of as-rolled composite S58 and SZ58 at 300 °C were investigated. Two rolled experimental composites (S58 and SZ58) were treated at 640 °C for 24 hrs (homogenization) and aged at 300 °C for up to 100 h; the details of these parameters are listed in Table 3.6. Furthermore, the influence of homogenization time on the matrix hardening was also investigated. Details of parameters were listed in Table 3.7.

Table 3.6 Post-rolling heat treatment parameters for aging response investigation

Model composites	Homogenization*		Aging	
	T (°C)	Time (h)	T (°C)	Time (h)
S58	640	24	300	1, 10, 24, 50, 100
SZ58	640	24	300	

*: After homogenization, samples were immediately quenched into water at room temperature

Table 3.7 Applied heat treatment parameters for solution-treatment investigation

Model composites	Homogenization*		Aging	
	T (°C)	Time (h)	T (°C)	Time (h)
S58	640	0.5, 1, 4, 6	300	1, 10

*: After homogenization, samples were immediately quenched into water at room temperature

3.3 Microstructure observation

3.3.1 Optical microscopy

Optical microscopy (Nikon Eclipse ME600) was used to examine the distribution of B₄C particles in the matrix and the evolution of interfacial reactions during heat treatment.

The samples were mounted and metallographically polished down to 1 micron diamond suspension. The detailed preparation procedure used for the samples is listed in Appendix A.

3.3.2 Scanning electron microscopy (SEM)

A scanning electron microscope (SEM, JSM-6480LV) equipped with energy-dispersive X-ray spectroscopic (EDS) facilities was used to examine the material microstructure (B_4C particles and reaction phases) and the distribution of the alloying elements. To reveal a three-dimensional morphology of phase constituents, metallographic samples were deep-etched with 2.5 % HF for 10 minutes. On the other hand, to obtain a combination between high quality pictures and flat surfaces for element analysis (EDS), samples were lightly etched with the same etchant for 10 seconds only.

3.3.3 Electron backscatter diffraction (EBSD)

EBSD was used for revealing the evolution of the grain size during the long-term holding at elevated temperatures. The specimens used for EBSD analysis were directly cut from the aged sample slice by using a diamond saw, with dimensions of 10 mm \times 5 mm \times 1mm. Then, the specimens were mounted on the sample holder and one-step ion-polished on a JEOL SM-09010 Cross Section Polisher operated at 5 kv and 100–110 mA current for 8 h. An HKL Channel 5 EBSD system equipped on the SEM (JSM-6480LV) was employed for this investigation.

3.3.4 Transmission electron microscopy (TEM)

Specimens for TEM observation were prepared in order to investigate the interfacial reaction and the evolution of precipitates after solidification and aging processes as well as evaluate their volume fraction. To prepare the TEM specimens, some foils were directly sliced from the samples investigated. The thickness of each slice was controlled around 500 μm . The disks 3 mm in diameter were then punched from the foils and metallographically polished on both sides to thicknesses of $\sim 100 \mu\text{m}$. Afterward, the disks were mechanically dimpled and their central thicknesses were further decreased to several micro. After final perforation on a Gatan PIPS (Model 691), the disks were immediately stored in a vacuum dessicator.

TEM samples were examined in a JEM-2100 electron microscope, operating at 200 kV and equipped with an EDS system. Dark-field images of the precipitates were formed using the (100) superlattice reflections of precipitates near the [011] direction and were used for calculating the size. Two-beam diffraction conditions were utilized. The thickness of the foil was determined via electron energy loss spectroscopy (EELS). Precipitate dimensions were determined using image-analysis software (Clemex). Moreover, for all morphologies, the diameter of the precipitate was reported by determining the diameter of an area-equivalent circle.

3.4 Evaluation of mechanical properties

3.4.1 Hardness

Two hardness tests, Vickers microhardness and Rockwell macrohardness, were applied to evaluate the properties of the Al-B₄C composites in this research, performed on a QUALI TEST HVS-1000 and a QUALIROCK-RS tester, respectively.

3.4.1.1 Vickers microhardness

Preliminary tests revealed that larger applied loads resulted in a pronounced error in the measurements due to the increased possibility for the indentator to be impressed on/near the ceramic particulate. Therefore, according to the ASTM standard E92-82, the test load was fixed to be 25 g for an indentation time of 15 s, with the diagonal of impression in the range of 25–40 μm . All hardness samples were polished to a surface roughness of around 1 micron. A minimum of 20 measurements were performed on the matrix of each sample. The mean value and standard deviation were calculated and reported.

3.4.1.2 Rockwell hardness

Based upon ASTM E384 standards, Rockwell hardness in F-scale (HRF, 60 kgf force and 1.588-mm steel-ball diameter) was measured for the samples, represented by the average value of 10 independent measurements.

3.4.2 Compression test

Room-temperature compression tests (MTS 810 Material Testing system) were carried out to measure the compressive strengths. Based on the ASTM standard E9-89a,

cylinders with a length/diameter ratio of 1.5 (12 mm length and 8 mm diameter) were prepared. The total deformation was 0.3 and the strain rate was fixed at 10^{-3} s^{-1} . An average value was obtained from four tests in the same condition.

3.5 Hot rolling process

The cast ingots of two composites, S58 and SZ58, with a dimension of $28 \times 40 \times 80$ mm were hot-rolled on a laboratory scale rolling mill (STANAT CX-100), as shown in Figure 3.3. Due to the limited capacity of the small mill, multi-passes (a total of 35) were applied during the hot rolling process. The thickness of the cast ingot was reduced from the initial value of 28 mm to a final thickness of 2 mm, with a total deformation rate of 93%. The rectangular cast ingot and the final rolling sheets are demonstrated in Figure 3.4. Before the rolling, the cast ingots of S58 and SZ58 were homogenized at 635°C for 24 h and 640°C for 96 h, respectively. Prior to the rolling process, the ingots were preheated to 500°C for 30 minutes. After several passes, to avoid the edge cracking, the plates needed to be heated back to 500°C . These heating processes were repeatedly performed in the whole rolling procedure, and the related soaking times varied from 5 to 30 mins, depending on the thicknesses of the intermediate plates. The detailed hot-rolling procedure is listed in Appendix B.



Figure 3.3 STANAT CX-100 laboratory scale rolling mill used for rolling.

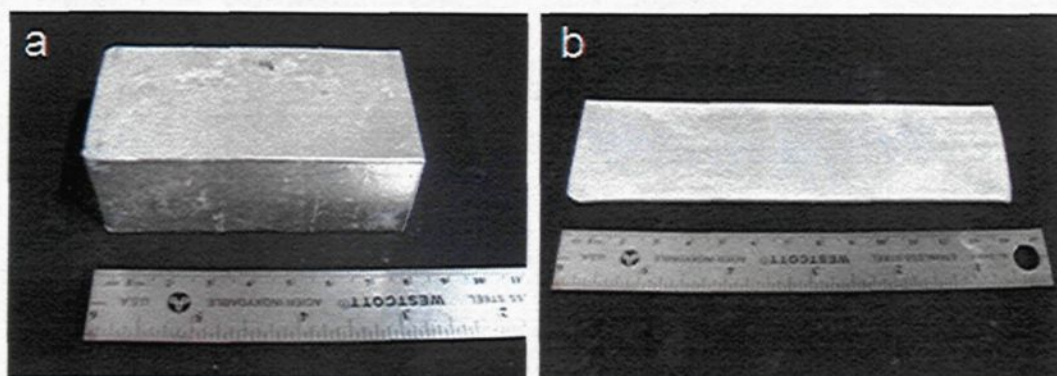


Figure 3.4 The original rectangular cast **a** and the final rolling sheet **b**.

CHAPTER 4

EFFECT OF Sc, Zr AND Ti ON THE INTERFACIAL REACTIONS

Chapter 4

Effect of Sc, Zr and Ti on the interfacial reactions

4.1 Introduction

Scandium, Sc, atomic number 21, is the first element in the Group III transition metals of the Periodic Table. Close to Sc are Ti and Zr, the first and second elements in the Group IV transition metals with atomic numbers 22 and 40, respectively. These three alloying elements exhibit behavior in aluminum alloys. When introducing Sc and Zr into the B_4C/Al system, it is expected that both Sc and Zr will react with B_4C to form reaction products as reported in the Ti case [26, 152] which may have the beneficial effect of preventing the decomposition of B_4C in liquid aluminum. On the other hand, such reactions can consume certain amounts of Sc and Zr that are necessary for precipitation strengthening of the Al-matrix. The ultimate properties of Al- B_4C composites depend on the interfacial bonding and the response of the matrix to precipitation hardening. However, the chemical reactivity of Al-Sc and Al-Sc-Zr alloys with B_4C is almost unknown and public information concerning the interfacial reactions in such multi-component systems is very scarce.

In this chapter, the hot pressed boron carbide plates were used to investigate the effect of Sc, Zr and Ti on the interfacial reactions and resultant microstructures of B₄C/Al couples (see 3.1.1). Four experimental aluminum alloys with different Sc, Zr and Ti contents were prepared (Table 3.2) and the B₄C plates were immersed in the alloy baths to study the solid-liquid reactions (Fig. 3.1). The influence of each alloying element will be identified by its individual addition, while the overall effects of all three elements will be studied by three combined addition to the B₄C/Al–Sc–Zr–Ti system. The interfacial morphology, element distribution, as well as the reaction-induced phases at the interface for each system, have been characterized. This will provide some guidance for the development and manufacture of B₄C particulate reinforced aluminum MMCs.

4.2 Results

4.2.1 Morphology and type of interfacial layers

Figure 4.1 shows the morphology of interfacial layers of B₄C/Al alloys with individual or combined additions of alloying elements after a 10-hour reaction period. In all the experiments, independently of the reaction time, two distinctive layers are observed at the interface of B₄C with molten aluminum. The lamellar layer close to the surface of boron carbide is composed of fine crystals and the serrated layer on the side of the Al-matrix is made up of coarse faceted crystals with growth orientations towards the aluminum matrix.

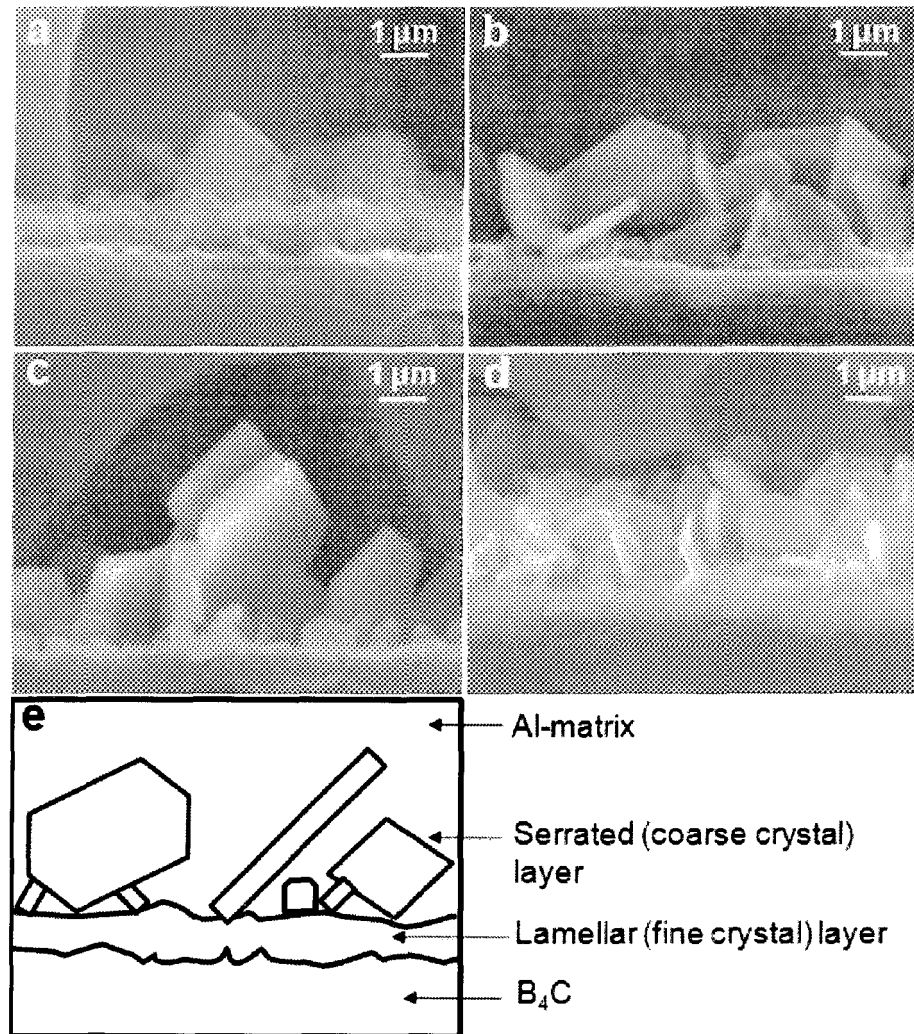


Figure 4.1 SEM micrographs of the deep-etched samples revealing the morphology of the interface after 10 hours reaction time: **a** B₄C/Al-0.3Sc, **b** B₄C/Al-0.3Ti, **c** B₄C/Al-0.3Zr, and **d** B₄C/Al-0.3Sc-0.3Zr-0.3Ti. **e** Schematic diagram illustrating interfacial layers.

It is evident that all four aluminum alloys react with B₄C and form a fine crystal layer followed by a pile of coarse particles (the coarse crystal layer). After a 2-hour reaction period, it was observed that the fine crystal layer already enclosed all of the B₄C plates surfaces and formed a continuous layer in the four alloy systems. Some rough particles

randomly grew from the fine crystal layer towards the Al-matrix and formed a discontinuous layer. With the reaction prolonged to 10 hours, the thickness of the fine crystal layer increased with different rates in each system. Large particles attached to the fine crystal layer continued to grow and coarsen in the direction of the Al-matrix. Figure 4.2 illustrates the growth of the interfacial layers with reaction time in examples of the $B_4C/Al-Ti$ and $B_4C/Al-Zr$ systems.

From the perspective of diffusion, the fine crystal layer can act as a real diffusion barrier in the separation of B_4C from liquid aluminum and, in consequence, the degradation of B_4C may be effectively restrained. Therefore, the average thickness of the fine crystal layer for each B_4C/Al system was measured after reaction periods of 2 and 10 hours. And the thickness of the layer was not uniform on the micro-scale, the average value was taken from the measurements of SEM images over 50 iterations. Results are plotted in Figure 4.3. In the case of adding the alloying element individually, the Al-Sc alloy produced the thickest layer that reached approximately $0.5 \mu m$ after a 2-hour reaction period. The thicknesses of the fine crystal layers were almost equivalent for the Al-Zr and Al-Ti alloys and were about $0.25 \mu m$ after holding in the liquid aluminum for 2 hours. As may be seen, values were only half that observed in the Al-Sc system. It is interesting to notice that the combined introduction of all alloying elements produced a fine crystal layer whose thickness was almost equal to that obtained with the Al-Ti and Al-Zr systems.

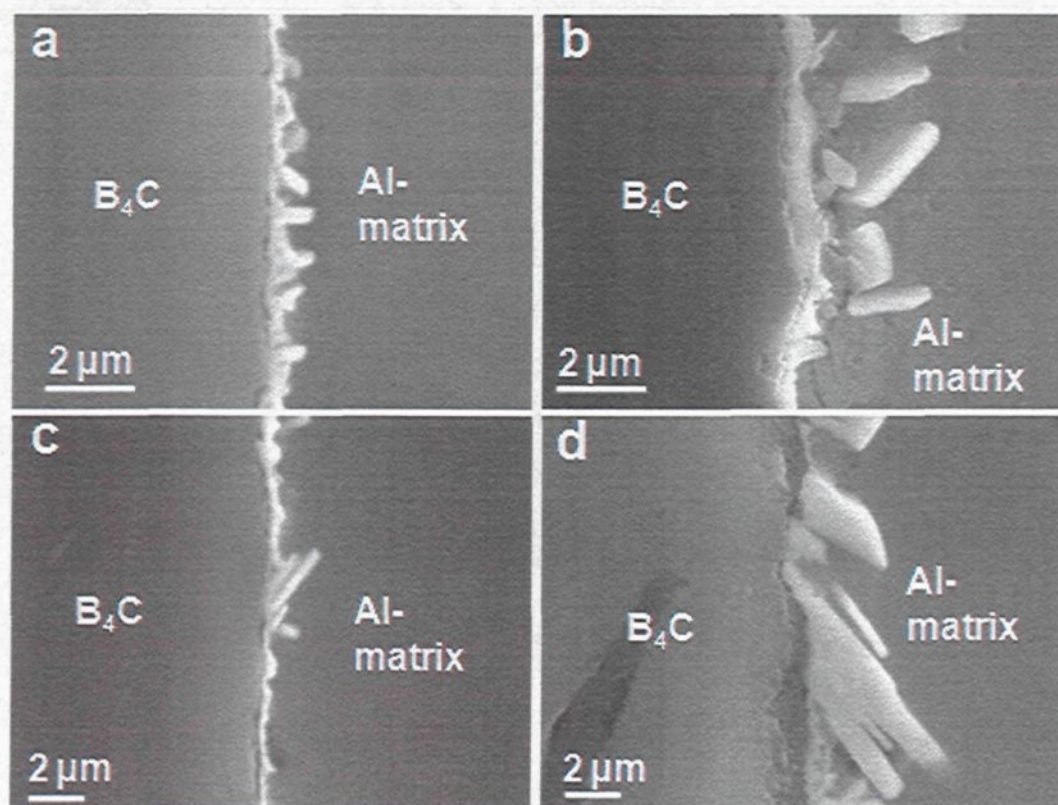


Figure 4.2 SEM images showing the interfacial layers at different reaction times: **a** 2 hours and **b** 10 hours in $B_4C/Al-Ti$ system; **c** 2 hours and **d** 10 hours in $B_4C/Al-Zr$ system.

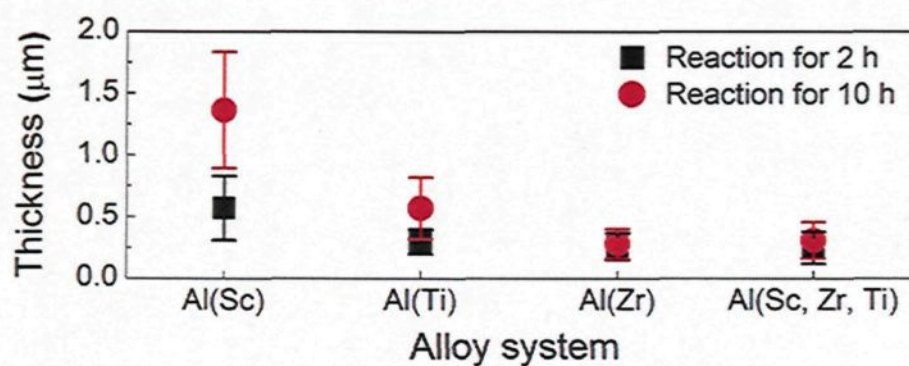


Figure 4.3 The thickness evolution of the fine crystal layer in different alloy systems after 2 and 10 h reaction times.

When the reaction time was prolonged to 10 hours, the thickness value of the fine crystal layer increased by 140%, 90% and 8% for the Al–Sc, Al–Ti and Al–Zr systems, respectively, when compared to the values obtained after the 2-hour reaction period. The fine crystal layer of the Sc-containing system reached approximately 1.4 μm and was nearly 2.4 times thicker than that for the Ti-containing system. The Zr-containing system showed the thinnest fine crystal layer and there was almost no increase in the thickness as the reaction time increased from 2 to 10 hours. Regarding the combined addition of alloying elements, the thickness of the fine crystal layer increased slowly by about 24% with the 2 to 10-hour increase in reaction time, which was less than that observed for the Ti-containing system.

4.2.2 Interfacial microstructure of $\text{B}_4\text{C}/\text{Al-Sc}$ alloy

Transmission electron microscopy (TEM) was used to investigate the detailed microstructure and reaction components of the $\text{B}_4\text{C}/\text{Al-Sc}$ alloy (Figure 4.4). It can be seen from Figure 4.4 a that the B_4C surface was covered with a polycrystalline layer with the crystals exhibiting random orientations, as well as large faceted particles extending from the fine crystal layer. The EDS line scan of Al, B, C and Sc (Figure 4.4b) shows the element distributions across the interface, including the polycrystalline layer and the coarse particle layer. Based on the profiles of the elements, the fine-crystal layer can be divided into two sublayers. The first sublayer, adjacent to the surface of B_4C , was enriched with Al, B and C. The second sublayer, adjacent to the coarse particles, was a Sc-rich lamella

containing Sc, Al, B and C. Moreover, towards the Al-matrix, three elements, i.e. Al, Sc and C, were detected in the coarse particles.

Selected area electron diffraction (SAED) patterns were taken at the different locations for identifying the reaction components and phases. In location I, the component in the first sublayer of the fine crystal layer was indexed to be Al_3BC (Figure 4.4 c). In the second Sc-rich sublayer, the ring patterns from location II were determined to be a mixture of Al_3BC , ScB_2 and Al_3ScC_3 fine crystals (Figure 4.4 d). In the outer coarse particle layer, two phases were identified using the tilt-series technique. In location III, the faceted particles, growing towards the Al-matrix were identified as Al_3ScC_3 (Figure 4.4 e-f). The hexagonal particle in location IV, also adjacent to the Al-matrix, was recognized as ScB_2 (Figure 4.4 g-i). It is clearly apparent that in the $\text{B}_4\text{C}/\text{Al}-\text{Sc}$ system, the fine crystal layer is composed of Al_3BC , ScB_2 and Al_3ScC_3 fine particles, while the coarse layer consists of large Al_3ScC_3 and ScB_2 particles.

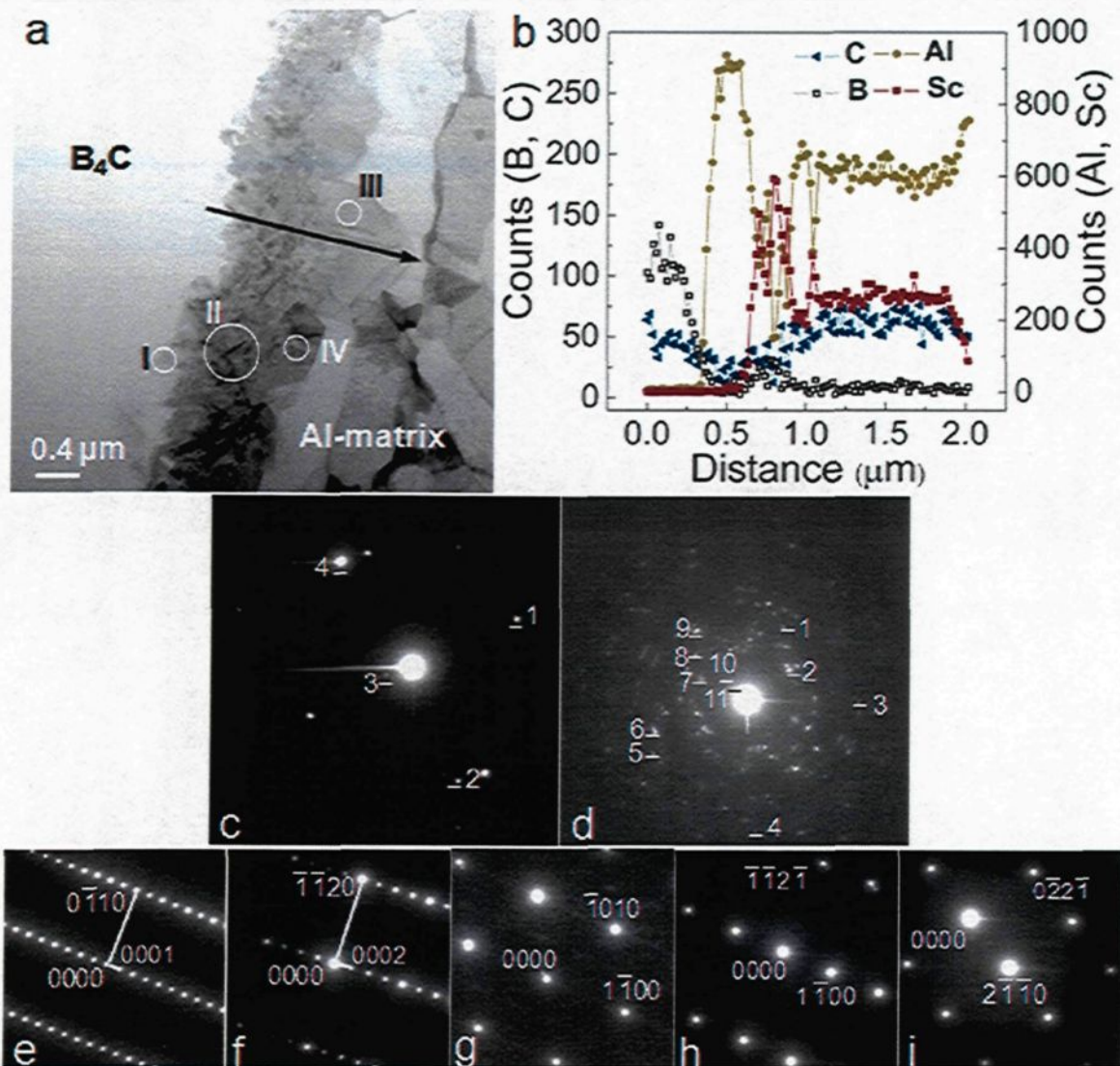


Figure 4.4 **a** Bright-field STEM image of interfacial layers in Sc-containing Al- B_4C system, **b** EDS line scan of Al, Sc, B and C along the arrow in **a**, **c** SAED ring pattern from selected area I: 1, $Al_3BC(101)$; 2, $Al_3BC(102)$; 3, $Al_3BC(001)$; 4, $B_4C(104)$, **d** SAED ring pattern from selected area II: 1, $ScB_2(110)$; 2, $ScB_2(100)$; 3, $ScB_2(201)$; 4, $ScB_2(211)$; 5, $Al_3BC(116)$; 6, $Al_3BC(203)$; 7, $Al_3BC(101)$; 8, $Al_3BC(104)$; 9, $Al_3BC(112)$; 10, $Al_3ScC_3(004)$; 11, $Al_3ScC_3(002)$; **e-f** Al_3ScC_3 phase electron diffraction patterns corresponding to the selected area III at the respective zone axes $[2\bar{1}\bar{1}0]$ and $[1\bar{1}00]$; **g-i** ScB_2 phase electron diffraction patterns from the selected area IV at the respective zone axes $[000\bar{1}]$, $[11\bar{2}\bar{6}]$ and $[01\bar{1}4]$.

4.2.3 Interfacial microstructure of B₄C/Al–Zr alloy

The interface of B₄C/Al–Zr alloy was also studied in detail by TEM, where the B₄C surface was covered with two interfacial layers (Figure 4.5 a). The annular dark-field STEM image illustrates that two sublayers exist in the fine-crystal layer: a dark-gray sublayer close to B₄C made up of lower Z number elements as well as a white sublayer enriched in higher Z number elements. The coarse crystal layer consists of large plate-like particles which extended from the fine crystal layer towards the Al-matrix.

Results of the EDS line scanning indicate that the first sublayer of the fine crystal layer directly attached to B₄C is enriched in Al, B and C, while the sublayer close to the large particles is concentrated in Zr and B, as shown in Figure 4.5 b. The SAED ring pattern in location I indicates that the first sublayer consists of Al₃BC crystals (Figure 4.5 c). The second sublayer in location II is composed of ZrB₂ crystals (Figure 4.5 d). Large plate-like particles extending into the Al matrix (location III) are confirmed to be a ZrB₂ phase by tilt-series technique (Figures 4.5 e–g). In the literature [173], it was reported that Zr reacted with B₄C to form zirconium diboride (ZrB₂) and zirconium carbide (ZrC). However, in this study, no evidence of zirconium carbide formation was found as one of the reaction products in the interfacial region.

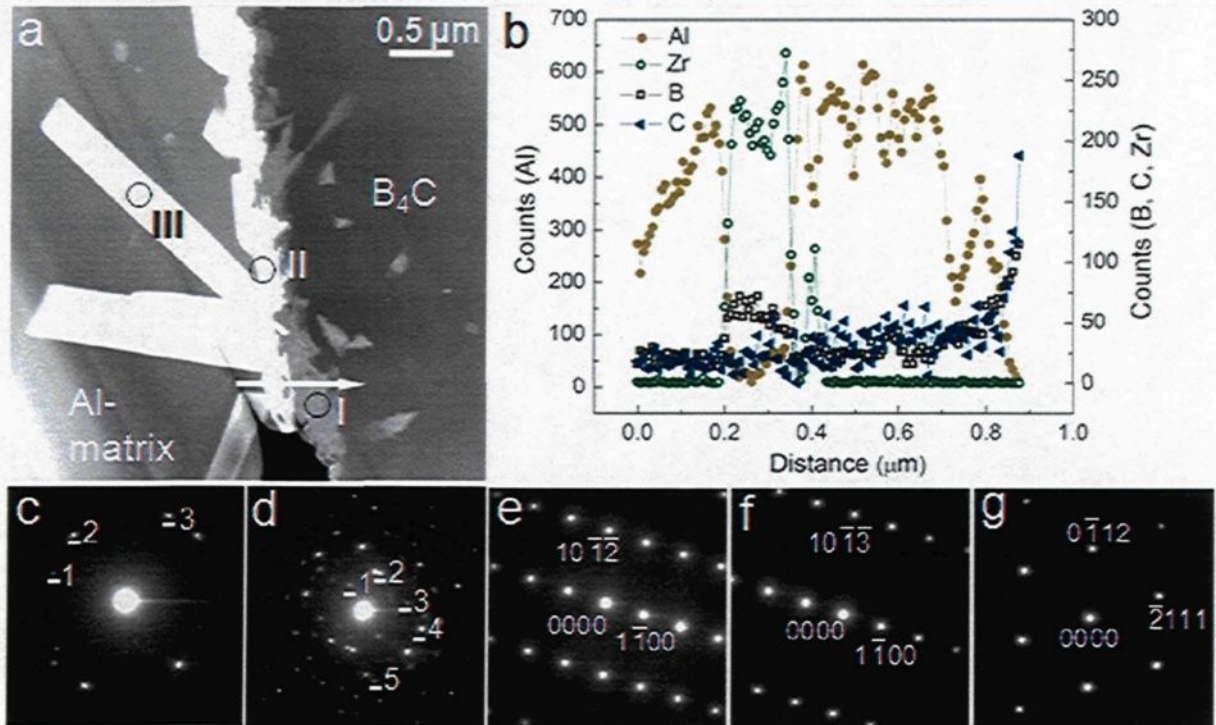


Figure 4.5 **a** Dark-field STEM image of interfacial layers in Zr-containing Al-B₄C couple, **b** EDS line scan of Al, B, C, Zr along the arrow indicated in **a**, **c** SAED ring pattern from region I showing: polycrystalline Al₃BC: 1, (101); 2, (102); 3, (103), **d** SAED ring pattern from region II: 1, Al (200); 2, ZrB₂ (102); 3, ZrB₂ (200); 4, ZrB₂ (211), 5, ZrB₂(104), **e-g** ZrB₂ electron diffraction patterns corresponding to the selected area III at the respective zone axes of [22̄43], [11̄21], and [25̄76].

4.2.4 Interfacial microstructure of B₄C/Al-Ti alloy

For the B₄C/Al-Ti system, it was clearly observed that a fine crystal layer continually covers the surface of B₄C and a number of large particles attach to this layer and grow towards the Al-matrix (Figure 4.6 a). The EDS line scan from the B₄C to the Al-matrix revealed some Al, B, C in the B₄C side of the interface and it changed to mainly Ti and B towards the Al-matrix side (Figure 4.6 b), suggesting the presence of Al₃BC and TiB₂ compounds in the fine crystal layer as well as TiB₂ particles in the coarse crystal layer. The

nature of the interfacial reactions between B_4C and Al-Ti alloys has been established in recent studies [25, 26, 152]. It was identified by TEM that, while the reaction products close to B_4C were Al_3BC crystals and fine crystals of TiB_2 in the nano scale, the coarse particles near the Al-matrix were identified as TiB_2 phase [25, 152].

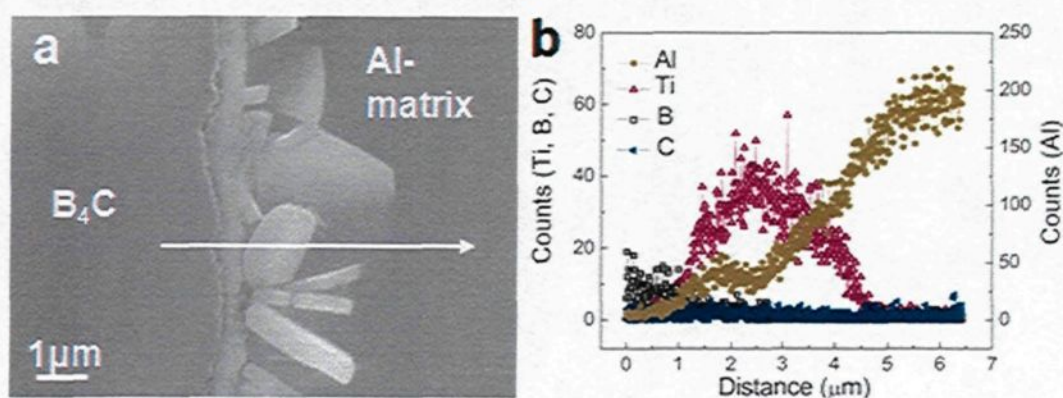


Figure 4.6 **a** SEM image of interfacial layer of B_4C /Al-Ti couple. **b** EDS line profiles showing major element distributions along the white arrow in **a**.

4.2.5 Interfacial microstructure of B_4C /Al-Sc-Zr-Ti alloy

In the case of combined addition of all three alloying elements, the typical microstructure of reaction layers in the interface is shown in Figure 4.7 a. It can be seen that the B_4C surface is covered with a light-grey sublayer which contains Al, B and C (Figure 4.7 b). There is also a dark-gray sublayer which measures approximately $0.1 \mu m$ in thickness and is composed of many tiny nano-size crystals. Results of the EDS line scan indicate that this sublayer is enriched in Ti, Sc, and B with a small amount of Zr (Figure 4.7 b). Several coarse particles, ranging from 0.2 to $2 \mu m$, make up the discontinuous coarse layer towards the Al-matrix side. This coarse layer is concentrated with Ti and B and

contains traces of Sc and Zr. It is interesting to note that a large amount of Ti is concentrated in the interfacial layers, while small amounts of Sc and Zr are detectable at the interface.

The SAED ring pattern in area I confirms that the first sublayer close to the B_4C plate consists of polycrystalline Al_3BC (Figure 4.7 c). The second sublayer, adjacent to the coarse particles in area II, is composed mainly of TiB_2 type nano-crystals (Figure 4.7 d), in which Sc and Zr atoms may replace some Ti atoms in the TiB_2 phase. The outside coarse layer near the Al-matrix (area III) consists of large single-crystal TiB_2 type particles (Figure 4.7 e–g) which contain a trace amount of Sc and Zr.

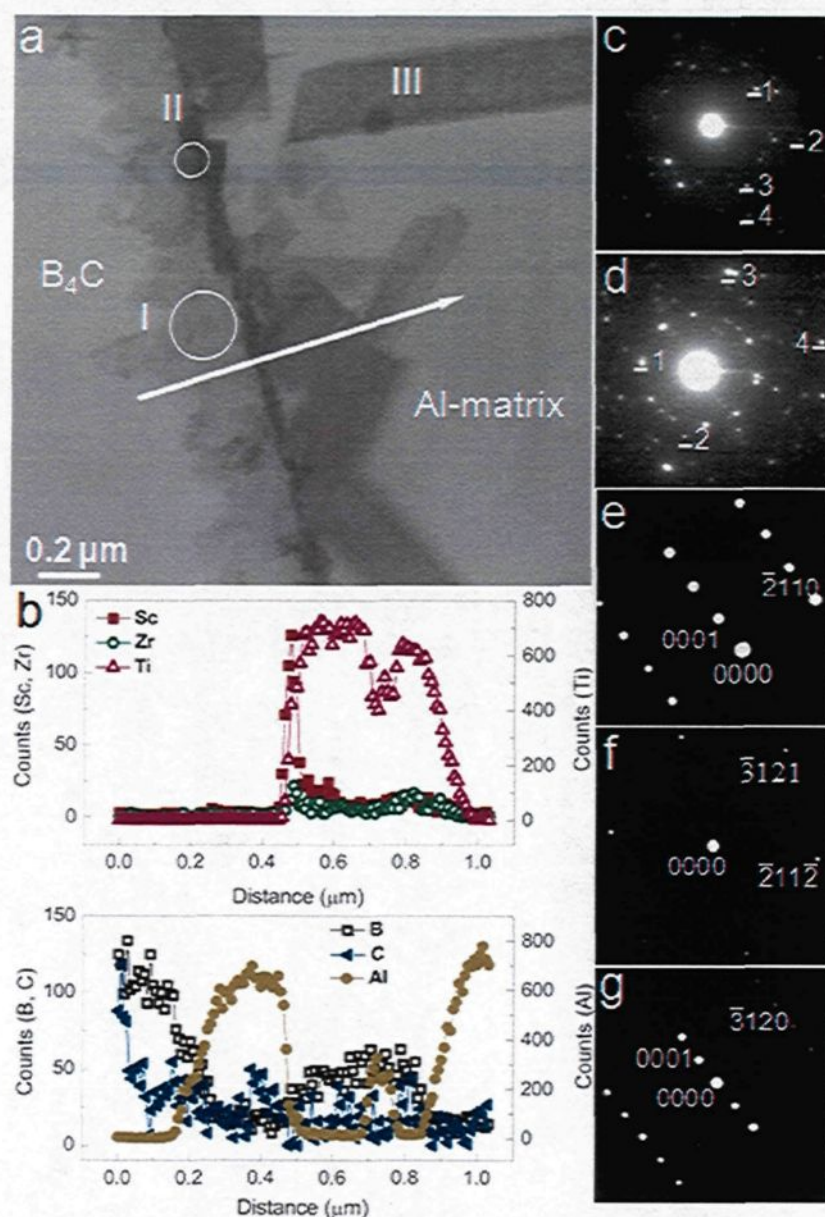


Figure 4.7 **a** Bright-field STEM image of interfacial layers in Sc, Zr, and Ti containing Al-B₄C couple, **b** EDS line scan of Al, B, C, Sc, Zr, and Ti along the arrow indicated in **a**, **c** SAED ring pattern from region I showing polycrystalline Al₃BC: 1, (101); 2, (105); 3, (103); 4, (110), **d** SAED ring pattern from region II showing polycrystalline Al₃BC and TiB₂: 1, TiB₂(101); 2, Al₃BC(110); 3, TiB₂(201); 4, Al₃BC(201), **e-g** TiB₂ electron diffraction patterns corresponding to the selected area III at the respective zone axes of [01 $\bar{1}$ 0], [$\bar{2}13\bar{1}$], and [$\bar{1}5\bar{4}0$].

4.3 Discussion

The microstructural observation reveals that all B₄C/Al systems studied in this work show some common features at the interface. The instability of boron carbide in liquid aluminum triggers the interaction between B₄C and the melt. All three alloying elements react with B₄C and form reaction products and layers covering the B₄C surface. The interfacial region consists of two distinctive layers: a fine crystal layer close to the B₄C surface and a coarse crystal layer near the Al-matrix. During immersion testing, the B₄C plate contacts with the liquid aluminum and alloying elements which react with the B₄C. This leads to the dissolving and release of B and C atoms into the molten aluminum. Since the solubility of boron and carbon in aluminum is low (~ 1000 ppm for boron at 1000 K [28] and 6 ppm for carbon even at 1223 K [182]), carbides and borides precipitate from the saturated liquid as reaction products. The fine reaction crystals form at the surface of the B₄C. As the number of fine crystals continues to increase with increased reaction time, they build up the first interfacial layer that progressively encloses all the B₄C surfaces. When the reaction time is prolonged, the reaction particles begin to grow and coarsen towards the liquid aluminum.

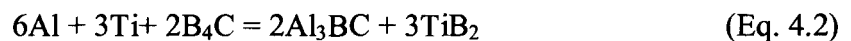
In the binary B₄C/Al system, reaction between B₄C and liquid aluminum takes place according to the following interfacial reaction [25, 28]:



Two reaction products, Al₃BC and AlB₂, form at the interface. In our preliminary tests, the interfacial reaction between pure liquid aluminum and the B₄C plate was also

studied in the immersion testing. Results showed that the formation of Al_3BC and AlB_2 at the interface led to a quick decomposition of B_4C , which confirmed the fact that these two compounds are unable to prevent the attack of liquid aluminum on B_4C [25, 26, 28, 152]. With the addition of alloying elements, the interfacial layers formed at the B_4C surface can act as a diffusion barrier to limit the decomposition of B_4C . From the diffusion perspective, the fine crystal layer is dense and continuous, and therefore it becomes a real barrier in avoiding the direct contact of B_4C with the liquid aluminum, and results in transforming a fast liquid diffusion-controlled process into a slow solid diffusion-controlled process. On the other hand, the coarse crystal layer is less dense and of a discontinuous nature and in consequence, it is less effective in separating B_4C from liquid aluminum. Due to a high affinity with boron and carbon, all three alloying elements exhibit somewhat similar behavior in the $\text{B}_4\text{C}/\text{Al}$ system, showing that they are concentrated and consumed at the $\text{B}_4\text{C}/\text{Al}$ interface to form reaction products and layers.

Recent research in the $\text{Al}-\text{B}_4\text{C}$ composites revealed that, with the Ti addition in the $\text{B}_4\text{C}/\text{Al}$ alloy, the following interfacial reaction replaces the reaction (4.1) [26]:



The reaction products Al_3BC and TiB_2 built a protective layer surrounding the B_4C surface. In the $\text{B}_4\text{C}/\text{Al}-\text{Zr}$ alloy, it is found that the fine crystal layer consists of Al_3BC and ZrB_2 , while the coarse layer is mainly made of ZrB_2 particles. Similar to the $\text{B}_4\text{C}/\text{Al}-\text{Ti}$ system, the interfacial reaction in the $\text{B}_4\text{C}/\text{Al}-\text{Zr}$ alloy can be formulated as follows:



In the $B_4C/Al-Sc$ system, it is identified for the first time that three reaction products exist in the interfacial microstructure, namely Al_3BC , ScB_2 and Al_3ScC_3 . The equation for the interfacial reaction of this system can be expressed as:



Taking into account the combined addition of all three alloying elements, mainly two reaction products (Al_3BC and TiB_2 type crystals) in the $B_4C/Al-Sc-Zr-Ti$ system are identified in the fine crystal layer, although some Sc and Zr are also detected in this layer. The outside coarse crystal layer is confirmed to be in the majority of TiB_2 type crystals that also contain traces of Sc and Zr. Due to the fact that most of the Ti but only a small amount of the Sc and Zr concentrate at the interfacial reaction layers, it is reasonable to believe that the interfacial reaction in the $B_4C/Al-Sc-Zr-Ti$ alloy is dominated by reaction (4.2).

It is worth pointing out that all above mentioned interfacial reactions and their reaction phases took place in the liquid stage. During the immersion tests, after the B_4C plate contacted with liquid aluminum for several hours (2 to 10 hrs) at $730^\circ C$, the crucible sample was cooled and solidified in the air. The freeze time of the sample was a few minutes, which was too short to form the reaction products during solidification. It is reasonable to believe that all reaction phases that were identified by SEM/TEM were formed during liquid holding.

It is observed that the thickness of the fine crystal layer varies with different alloying elements. The $B_4C/Al-Sc$ alloy yields the thickest layer after 2 and 10 hours reaction periods. According to the TEM result (Figure 4.4), the ring patterns of the fine crystal layer

are made up of discrete spots suggesting relatively large-size crystals of reaction products collected at the interface. Large grains pile up at the interface as a barrier layer, making it less effective to restrain the diffusion of boron and carbide out of the B_4C . As a result, and although a large amount of Sc is consumed at the interface, it is still inefficient to prevent B_4C decomposition. The $B_4C/Al-Ti$ alloy shows a medium thickness of the fine crystal layer after 10 hours of holding. It has been demonstrated that a Ti-rich layer forms at the B_4C interface and its reaction product TiB_2 is an efficient barrier to limit B_4C decomposition [5, 25, 26, 140, 152]. The ring patterns of the TiB_2 layer obtained in the $B_4C/Al-Ti$ system show many continuous rings, which is recognized as the finest TiB_2 crystals on the nanometer scale [152]. On the other hand, the $B_4C/Al-Zr$ alloy possesses the thinnest layer among the three individual alloying additions, which may suggest that Zr is a potential candidate for stabilizing B_4C during the manufacturing process of $Al-B_4C$ composites.

When introducing all three additives into the B_4C/Al system, the thickness of the fine crystal layer after 10 hours of holding is very moderate and lies between the $B_4C/Al-Ti$ and $B_4C/Al-Zr$ alloys. TEM results show that most of the Ti is concentrated at the interface and the layer is composed mainly of a number of TiB_2 type nano-crystals. It is evident that, when co-existing with Sc and Zr, Ti not only offers appropriate protection of the B_4C but also greatly reduces the consumption of Sc and Zr at the interface.

The $Al-Sc$ alloy exhibits particular promise for developing a thermally stable matrix due to the forming of fine and coherent Al_3Sc precipitates upon aging. The addition of the

slow diffusing element Zr, which is soluble in Al_3Sc , has the potential to increase the coarsening resistance of Al_3Sc precipitates and thus improve the thermal stability of the matrix during prolonged exposure at elevated temperatures [118, 183]. Moreover, it is reported that Ti is also a candidate as a ternary alloying element to the Al–Sc alloy for stabilizing the precipitate structure and improving the coarsening resistance [183]. Considering the commercial benefits, Sc and Zr, in the form of aluminum master alloys, are more expensive than Ti. Therefore, it is desirable for the thermally stable Al– B_4C composites that Ti be primarily used at the interface to prevent B_4C degradation while most of the Sc and Zr remain in the Al-matrix for precipitation strengthening.

By individual addition of three alloying elements in the $\text{B}_4\text{C}/\text{Al}$ system, the alloying element is enriched at the $\text{B}_4\text{C}/\text{Al}$ interface and bonded in the reaction products, which leaves too little to contribute to the precipitation strengthening. In the case of the combined addition of Sc, Zr and Ti, most of the Ti is enriched at the interface to build up protective layers around the B_4C and the concentration of Sc and Zr at the interface decreases greatly. Results obtained in this study give an interesting promise that satisfies two important aspects of producing thermally stable Al– B_4C composites, namely the protection of the B_4C and the response of the matrix to precipitation strengthening.

4.4 Summary

The influences of alloying elements Sc, Zr, and Ti on the interfacial reactions of the $\text{B}_4\text{C}/\text{Al}$ system have been studied in terms of individual and combined additions using immersion tests. All three alloying elements react with B_4C in liquid Al and form

interfacial layers covering the B_4C surface. The interfacial region constitutes two distinctive layers: a fine crystal layer close to the B_4C and a coarse crystal layer near the Al-matrix side. From the diffusion perspective, the fine crystal layer is a real barrier in avoiding the direct contact of B_4C with liquid aluminum. The thickness of the fine crystal layer varies with different alloying elements and reaction times.

Three phases of Al_3BC , Al_3ScC_3 and ScB_2 are identified as reaction products in the $B_4C/Al-Sc$ system. Al_3BC and ZrB_2 in the $B_4C/Al-Zr$ system, as well as Al_3BC and TiB_2 in the $B_4C/Al-Ti$ and $B_4C/Al-Sc-Zr-Ti$ systems are respectively confirmed. The interfacial reactions and the reaction products in each system are outlined.

With individual addition of the three alloying elements in the B_4C/Al system, the alloying element is mainly enriched at the B_4C/Al interface and bonded in the reaction products. In the case of a combined addition of Sc, Zr and Ti, most of the Ti is enriched at the interface, which not only offers appropriate protection to the B_4C but also reduces the consumption of Sc and Zr at the interface.

CHAPTER 5

AS-CAST MICROSTRUCTURE AND PRECIPITATION EVOLUTION

Chapter 5

As-cast microstructure and precipitation evolution

5.1 Introduction

In Chapter 4, the effects of Sc, Zr and Ti on the interfacial reactions between B_4C and melt aluminum were discussed. It was found that, when introducing individual additions of Sc, Zr or Ti to the Al- B_4C system, each element reacted with B_4C and was mainly tied up in the interfacial reaction products. However, in the case of a combined addition of all three elements, most of the Ti but very little of the Sc and Zr enriched the B_4C/Al interface to prevent B_4C decomposition. It is important to note that Ti reduces significantly the consumption of Sc and Zr in the reaction products and consequently increases the amount of Sc and Zr retained in the Al matrix, which provides the precipitation strengthening of the matrix alloy.

In this chapter, Sc or a combination of Sc and Zr are introduced in an Al-15 vol.% B_4C composite presaturated with Ti. Eight experimental composites with different Sc and Zr levels (Table 3.3) are prepared via conventional casting technique while keeping the B_4C

and Ti contents constant (the detailed compositions of samples are listed in Table 3.3). The research focuses on the microstructure and precipitation evolution in the as-cast condition. Attention is paid to the interfacial reaction and its reaction phases, the nature of the precipitates and their distribution, as well as the precipitation strengthening effect on the as-cast composite materials.

5.2 Results

5.2.1 Microstructure of prefabricated material

Figure 5.1 shows optical micrographs of the prefabricated AA1100–25 vol.% B₄C with 2.0 wt.% Ti cast billets, produced by a liquid mixing process [6]. The B₄C particles are uniformly distributed in the Al matrix (Figure 5.1 a). All of the B₄C particles have a straight interface with the Al matrix, and a few reaction products are observed attached to or close to the B₄C particles; three were identified as TiB₂ and Al₃BC [25, 29, 152]. This indicates that the B₄C particles are well protected from the attack of aluminum and no serious B₄C degradation occurs during the billet manufacture.

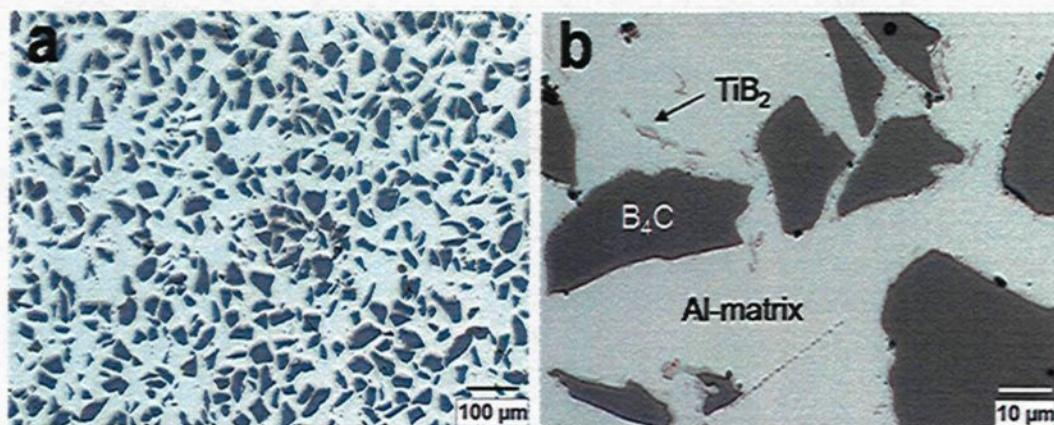


Figure 5.1 Optical micrographs of prefabricated AA1100-25 vol. % B_4C with 2.5 wt. %Ti cast billets.

5.2.2 Microstructures of as-cast composites

5.2.2.1 Optical microstructure

Figure 5.2 and 5.3 show typical microstructures of as-cast Al- B_4C experimental composites. After alloying and remelting, the B_4C particles still remain homogeneously distributed in the Al matrix, and particle agglomeration (cluster) is rarely found. Although the amount of the interfacial reaction products does not increase significantly in the matrix, some reaction products around and close to B_4C particles, generated during the melt preparation can be observed. In all composites containing only Sc (Figure 5.2), no primary intermetallic phases (Al_3Sc) appear in the matrix, although the Sc content in one of the composites (S58) is above the maximum solid solubility of Sc (0.4 wt.%) in aluminum. However, in all Sc-Zr-containing composites (Zr fixed at 0.24 wt.%), a few primary intermetallic particles of Al_3Zr appear in the matrix whose size is similar to that of the B_4C particles (Figure 5.3). EDS analysis detected that a small amount of Ti is retained in these primary Al_3Zr intermetallic particles, where Ti could substitute some Zr atoms in the Al_3Zr

crystals during solidification. The appearance of primary Al_3Zr particles indicates that the concentration of Zr in the matrix is slightly above the maximum solubility of Zr in aluminum, even though some Zr was consumed at the interfaces between B_4C particles and Al (see 5.2.2.2).

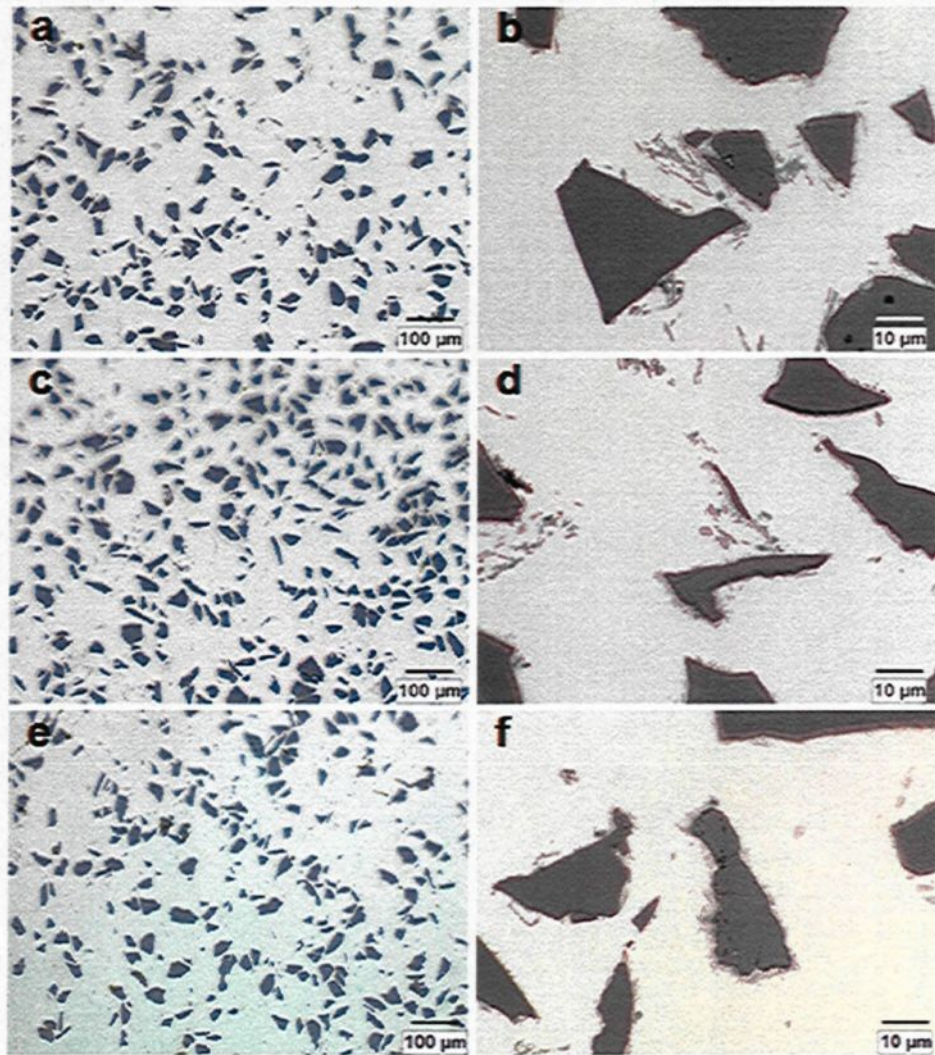


Figure 5.2 Optical microstructures of as-cast composite samples: S58 (a and b), S40 (c and d), and S29 (e and f).

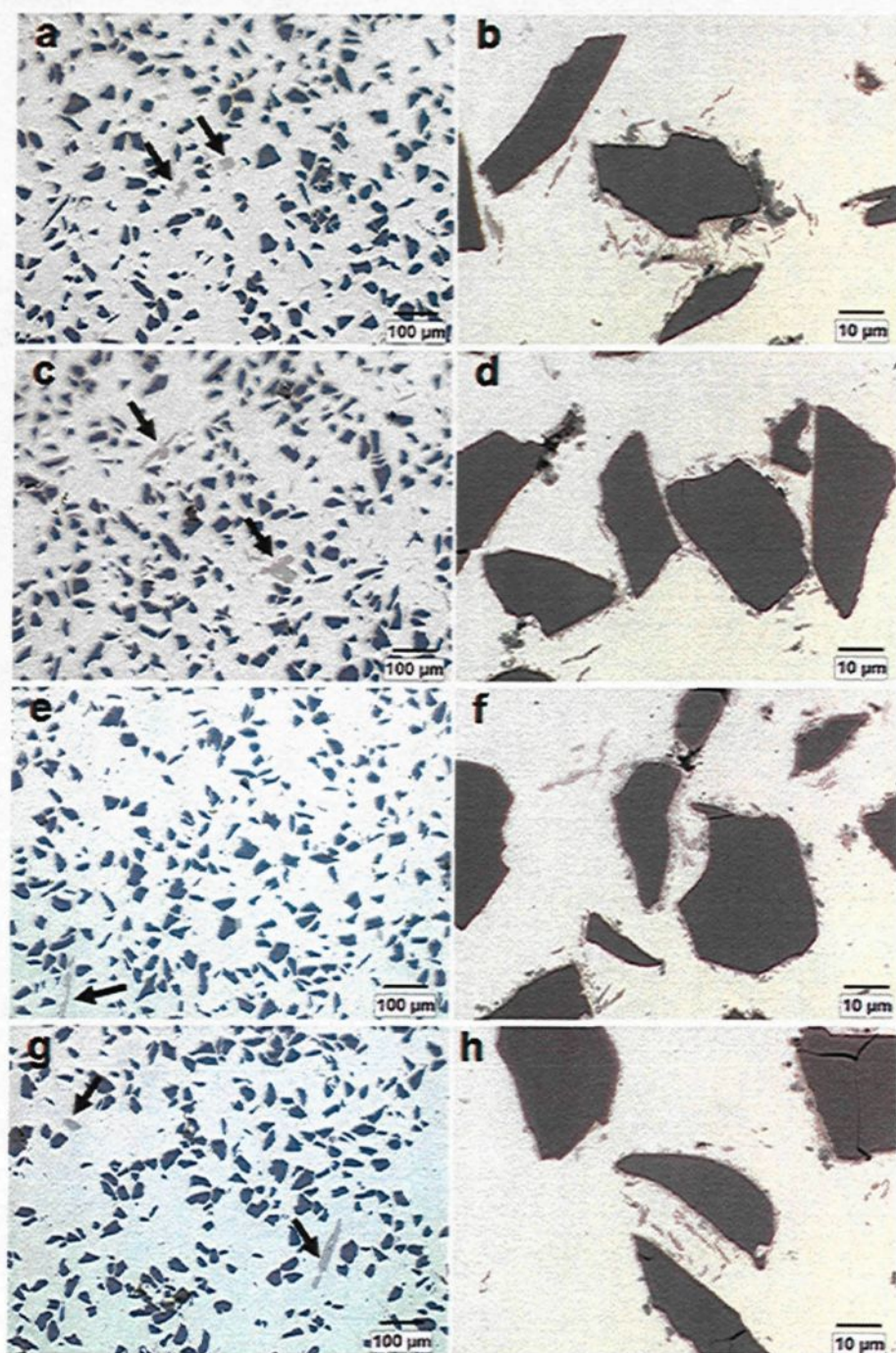


Figure 5.3 Optical microstructures of as-cast composite samples of SZ58 (a and b), SZ40 (c and d), S29 (e and f) and Z24 (g and h). The arrows in a, c, e and g show the primary Al_3Zr intermetallic particles.

5.2.2.2 Interfaces between B₄C and aluminum

The surface of each B₄C particle is covered by a thin interfacial reaction layer (usually less than 1 μm), composed of many reaction particles (Figure 5.4). The majority of those particles are TiB₂ type particles, which have a hexagonal morphology. In a three dimensional view revealed by deep etching (Figure 5.4 b and d), it becomes evident that the thin reaction zone is a continuous layer covering the entire B₄C surface. Moreover, in the interfacial reaction zone, there are some coarse particles (mainly TiB₂) that grow directly from the reaction zone with random orientation and extend into the Al-matrix. EDS analysis shows that these TiB₂ type particles often contain a trace of Sc or Sc and Zr in the Al-Sc and Al-Sc-Zr composites, respectively.

Figures 5.5 and 5.6 show more details of the interfacial microstructures obtained by TEM examination of samples of the composites S58 and SZ58, respectively. In the case of Al-Sc composites (an example of S58), it can be seen from Figure 5.5 a and b that the B₄C surface is covered with a layer of fine crystals attached to the B₄C surface as well as a layer of coarse crystals extending from the fine crystal layer toward the Al-matrix. The fine crystal layer can be divided into two sublayers: one sublayer, light grey in color and adjacent to the surface of B₄C, is enriched in Al, B and C and consists of fine Al₃BC crystals (Figure 5.5 a and c), which also is found in other Al-B₄C composites [25]; The second dark grey polycrystalline sublayer containing Ti, Sc and B, is composed of two types of fine crystals, TiB₂ and ScB₂, as confirmed by the selected area electron diffraction (SAED) pattern taken from in the location I (Figure 5.5 a, c and d). Furthermore, the amount of titanium is much higher than the Sc detected at the interface, indicating that the

second polycrystalline sublayer mainly consists of the fine TiB_2 crystals. In the coarse crystal layer, two compounds are identified. In the location II the plate-like hexagonal particle is recognized as TiB_2 (Figure 5.5 a and e). The faceted particle in location III, growing toward the Al-matrix, is identified as Al_3ScC_3 (Figure 5.5 b and f).

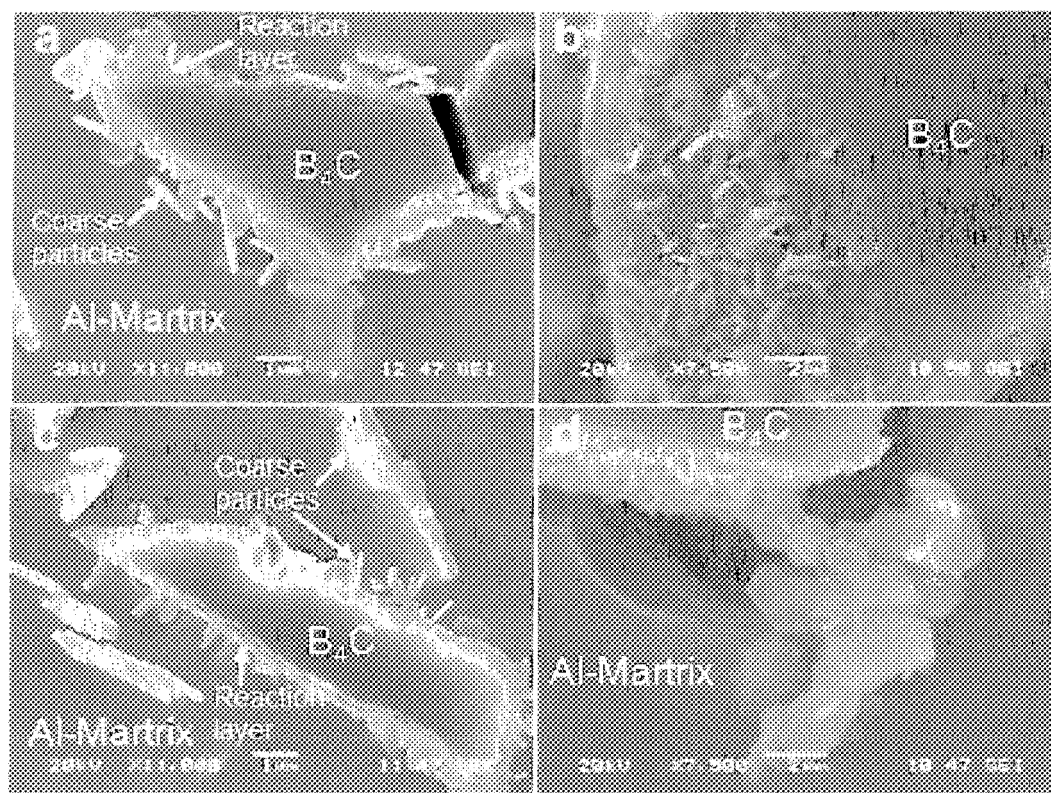


Figure 5.4 SEM micrographs of S58: **a** light-etched, **b** deep-etched; and SZ58: **c** light-etched and **d** deep-etched.

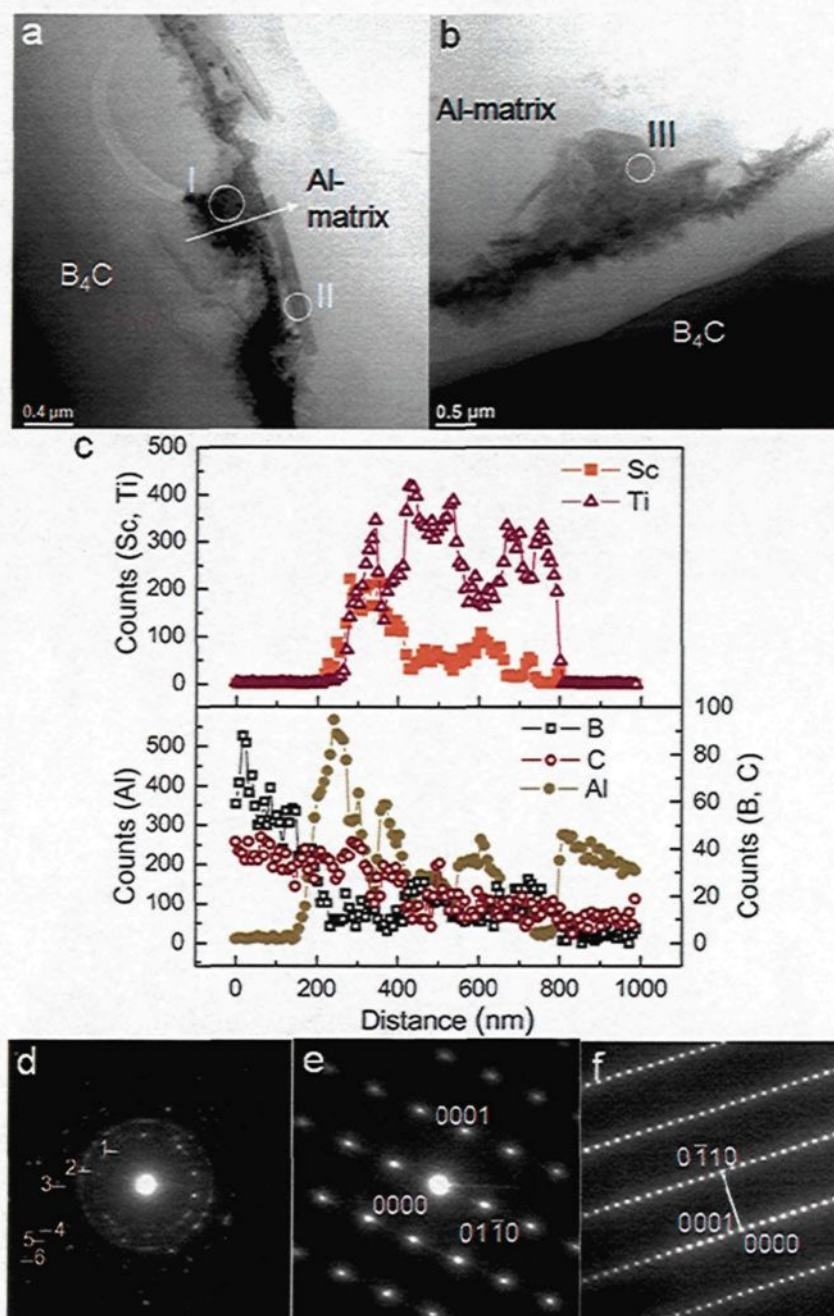


Figure 5.5 **a, b** Bright-field STEM images of typical interfacial morphologies in as-cast composite S58. **c** Composition profiles along the arrow indicated in **a**. **d** SAED ring patterns from selected area I: 1, ScB₂(100); 2, TiB₂(101); 3, TiB₂(110); 4, TiB₂(201); 5, TiB₂(112); 6, ScB₂(211). **e** TiB₂ phase electron diffraction pattern corresponding to the selected area II at the zone axis $[2\bar{1}\bar{1}0]$; **f** Al₃ScC₃ phase electron diffraction patterns corresponding to the selected area III at the zone axis $[2\bar{1}\bar{1}0]$.

The typical microstructure of reaction layers in the Al–Sc–Zr composites (SZ58) is shown in Figure 5.6, which is very similar to that of the Al–Sc composites (S58). At the interface between B₄C and Al, there is a layer of fine crystals attached on the B₄C surface and a layer of coarse crystals adjoining aluminum matrix (Figure 5.6 a and b). In the fine crystal layer, a great number of tiny crystals on the nanoscale covered the entire B₄C surface. Two sublayers exist here: one exhibiting light-grey color close to B₄C is made up of Al₃BC crystals, and one with dark-gray is composed of polycrystalline TiB₂ and ScB₂, identified by the SAED in the location I (Figure 5.6 a and d). Results of EDS line scanning reveal that the dark-gray sublayer is enriched with a high amount of Ti and a small amount of Sc (Figure 5.6 c), suggesting a majority of TiB₂ and a minority of ScB₂ fine crystals in this sublayer. Moreover, a trace level Zr is also detected at the interface. Since the possible reaction product ZrB₂ has the same hexagonal structure as ScB₂ and both compounds have similar lattice constants (for ZrB₂: $a = 3.170 \text{ \AA}$, $c = 3.530 \text{ \AA}$ [184]; for ScB₂: $a = 3.148 \text{ \AA}$, $c = 3.515 \text{ \AA}$ [185]), it is difficult to distinguish them from each other by the selected area diffraction patterns. Therefore, the trace Zr is expected to exist in the following two possible ways: either in the form of ZrB₂ or by substituting some Ti or Sc atoms in the TiB₂ and ScB₂ crystals.

The SAED pattern in location II (Figure 5.6 e) confirms that the large plate-like particles extending into the Al-matrix are TiB₂ type crystals, containing traces of Sc and Zr. The faceted particles toward the Al-matrix are identified as Al₃ScC₃ (Figure 5.6 f).

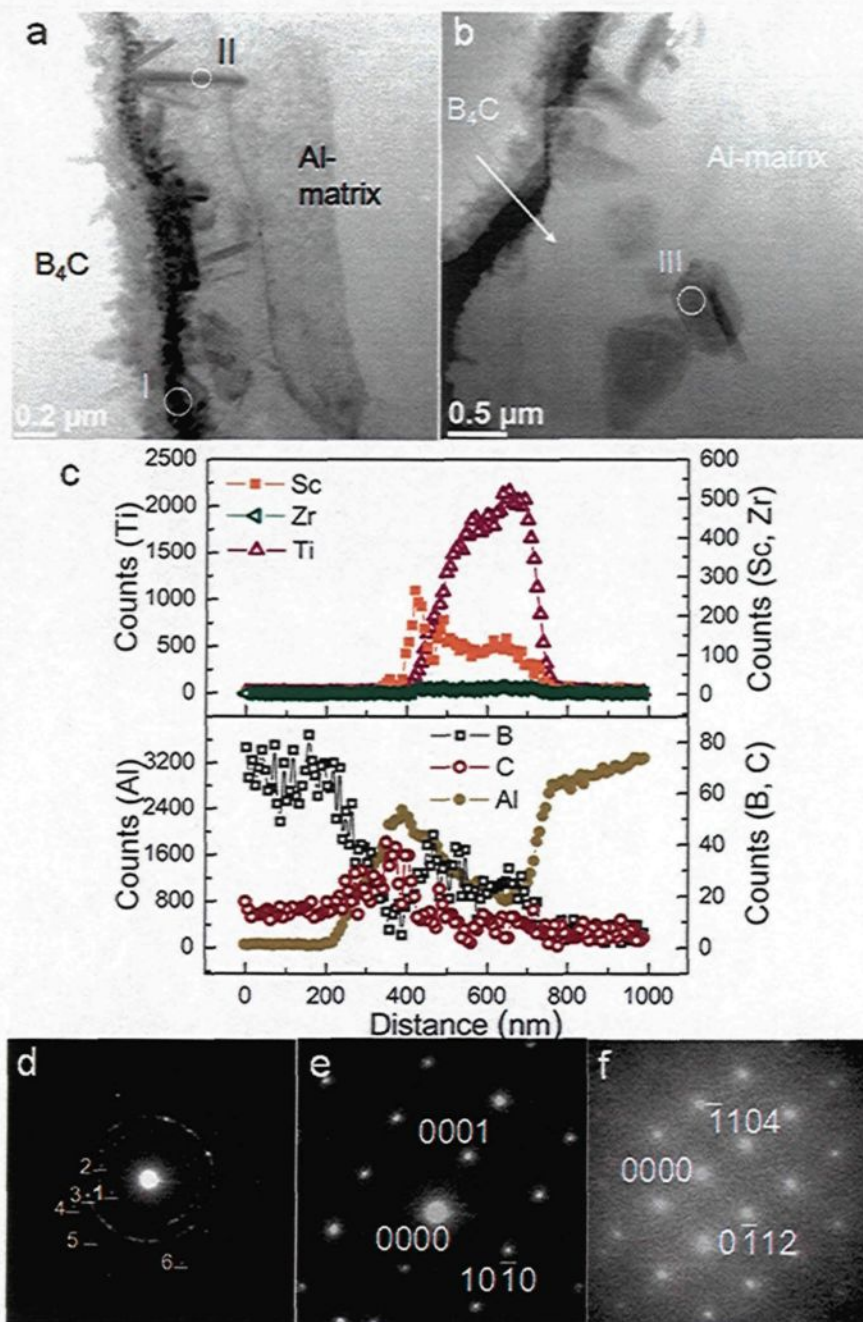


Figure 5.6

a, b Bright-field STEM images of typical interfacial morphologies in as-cast composite SZ58. **c** Composition profiles along the arrow indicated in **b**. **d** SAED ring pattern from selected area I: 1, $\text{TiB}_2(001)$; 2, $\text{ScB}_2(100)$; 3, $\text{TiB}_2(101)$; 4, $\text{TiB}_2(002)$; 5, $\text{ScB}_2(102)$; 6, $\text{ScB}_2(201)$. **e** TiB_2 phase electron diffraction patterns corresponding to the selected area II at the zone axis $[\bar{1}2\bar{1}0]$. **f** Al_3ScC_3 phase electron diffraction patterns corresponding to the selected area III at the zone axis $[10\bar{2}83]$.

It is interesting to observe that the highest peak of Sc in both composites (S58 and SZ58) is very close to B_4C and lies in front of the fine TiB_2 layer. It suggests that Sc atoms are able to diffuse across the existing TiB_2 layer formed in prefabricated cast billets.

5.2.2.3 Precipitates in the as-cast condition

Figure 5.7 displays TEM micrographs of the as-cast precipitates of Al_3Sc and $Al_3(Sc,Zr)$ in the as-cast composites of S58 and SZ58, respectively. The Al_3Sc precipitates in the Al–Sc composite (S58) exhibit spheroidal morphology and are distributed homogeneously in the Al-matrix (Figure 5.7 a). They have an average radius of 3.0 ± 0.9 nm and a volume fraction of 0.14%. The Al–Sc–Zr composite (SZ58) produces a combination of spheroidal and cellular-cubic precipitates, $Al_3(Sc,Zr)$, see Figure 5.7b and c. The $Al_3(Sc,Zr)$ precipitates have an average radius of 3.4 ± 1.7 nm (spheroidal shape) and 8.7 ± 4.1 nm (cellular-cubic shapes), respectively. The total volume fraction of the precipitates is 0.29%. In comparison to the Al–Sc composite, the effect of Zr addition on the precipitate volume fraction is obvious. At the same Sc level, the Al–Sc–Zr system produces approximately twice the amount of precipitates, which has a significant impact on the precipitation hardening.

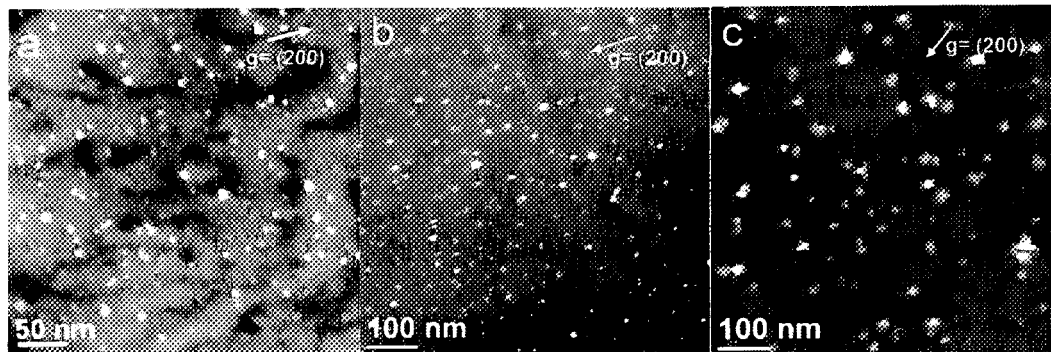


Figure 5.7 Dark-field TEM images showing the precipitates in the matrix of the composites S58 **a** and SZ58 **b** and **c**.

In general, such precipitates in the nanometer scale distribute uniformly in the matrix. However, a precipitate free zone (PFZ) is observed both near the grain boundaries (Figure 5.8) and close to the front of the interfaces of ceramic particles (Figure 5.9). The width of the PFZ near the grain boundaries in the Al–Sc composite (S58) varies in a range of 50–200 nm. As phenomenon is also found in the Al–Sc–Zr composite (SZ58). Generally, the formation of PFZs at grain boundaries can be explained by the depletion of solute elements or vacancies since the lack of solute elements or vacancies makes it difficult for precipitate nucleation to occur [186, 187].

In the area adjacent to the interfaces of the ceramic particles, a precipitate free zone with a width of 2 to 2.5 μm can be clearly identified (Figure 5.9). A similar PFZ is also observed in the Al–Sc–Zr composite (SZ58). It is worth mentioning that the width of the PFZ at the interface is much wider than that at the grain boundaries. In the interfacial microstructure (Figure 5.5 and 5.6), it is found that a considerable amount of Sc is present in the interfaces for both composites. These Sc atoms react with B_4C and are fixed at the

interface, thereby removing sufficient solute from the adjacent zone. This solute-depleted region near the interface finally becomes the PFZ.

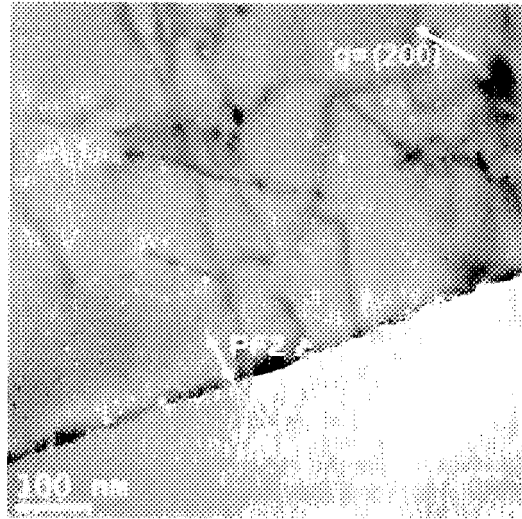


Figure 5.8 A precipitate free zone existed near the grain boundary (S58) using the superlattice reflection (100) of Al_3Sc particles near the [100] zone axis.

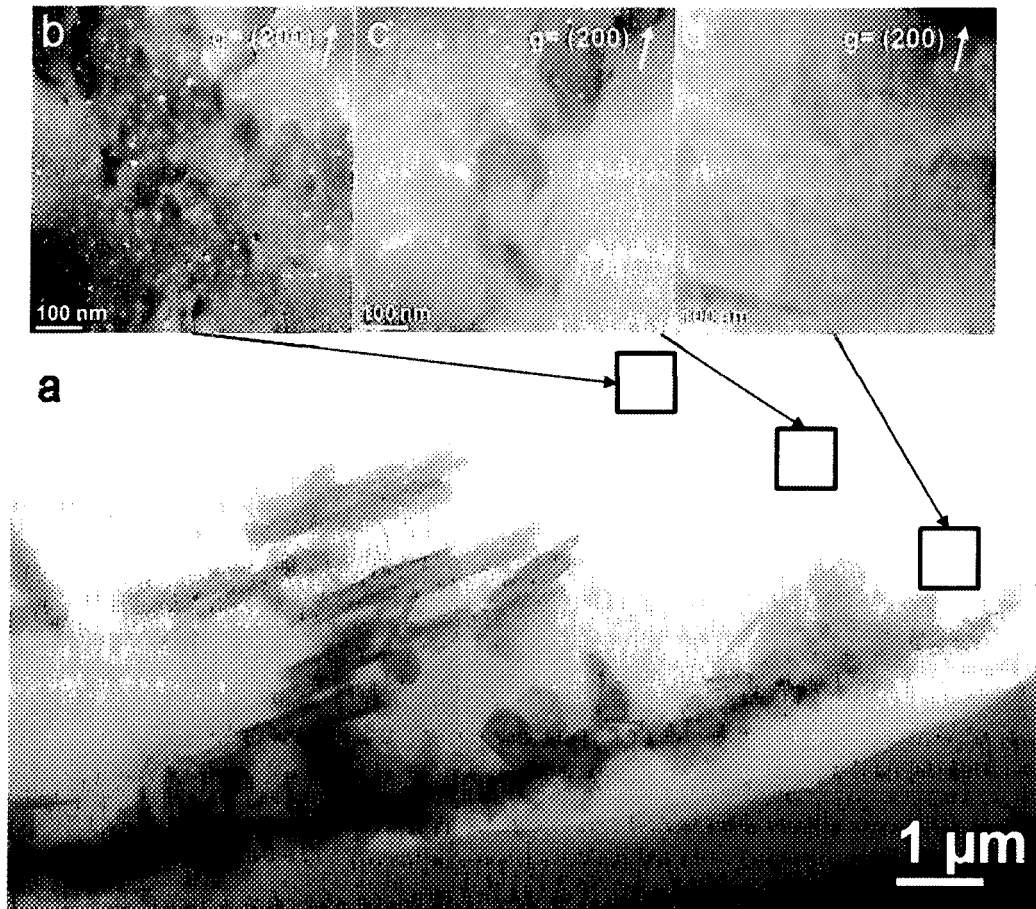


Figure 5.9 A precipitate free zone at the interface of the composite S58. **a** bright-field STEM image of the interface; **(b, c, and d)** enlarged dark-field images of zoom-in areas (squares) in **(a)** taken from locations away from the interface by $4.5\ \mu\text{m}$, $2.5\ \mu\text{m}$ and $300\ \text{nm}$, respectively.

5.2.3 Precipitation strengthening

The precipitation strengthening effects on the Al-matrix of all experimental composites were monitored by Vickers hardness measurements. The hardness values of the composites in as-cast, as-homogenized, and peak-aged conditions are illustrated in Figure 5.10. No precipitation strengthening is observed in the base composite due to the absence of any precipitate in its matrix. The addition of Zr to the base composite (Z24) produces no

strengthening effect in both as-cast and homogenized conditions. But it shows a limited precipitation hardening in the peak-aged condition, probably due to the precipitation of a small amount of Al_3Zr precipitates in the matrix [188]. The Al–Sc composites (S29, S40 and S58) exhibit an obvious strengthening effect in both as-cast and peak-aged conditions. The higher the scandium level, the higher the strengthening effect exhibited by the composites. Moreover, a pronounced synergistic effect on the precipitation strengthening is observed when both Sc and Zr are present (SZ29, SZ40 and SZ58). Each Al–Sc–Zr composite produces higher hardness values than the corresponding Al–Sc composite in both as-cast and peak-aged conditions. For example, the microhardness values of the composite S29 are 38 HV and 45 HV while the composite SZ29 exhibits hardness values of 42 HV and 60 HV in the as-cast and peak-aged condition (300 °C), respectively. The hardness values of the latter are increased by 11% in as-cast condition and 33% in the peak-aged condition compared to the former.

It is worth noting that the hardness values of all homogenized composites are back to the similar low level as that of the base composite, indicating that all precipitates formed in the as-cast condition can be completely dissolved during homogenization. Certainly, they reappear in the matrix during the aging process and produce higher hardness values in the composites.

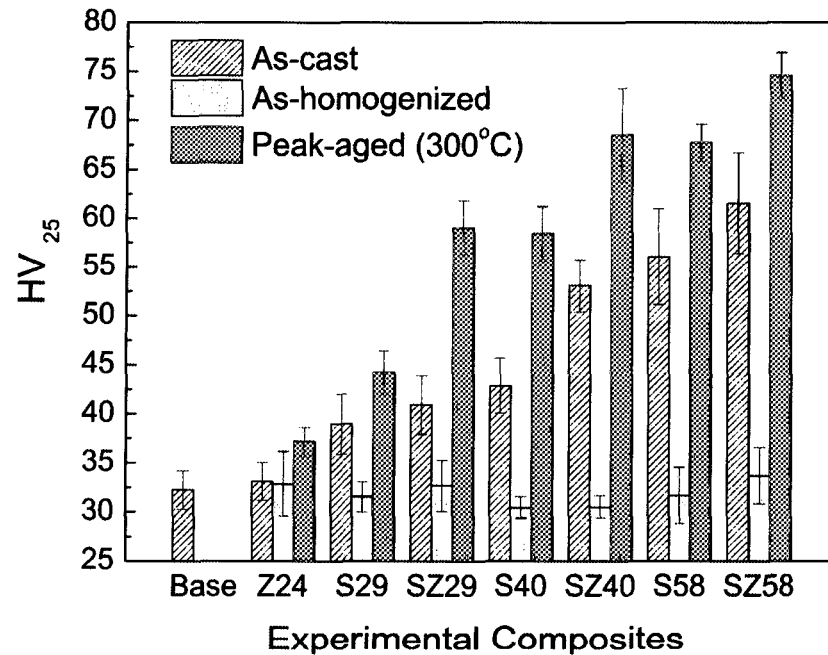


Figure 5.10 Vickers microhardness of the matrix of experimental composites in as-cast, as-homogenized and peak-aged conditions.

5.3 Discussion

5.3.1 Interfacial reactions

In the Al–B₄C system, B₄C is not stable in liquid aluminum [28, 29, 160]. During melting and casting, B₄C continually decomposes, which decreases the fluidity during casting and deteriorates the mechanical properties [25, 26]. With the addition of Ti to the Al–B₄C composites, the interfaces between Al and B₄C becomes enriched in Ti and the following reaction takes place [26]:



The reaction products, Al_3BC and TiB_2 , build a protective layer surrounding the B_4C surface to restrain the decomposition of B_4C [25, 26, 152]. The prefabricated AA1100–25 vol.% B_4C cast billets containing 2.0 wt.% Ti, and all B_4C particles in this material were covered by this interfacial reaction layer.

Sc and Ti are adjacent transition elements in the periodic chart, and they show similar behavior in liquid aluminum. When Sc is introduced into the Ti-saturated composites, it is found that Sc concentrates at the interfaces and is involved in interfacial reactions with B_4C . In addition to the interfacial reaction (5.1), the following reaction with Sc also occurs.



The four reaction products formed in the interfacial layer are confirmed by TEM to be, Al_3BC , TiB_2 , ScB_2 and Al_3ScC_3 (Figure 5.5 and 5.6). The *in-situ* interfacial layer constitutes two sublayers: a fine crystal layer close to the B_4C consisting of Al_3BC , TiB_2 and ScB_2 , and a coarse crystal layer adjacent to the Al-matrix made up of TiB_2 and Al_3ScC_3 . EDS results indicate that the major compound is TiB_2 , besides which, two minor amount of ScB_2 and Al_3ScC_3 co-exist in the interfacial layer. These Sc-containing reaction products may bring some benefit by further stabilizing B_4C and preventing B_4C from the decomposition during melting. However, the interfacial reaction consumes a considerable amount of Sc, which is no longer available for the precipitation strengthening.

When Zr, in combination with Sc, is added in Al– B_4C composites, only a trace level of Zr is detected in the interfacial reaction zones and no major Zr reaction product is recognized by TEM (Figure 5.6). The consumption of Zr at the interfaces should be very

limited so that most Zr atoms are retained in the matrix, which is essential for precipitation hardening.

5.3.2 Solute concentration of Sc and Zr in the matrix

The precipitation strengthening of the composite relies on the solute concentration of Sc and Zr in the matrix. However, there is no effective method to precisely quantify the amount of alloying elements retained in the Al-B₄C composite matrix. It is well known that, during the aging process, the precipitation strengthening depends on the volume fraction and the size of the precipitates in the material which is in turn controlled by the solute concentration and the aging temperature [33, 52, 60]. Therefore, materials with the same peak value at a given aging temperature would have similar alloying element concentrations. Based on this principle, we compare the peak hardness obtained at 300°C in a series of the binary Al-Sc alloys reported in the literature [18, 19, 84, 106, 108, 109] with the values obtained in the experimental composites. The equivalent concentration of Sc and Zr in the matrix may therefore be assessed (Figure 5.11).

For the Al-Sc composites, the peak microhardness values of the S29 (0.29 wt.% Sc), S40 (0.40 wt.% Sc) and S58 (0.58 wt.% Sc) composites are equivalent to those values exhibited by binary Al-0.15, 0.2 and 0.3 wt.% Sc alloys. It suggests that approximately half of the Sc is retained in the matrix for the precipitation hardening while the other half is consumed at the interfaces. In other words, doubling the Sc amount is necessary in Al-B₄C composites to achieve the same strengthening effect in binary Al-Sc alloys. The higher the

strength level of the composites required, the more the Sc consumed in the interfaces, and as a consequence, the higher the concentration of Sc needed.

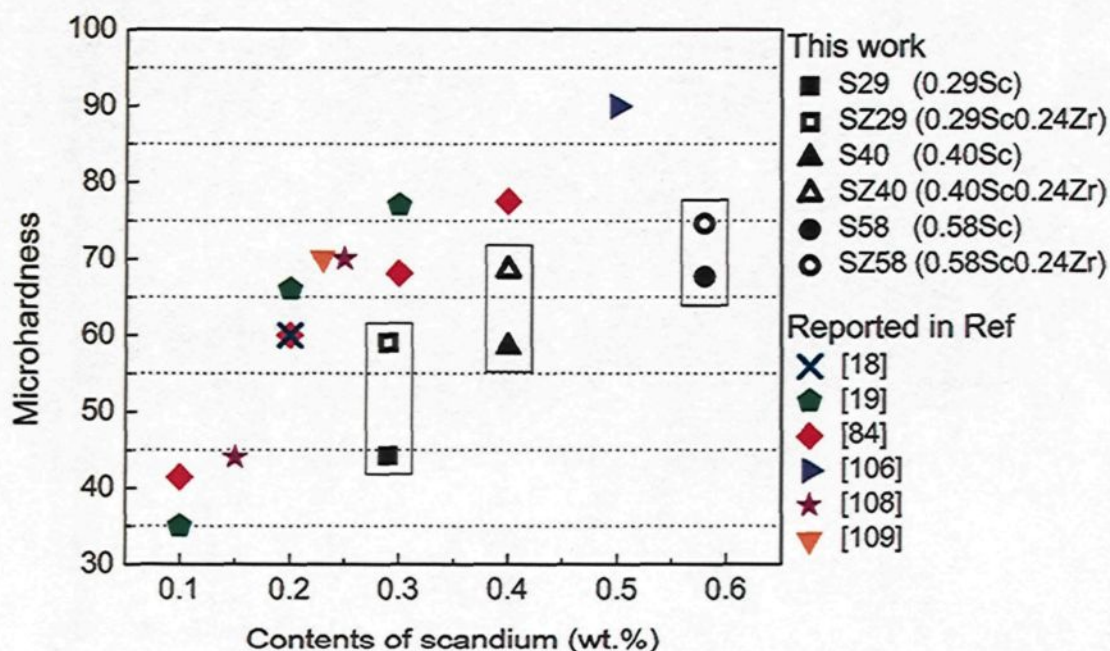


Figure 5.11 Peak microhardness at 300 °C vs. Sc concentration of experimental composites in comparison with that reported in binary Al-Sc alloys.

With respect to the Al-Sc-Zr composites, a few primary Al_3Zr particles appear in the cast microstructure (Figure 5.3), which indicates that some Zr is bounded in the primary Al_3Zr crystals upon solidification. According to the Al-Zr binary diagram, primary Al_3Zr will form when Zr content is higher than approx. 0.11 wt.% at the peritectic reaction [189]. Under non-equilibrium solidification conditions, the peritectic reaction shifts towards a higher Zr concentration and more Zr can enter the Al-matrix upon solidification to form a supersaturated solid solution. During the present experimental casting procedures, the cooling rate in liquid state (730 to 660°C) is about $12\text{ }^\circ\text{C}\cdot\text{s}^{-1}$ (Table 5.1), which is a normal

cooling condition for permanent mold casting and direct chill (DC) casting. In such non-equilibrium conditions, the solute content of Zr after solidification is estimated around 0.15 wt. %.

Results of Figure 5.11 show that, in all three Al–Sc–Zr composites (SZ29, SZ40 and SZ58), the presence of Zr generates a strengthening effect that is more or less equivalent to that of 0.1 wt. % Sc in the binary Al–Sc alloys after homogenization and aging. It is reported that [114, 190], based on the precipitate volume, two times the Zr concentration is needed to achieve a similar precipitation effect of Sc in aluminum alloy, *i.e.*, the precipitation hardening effect of 0.2 wt. % Zr in aluminum is equivalent to that of 0.1 wt. % Sc. Again, based on the Al–Zr binary diagram, the maximum solid solubility of Zr in Al at 640°C lies around 0.23 wt. % [189]. All three composites experienced a homogenization treatment at 640°C for 96 h. Considering that a small part of Zr is consumed at the interfaces but some primary intermetallics Al_3Zr are dissolved during the long homogenization time, the solute concentration of Zr in the matrix after heat treatment is assessed to be about 0.20 wt. %, which is higher than that in the as-cast condition.

5.3.3 Precipitation strengthening in as-cast condition

The cooling conditions of the experimental ingots are listed in Table 5.1. To achieve precipitation strengthening in the as-cast condition, the formation of supersaturated solid solution upon solidification and the precipitation of coherent precipitates during the subsequent cooling are both of importance. The solid solubility of Sc in aluminum is very low and it decreases sharply with decrease in temperature. For example, the solid solubility

of Sc is 0.30, 0.05 and 0.005 wt.% at 640, 500 and 350°C respectively [89]. In spite of the partial consumption of Sc at the interfaces, approximately 0.15, 0.2 and 0.28 wt. % Sc is still remained in the matrix of the three composites and forms the supersaturated solid solution upon solidification.

Table 5.1 Measured cooling rates of cast ingots from 730 °C to 300 °C

Temperature range (°C)	Average cooling rate (°C·s ⁻¹)
730-660	12.4
650-500	4.3
500-300	0.8

During the subsequent cooling, if the cooling rate in the solid state is not high enough to exhibit a quench effect, the supersaturated solid solution decomposes. It is reported that when the cooling rate in the solid state is below 10 °C·s⁻¹ in Al–Sc alloys, the nano-size precipitates are able to generate from the supersaturated solid solution and display precipitation-strengthening of the matrix [114, 190]. Therefore, precipitation occurs in the experimental composites in the as-cast condition based on their appropriate cooling rates (Table 5.1). The precipitates, Al₃Sc and Al₃(Sc,Zr), uniformly distributed in the matrix of the respective composite (Figure 5.7), indicating that a quick nucleation and growth of precipitates occurred during cooling. Taking into account that the cooling time from 500 to 300°C of the experimental composites is about 7 minutes, the incubation time is quite short, which might be attributed to the excess vacancies in the metal matrix composites. It is suggested that the vacancies may enhance the diffusion of Sc in the Al matrix, and that the vacancy clusters act as heterogeneous nucleation sites for Al₃Sc and Al₃(Sc,Zr) precipitates

[89]. Due to the presence of Zr, the as-cast Al–Sc–Zr composite (SZ58) produces double the amount of precipitates as the Al–Sc composite at the same level of Sc level. Therefore, the precipitation hardening effect of Al–Sc–Zr composites is remarkably higher than that of Al–Sc composites in the as-cast condition. It should be noticed that the as-cast hardness is generally lower than that at the peak-aged condition (equivalent to 70–90% of the value at peak aging), due to a short time during cooling (in the order of several minutes), which does not allow a complete precipitation.

5.4 Summary

In the present study, B₄C particulate reinforced aluminum matrix composites alloyed with varied Sc contents of 0.29, 0.40 and 0.58 wt.% and a fixed Zr content of 0.24 wt.% were fabricated by the conventional casting process. The interfacial microstructure, precipitation of Al₃Sc and Al₃(Sc,Zr) as well as the precipitation strengthening effect in the as-cast and peak-aged conditions were investigated. The following results and findings were obtained and discussed.

When Sc is added to the Ti-presaturated Al–B₄C composites, Sc concentrates at the interfaces and is involved in the interfacial reactions with B₄C. The *in-situ* interfacial layer formed enclosing the whole B₄C surface consists of two sublayers: a fine crystal layer close to the B₄C, consisting of Al₃BC, TiB₂ and ScB₂, and a coarse crystal layer in the proximity of the Al-matrix, made up of TiB₂ and Al₃ScC₃. The interfacial reactions consume a considerable amount of Sc which is then no longer available for precipitation strengthening.

A trace level of Zr is detected at the interfacial reaction zone when Zr is added in combination with Sc to the Al-B₄C composites. No major Zr reaction product is found at the interfaces. Therefore, only a small part of Zr is consumed at the interfaces while the major part of Zr is retained in the matrix for precipitation strengthening.

Precipitation of nanoscale Al₃Sc and Al₃(Sc,Zr) precipitates are observed in the as-cast microstructure. Both precipitates are formed during cooling after solidification and are uniformly distributed in the aluminum matrix except near the grain boundary areas and in front of the interfaces between Al and B₄C where the PFZs are found.

The introduction of Sc in Al-B₄C composites yields a considerable precipitation strengthening effect in as-cast and peak-aged conditions. With increased Sc content, the precipitation strengthening of the composites increases but the consumption of Sc at the interfaces is also increased. To achieve an equivalent strengthening effect of Sc as that produced in binary Al-Sc alloys, approximately twice the amount Sc is required in the case of Al-B₄C composites.

The addition of Zr to the Sc containing composites produces a high volume fraction of Al₃(Sc,Zr) precipitates which enhances the significant strengthening of Al-B₄C composites in both as-cast and peak aged conditions.

CHAPTER 6

PRECIPITATION STRENGTHENING DURING ISOTHERMAL AGING AT 300 – 450 °C

Chapter 6

Precipitation strengthening during isothermal aging at 300 – 450 °C

6.1 Introduction

In the last two chapters, the feasibility of manufacturing Al-B₄C composites with the additions of scandium and zirconium was demonstrated. Results showed that some Sc and Zr were enriched at Al-B₄C interfaces while certain amount of both elements retained in Al-matrix. Therefore, the objectives of the present chapter is to investigate the effects of Sc and Zr on the precipitation strengthening of Al-B₄C composites. The produced experimental composites were homogenized at the temperatures of 635 to 640°C (see 3.2.1) and were quenched into water. The subsequent aging processes were applied at a temperature range from 300 to 450°C for up to 200 h (Table 3.4). The thermal stability and coarsening resistance of Al₃Sc and Al₃(Sc,Zr) precipitates are also assessed. In addition, the coarsening behavior of the precipitates and their related strengthening mechanisms are discussed.

6.2 Results

6.2.1 Age hardening response

6.2.1.1 Al–Zr composites

Figure 6.1 shows the age hardening curves of the Zr-containing composite (Z24) at 300 and 450 °C. At the higher temperature (450°C), the composite does not show any age hardening response. At the lower aging temperature (300°C), the composite displays a slight hardening effect. The value of the hardness increases from 33 HV (as-homogenized) to 37 HV, which is attributed to a possible precipitation of Al_3Zr precipitates [188]. In the dilute Zr corner of the Al–Zr system, the system experiences a peritectic reaction with low liquid solubility of Zr. This peritectic reaction favors the formation of the primary Al_3Zr intermetallics and reduces the Zr concentration in the solid solution. The attainable strengths of Al–Zr alloys are therefore limited. It is reported that, to yield an acceptable increase of hardness during the aging process, a minimum concentration of 0.3 wt.% Zr and a cooling rate of 100 °C/s are required [92], which is not satisfied in the case of conventional casting.

It should be mentioned that all eight experimental Al– B_4C composites used in this study contained a relatively large amount of Ti (1.50 wt.%). The addition of such a large level of Ti amount is necessary to prevent the B_4C degradation and increase the castability by forming an *in-situ* protective TiB_2 layer on B_4C surfaces [5, 25, 26, 152]. Almost all of the Ti reacts and is consumed at the interfaces between Al and B_4C . Moreover, considering the relatively low liquid solubility but high solid solubility of titanium in the Al-rich corner,

the free titanium remaining in the solid solution exhibits no strengthening effect in the dilute Al-Ti alloys [11]. Moreover, in our preliminary study, no synergistic hardening effect of Ti with Zr or Ti with Sc and Zr was found in the Al-B₄C composites. Thus, titanium is not considered here as an alloying element for precipitation hardening.

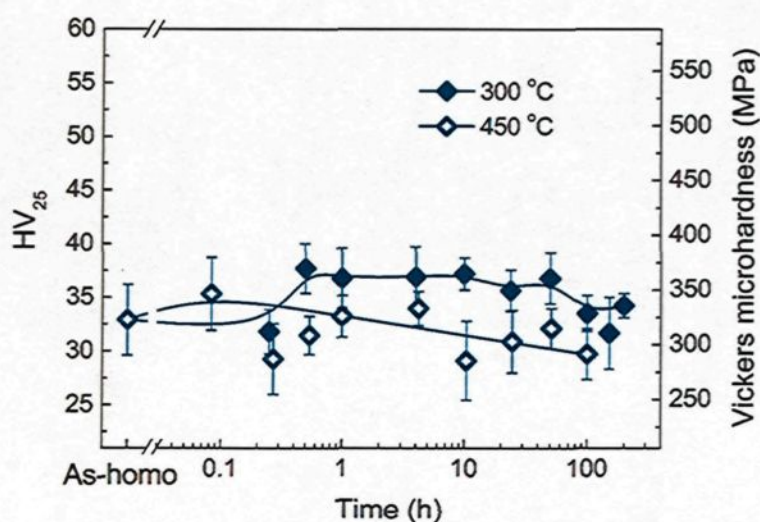


Figure 6.1 Aging curves of the Al-Zr composite (Z24) at 300 and 450°C.

6.2.1.2 Al-Sc composites

Figure 6.2 displays the microhardness of three Al-Sc composites as a function of aging time at four different temperatures of 300, 350, 400 and 450°C. As observed in Figure 6.2, the aging curves of the three composites exhibit the classical features of the aging response which include three regions: (1) an initial increase in hardness (underaging); (2) the maximum hardness value (peak aging); and (3) a decrease in hardness (overaging). In general, the onset of peak hardness, the peak hardness value, and its duration vary with the aging temperature and Sc concentration.

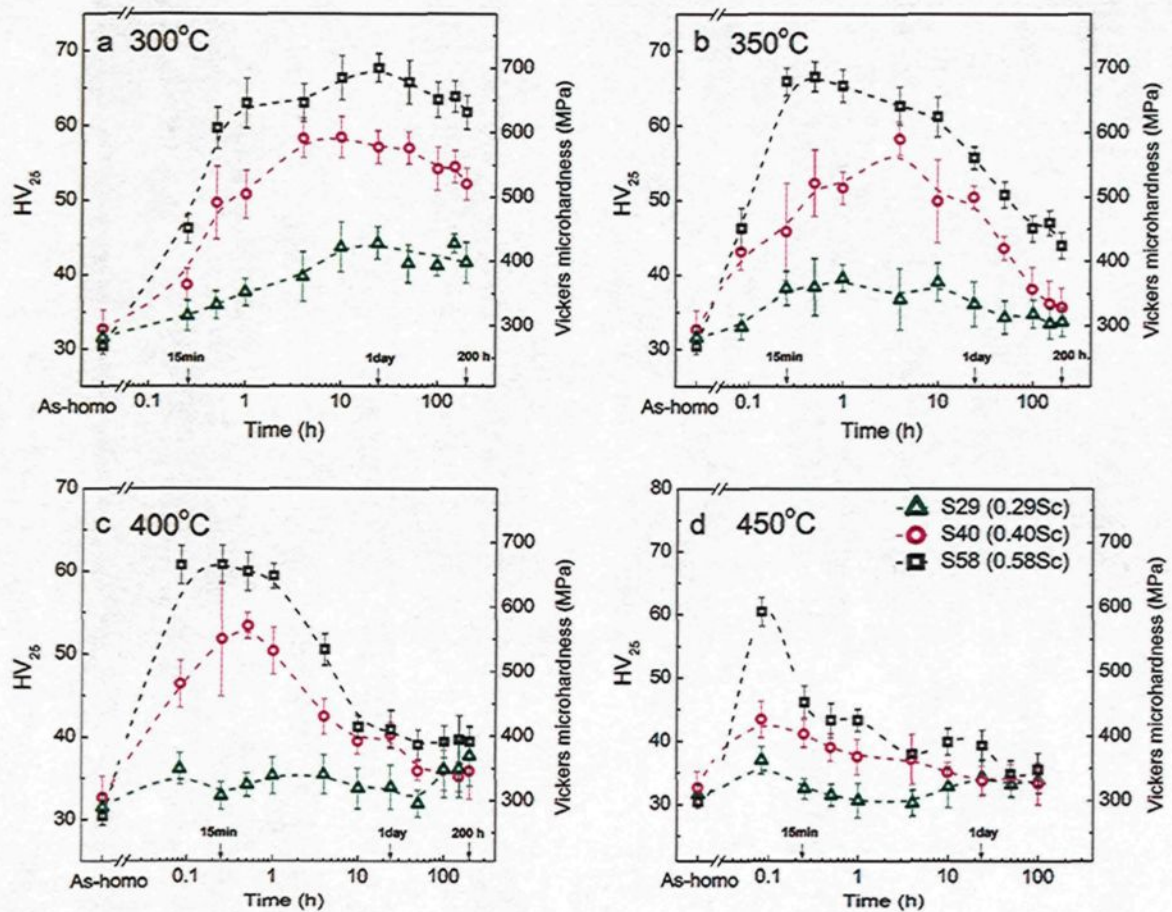


Figure 6.2 Vickers hardness vs. aging time at: **a** 300 °C, **b** 350 °C, **c** 400 °C and **d** 450 °C for the three Al-Sc composites.

It is obvious that the introduction of scandium yields a considerable increase in hardness. The peak hardness values increase with increasing Sc concentration at all aging temperatures. The higher the Sc content, the larger the increase in the hardness. For example, at 300 °C, the hardness increases of 40, 79 and 122% at peak-aging over the unstrengthened matrix (as-homogenized) of composites S29, S40 and S58, respectively. The peak hardness decreases with the increasing aging temperature due to the reduction in the volume fraction of Al₃Sc precipitate caused by the temperature dependence of the solid

solubility of Sc. Higher temperatures provide more energy for the nucleation and growth of precipitates, leading to not only the acceleration in achieving maximum hardening but also the occurrence of overaging.

Results of Figure 6.2 show that the strongest hardening effects of all three Al–Sc composites are achieved at the lowest aging temperature of 300°C. At this temperature, as the aging time increased to 200 h, a slight softening (10 % reduction from the peak hardness value) is noticed in the two higher content Sc-containing composites. Nevertheless, all three composites are still considered to be thermally stable at this temperature for at least middle-term holding time (tens of hours). When the aging temperature rises to 350°C, overaging occurs and the drop in hardness becomes obvious for the three composites. The higher the Sc concentration, the earlier the onset of overaging. The composite materials are no longer thermally stable at this temperature. At higher aging temperatures (400 and 450°C), the softening effect speeds up and all composite materials lose almost all their precipitation hardening after a short time of aging (few to tens of minutes).

6.2.1.3 Al–Sc–Zr composites

Figure 6.3 shows the aging curves of the three Al–Sc–Zr composites at four different temperatures of 300, 350, 400 and 450°C. Compared to the aging curves of the Al–Sc composites (Figure 6.2), the aging hardening responses of Al–Sc–Zr composites show some similarities, namely the peak aging hardness increases with the increasing concentration of solute elements and decreases with increase in aging temperature.

However, the addition of Zr to the Sc-containing composites not only produces a synergistic effect of the increase in strength, but also significantly improves the thermal stability.

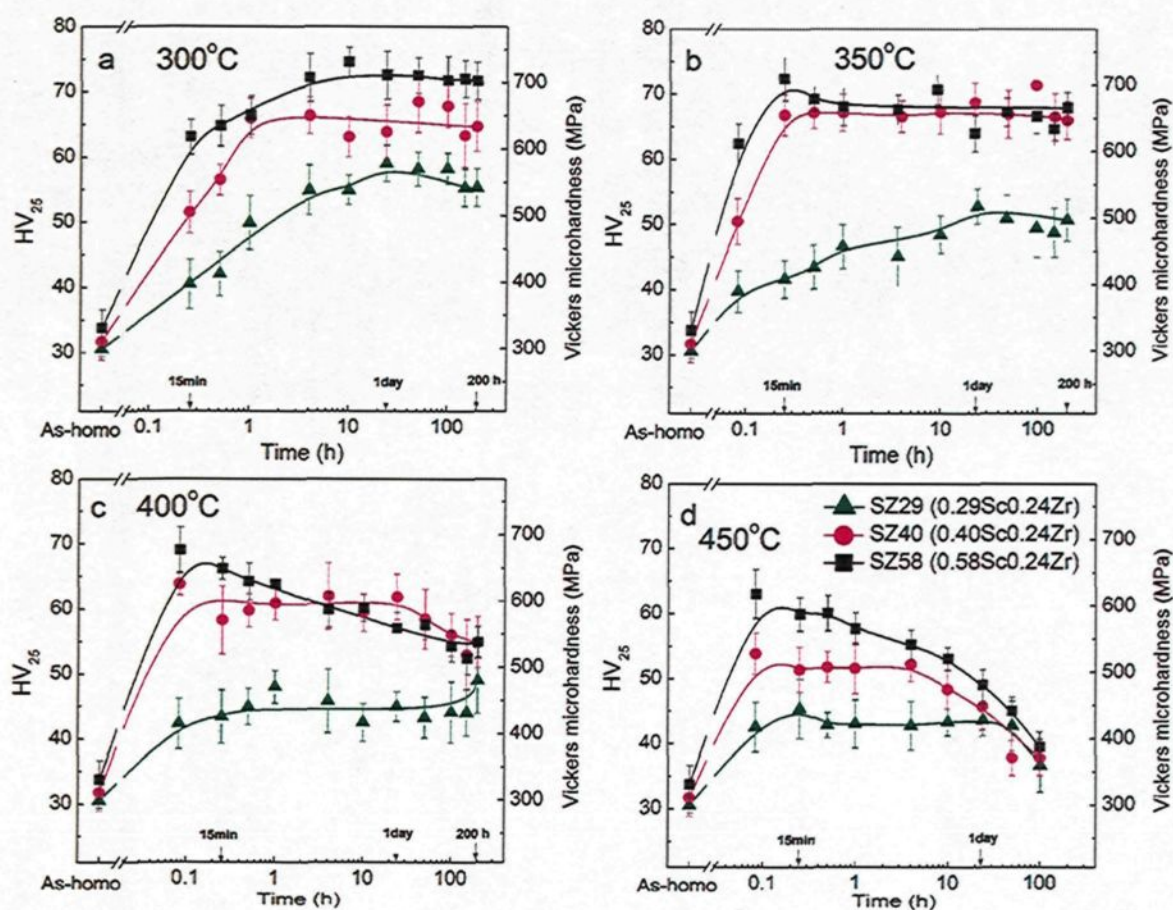


Figure 6.3 Vickers hardness vs. aging time at: a 300 °C, b 350 °C, c 400 °C and d 450 °C for the three Al-Sc-Zr composites.

Figure 6.4 demonstrates the hardness increment in peak aging for the three Al-Sc-Zr composites. The increments are calculated by subtracting the as-homogenized hardness values from the peak hardness values. It is obvious that the addition of zirconium yields

higher hardness increments at all age temperatures. Moreover, the improvement of the peak-age hardening varies with the Zr:Sc ratio. As was estimated in Chapter 5, the three Al–Sc–Zr composites SZ29, SZ40 and SZ58 have approximately 0.2 wt.% Zr and 0.15, 0.2 and 0.28 wt.% Sc retained in the matrix, and Zr:Sc ratios of 1.33, 1 and 0.7, respectively. It can be seen from Figure 6.4 that with an increasing Zr:Sc ratio, the precipitation hardening efficiency also increases. For example, compared to the corresponding Al–Sc series composites, the SZ29 composite (Zr:Sc = 1.33) has the highest hardness increment while the SZ58 composite (Zr:Sc = 0.7) has the lowest one when the same Zr content of 0.24 wt.% is alloyed.

Nevertheless, the addition of zirconium makes an important contribution to the thermal stability. As shown in Figure 6.3, all three Al–Sc–Zr composites keep the strength stable at the aging temperatures of 300 and 350°C. As the aging temperature rises to 400°C, the SZ58 composite shows an overaging tendency while both composite SZ40 and SZ29 are still reasonably stable. Compared to the Sc-containing composites S40 and S29, the Zr addition in SZ40 and SZ29 composites delays the overaging by ~100°C, which indicates that Al(Sc,Zr) precipitates are coarsening resistant up to 400°C. At higher age temperature (450°C), all three composites exhibit overaging, but the composite SZ29 still shows a softening resistance up to about 50 hours.

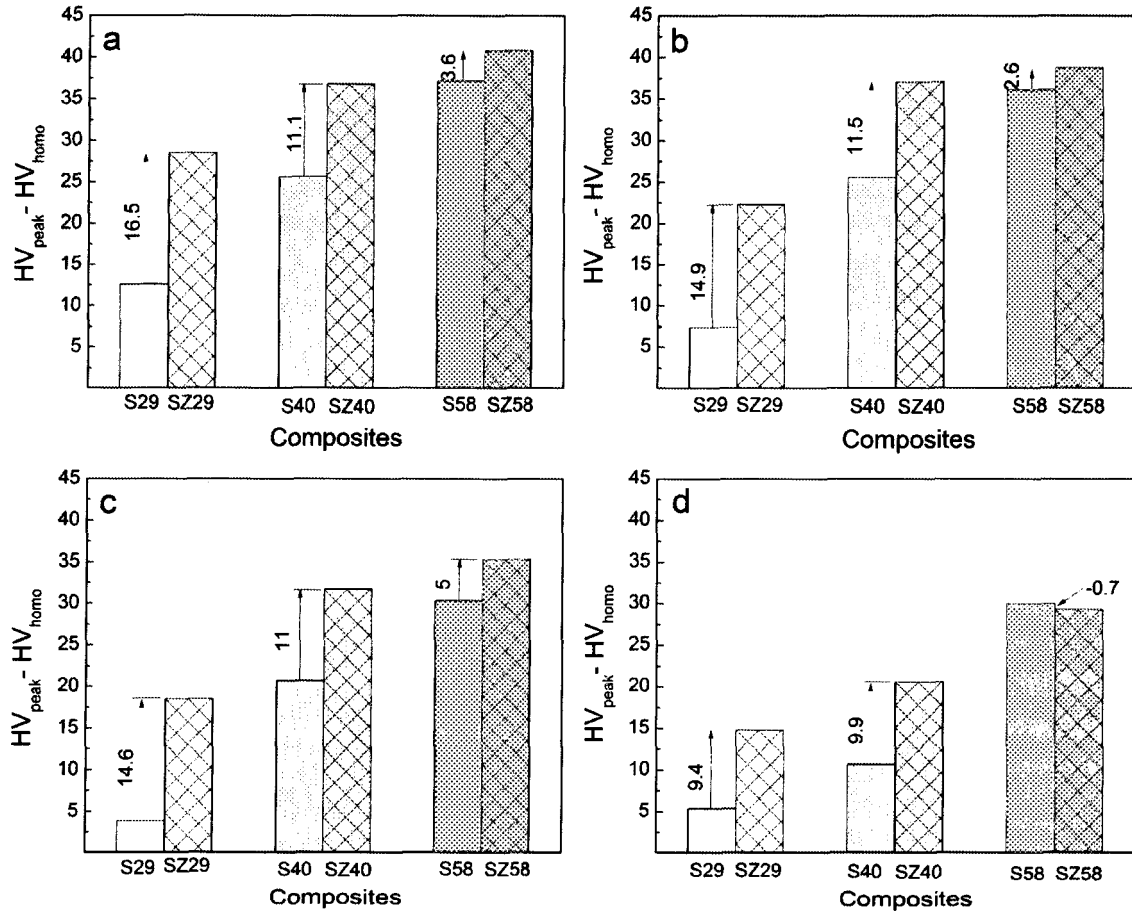


Figure 6.4 Hardness increment of the peak aging for the six Al-Sc and Al-Sc-Zr composites isothermally aged at **a** 300, **b** 350, **c** 400 and **d** 450 °C.

It is also evident that the thermal stabilities of the composites are dependent on the Zr:Sc ratio. The SZ29 composite with the highest ratio (Zr:Sc > 1) provides the best thermal stability of the strength up to 400°C. In practical terms, the service temperature of this material can be maintained to 400°C at a reasonable strength (HV ~450 MPa) and can be occasionally raised to 450°C for a short period without the strength deterioration. The composite SZ40 with a Zr:Sc ratio of ~1 also affords excellent thermal stability with an

enhanced strength (HV ~650 MPa) at 350°C. The service temperature of composite SZ40 is stable at 350°C and can be increased to 400°C for a short-term exposure. The composite SZ58 with a lower Zr:Sc ratio (Zr:Sc < 1) has the highest strength (HV 680–700 MPa) and the service temperature can be maintained up to 350°C. Above this temperature, the softening effect becomes dominant.

6.2.2 Evolution of precipitates

To understand the precipitation hardening response of the Sc- or (Sc+Zr)-containing composites in Figures 6.2 and 6.3, the precipitation of Al_3Sc or $\text{Al}_3(\text{Sc,Zr})$ particles of two typical composites, S58 and SZ58, were investigated via TEM. Figure 6.5 shows the representative TEM images which demonstrate the precipitate evolution of these two materials for different aging times. The sizes of precipitates as a function of aging time were measured using image analysis and the corresponding results are listed in Table 6.1.

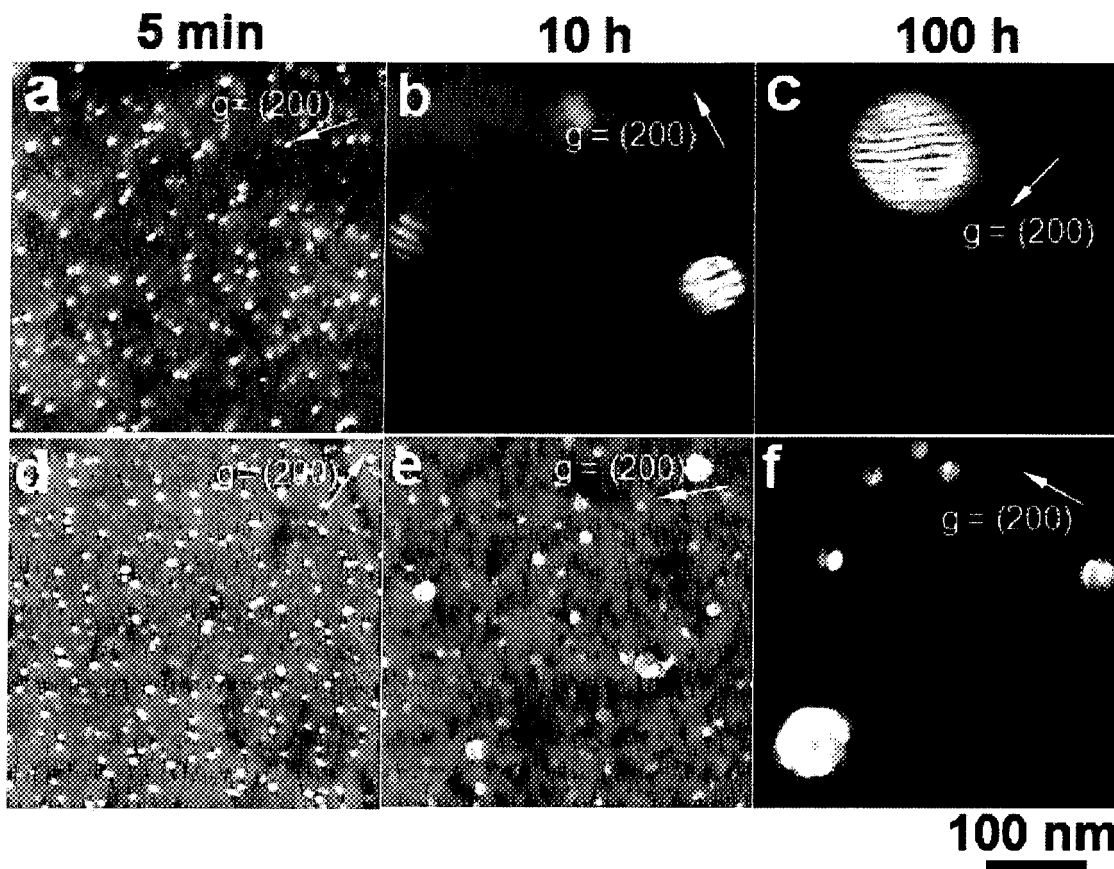


Figure 6.5 Dark-Field TEM images show the evolution of precipitates in the matrix of the composites S58 (a–c) and SZ58 (d–f) during aging at 450°C for different exposure times. All of the images are taken utilizing (100) superlattice reflections near [011] zone axis.

At early aging time (5 min., the peak aging), a uniform distribution of coherent Al_3Sc in the S58 composite, and $\text{Al}_3(\text{Sc},\text{Zr})$ in the SZ58 composite is observed. Both types of precipitates have a spheroidal morphology with the stable L1_2 structure. The Al_3Sc precipitates have an average radius of 3.5 nm while the $\text{Al}_3(\text{Sc},\text{Zr})$ precipitates show a finer size with a mean radius of 3 nm. With prolonged aging time, both types of precipitates coarsen, but with different coarsening rates. The average radius of Al_3Sc in the S58

composite increases significantly with aging time, from 3.5 nm after 5 minutes to 54.5 nm after 100 h aging, by a factor of about 15.5. On the other hand, the $\text{Al}_3(\text{Sc,Zr})$ in the SZ58 composite exhibits a better coarsening resistance. The mean radius of $\text{Al}_3(\text{Sc,Zr})$ increases from 3 nm after 5 minutes to 13.7 nm after 100h by a factor of ~4.5.

Table 6.1 Average precipitate radii of precipitates as a function of aging time at 450 °C in the composites S58 and SZ58

Aging time (h)	S58		SZ58	
	Number of precipitates	Average radius of precipitate (nm)	Number of precipitates	Average radius of precipitate (nm)
0.083(5min)	3119	3.5 ± 1.0	4304	3.0 ± 0.9
10	128	23.0 ± 6.0	651	5.6 ± 3.1
100	74	54.5 ± 13.9	232	13.7 ± 6.3

Results of EDS analysis show that only Al and Sc elements exist in the precipitates of the S58 composite while Al, Sc and Zr are detected in the precipitates of the SZ58 composite. van Dalen [129] reported that Ti has a small partition to the $\text{Al}_3(\text{Sc}_{1-x}\text{Ti}_x)$ precipitates, which might influence the coarsening resistance of the precipitates. Although the matrix of both composites may contain a small amount of solute Ti, Ti element, even at the trace level, is not detected in both types of precipitates. Thus the precipitates formed in the experimental composites are classic Al_3Sc and $\text{Al}_3(\text{Sc,Zr})$ particles without the influence of the other elements.

The values of the precipitate volume fraction, measured at peak aging (450 °C/5 min), are 0.20% and 0.33% for the composites S58 and SZ58, respectively. It is evident that the addition of Zr effectively boosts the volume fraction of precipitates and hence improves the precipitation strengthening effect. For longer aging times, the TEM image data show less number but larger size of precipitates caused by the coarsening process. Accordingly, the volume fractions were not calculated in this case, as it may lead to large statistical uncertainty.

Figure 6.6 illustrates the precipitate size distributions (PSDs) of the S58 and SZ58 composites aged at 450°C. PSDs are displayed for three aging times: 5 min, 10 h and 100 h. The PSDs for 5 min aging have a similar spread for both materials and the precipitate radii are mostly centered in the range from 2 to 5 nm. When the aging time increases to 10 h, for composite S58 not only does the average precipitate radius increase rapidly but the PSD also becomes broader, while mean precipitate radius of SZ58 still remains small and the PSD keeps within a narrow range. As the time further prolonging to 100h, the coarsening process of precipitates in the S58 accelerates and the precipitate radii spread over a wide range from 30 to 80 nm. On the contrary, the coarsening effect in the SZ58 is restrained and most precipitates exhibit a radius range of 5 to 25 nm.

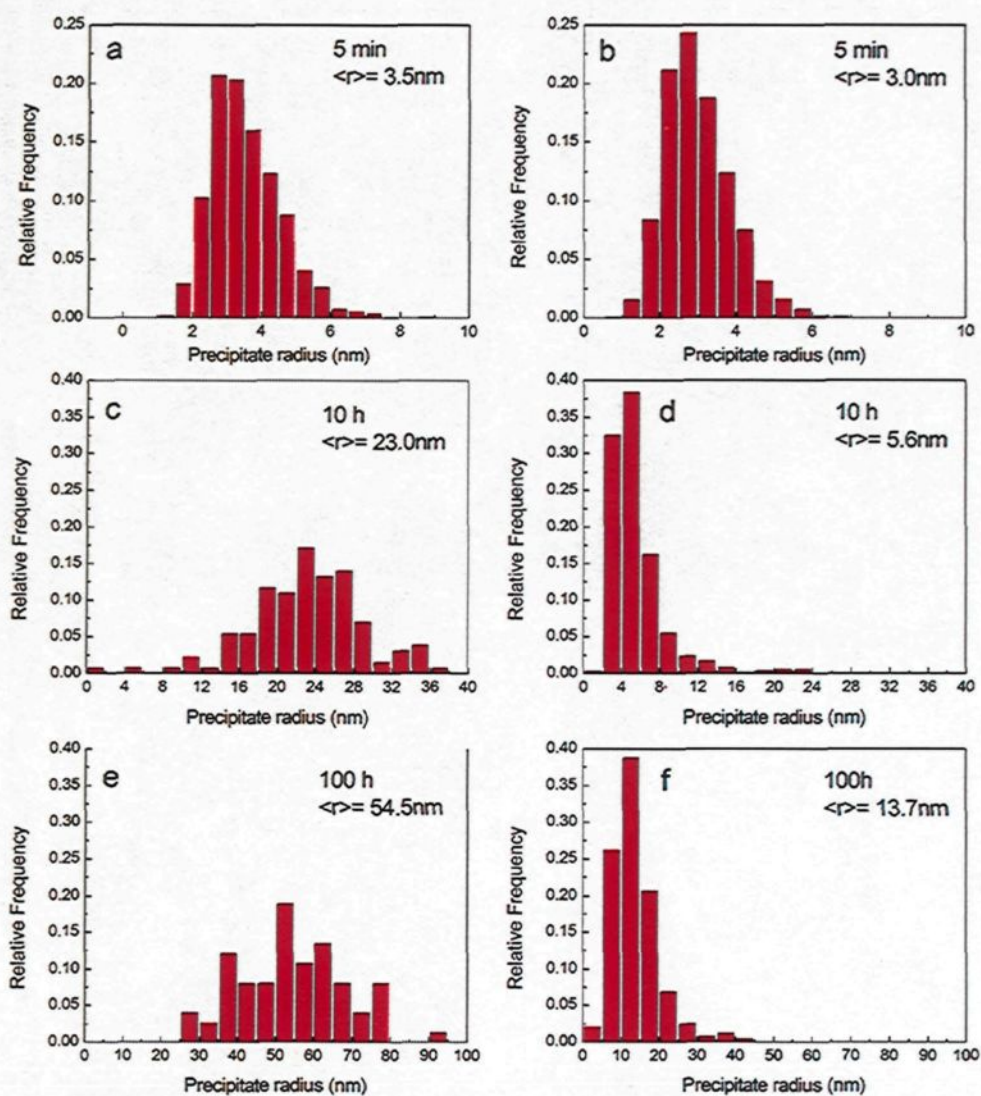


Figure 6.6 Precipitate size distributions in the composites S58 (a, c and e) and SZ58 (b, d and f) aged at 450°C for 5min, 10h and 100h.

As the large trialuminum particles grow at the expense of small particles during aging, they will sooner or later reach a critical size where the precipitates lose their coherency with the matrix materials. According to the study reported in Ref [97], when $\langle r \rangle$ is less than 15 nm, Al_3Sc type precipitates keep coherent with the matrix; when $\langle r \rangle$ lies between

15 to 40 nm, they begin to lose their coherency and become semi-coherent; while for $\langle r \rangle$ values over 40 nm, they completely lose coherency. Applied in our case, Al_3Sc precipitates formed during 450°C aging in the S58 composite undergo all stages from full coherency with the matrix (5 min), to semi-coherency at (10 h), to a complete loss of coherency (100 h). Using the same criterion, it can be seen from Figure 6.6 d and e that $\text{Al}_3(\text{Sc,Zr})$ precipitates formed in the SZ58 composite remain coherent with the Al-matrix up to 10 h of aging. After 100 h holding time, some of them begin to lose the coherency (Figure 6.6 f) and exhibit semi-coherent characteristics.

Figure 6.7 demonstrates the distribution of precipitates near the grain boundary and in the front of the interfacial area. The images were obtained from the composite S58 in the peak-aged condition (5min at 450°C). At the grain boundary, a precipitate free zone (PFZ) was observed, whose width varies from several to tens of nanometers. In the as-cast condition (see session 5.2.2.3), the PFZ width was 50–100nm at the grain boundaries. Moreover, the width of PFZ at B_4C particle interface lies around 50nm. This value is much smaller compared with that observed in the as-cast condition ($\sim 2 \mu\text{m}$). Therefore, it can be concluded that the homogenization treatment at high temperature for a sufficient period of time produces a more uniform distribution of solute atoms in the matrix and hence significantly reduces the width of the PFZs.

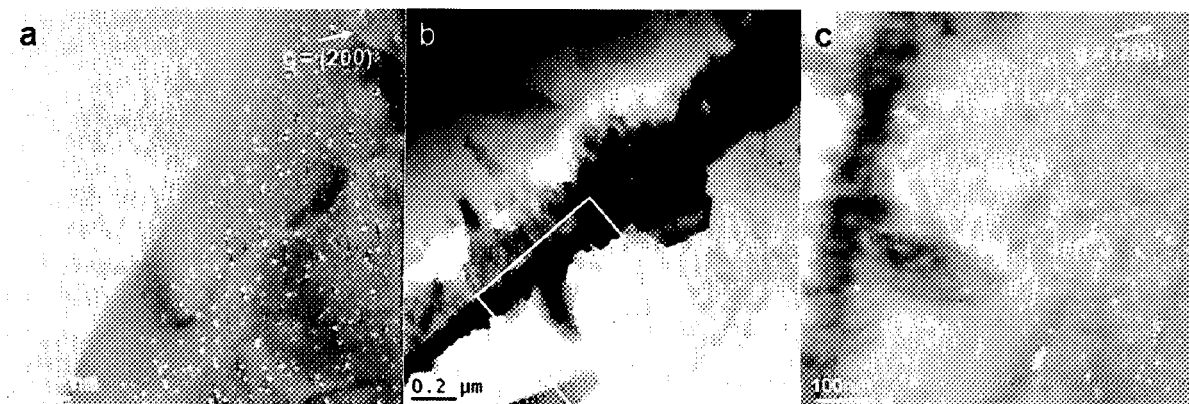


Figure 6.7 Distribution of precipitates at the grain boundary and in front of the interface in the composite S58 aged at 450 °C for 5 min: **a** Superlattice dark-field image illustrating a PFZ with variable widths at the grain boundary (using 100 reflections of precipitates near [011] axis); **b** STEM image demonstrating particle distribution in front of interface, **c** Superlattice dark-field image illustrating magnified view of precipitates distribution in the area mark by white square in **b**.

6.3 Discussion

6.3.1 Coarsening behavior of Al_3M precipitates

The coarsening data for S58 and SZ58 composites at 450 °C are displayed in Figure 6.8 by plotting the average precipitate radii $\langle r \rangle$ as a function of aging time on a double logarithmic plot. The time exponents for coarsening in the S58 and SZ58 composites are 0.38 and 0.20, respectively. In practice, the time exponent for coarsening in Al-Sc binary systems is reported around 0.33 [67, 68]. According to the classic LSW theory, a value of 0.33 is expected when the volume diffusion dominates the coarsening mechanism of precipitates [65, 66]. It should be noted that the time exponent of the S58 composite is higher than the expected value of 1/3, indicating an accelerated coarsening of Al_3Sc during the aging process. The phenomenon of accelerated coarsening of precipitates in the

composite is reported in [135, 191] probably due to the high density of dislocations produced by the addition of ceramic particulates, which favors the growth of precipitates for enhancing the diffusion of solute atoms as high-diffusion path.

Results of TEM investigation in this study indicate that the introduction of Zr has large impact on the coarsening kinetic of $\text{Al}_3(\text{Sc}, \text{Zr})$. The $\text{Al}_3(\text{Sc}, \text{Zr})$ precipitates formed in the (Sc+Zr)-containing composites are highly resistant to coarsening. The addition of Zr yields a time exponent of 0.2 for the SZ58 composite that is significantly smaller than that for the Sc-containing composite (S58), which is supported by similar observations in other (Sc+Zr)-containing aluminum alloys [72, 112]. The growth of precipitates is described as a continually collecting process of Zr atoms which enrich the outer shell of the $\text{Al}_3(\text{Sc}, \text{Zr})$ precipitates [121, 122]. The coarsening rate of the precipitates is controlled by the volume diffusion of Zr, whose diffusion coefficient in Al is close to three orders of magnitude smaller than that of Sc in Al at 450 °C ($D_{\text{Zr}} = 2.32 \times 10^{-19}$, $D_{\text{Sc}} = 1.77 \times 10^{-16}$, calculated based on the equation given in Ref. [124]). Thus the coarsening of $\text{Al}_3(\text{Sc}, \text{Zr})$ precipitates is significantly retarded [72].

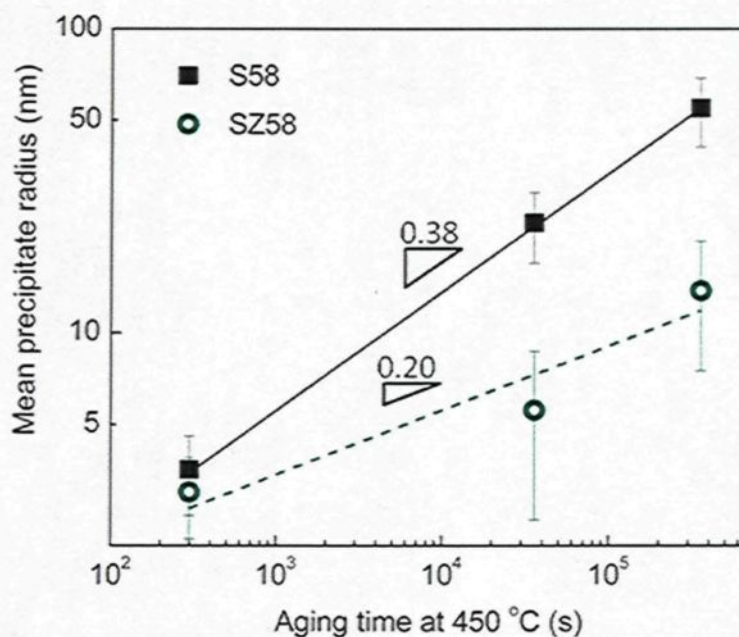


Figure 6.8 Average precipitate radii formed in two composites as a function of aging time on a double logarithmic plot at 450 °C.

6.3.2 Precipitation strengthening mechanisms

Theories of precipitation strengthening have been well studied and reviewed in Refs. [30, 31]. Precipitate shearing and precipitate bypass by dislocation looping are two main mechanisms to explain the increase of yield strength in general precipitate-strengthened alloys. In the case that the coherent precipitates are small, the strength is controlled by dislocation shearing where the dislocation can cut and move forward through precipitates. For this shearing mechanism, the increase in strength comes from the three contributions: (i) modulus hardening, (ii) coherency strengthening and (iii) order strengthening. A description of the increase in yield strength for each contribution is outlined below.

The strength increment due to modulus strengthening, $\Delta\sigma_{ms}$, arises through the mismatch between the shear modulus of the precipitate and matrix phase and is given by [52]:

$$\Delta\sigma_{ms} = M \cdot 0.0055(\Delta G)^{3/2} \left(\frac{V_p}{\frac{1}{2}G_{Al}b^2} \right)^{1/2} b \left(\frac{\langle r \rangle}{b} \right)^{3m/2-1} \quad (\text{Eq. 6.1})$$

where $M = 3.06$ is the Taylor mean orientation factor [60], G_{Al} is the shear modulus of pure Al (25.4 GPa at 24 °C [192]), ΔG is the difference in the modulus between Al and Al_3M precipitates (here, assumed Al_3Sc and $\text{Al}_3(\text{Sc}, \text{Zr})$ have the same stiffness, 68 GPa [193]), $b = 0.286$ nm, represents the magnitude of the Al Burgers vector [60], and $m = 0.85$ is a constant [52].

The elastic strain-field interactions between the coherent precipitates and the dislocations are also a source of strengthening. The strength increment resulting from coherency strengthening, $\Delta\sigma_{cs}$, is given by [52]:

$$\Delta\sigma_{cs} = M \chi (\varepsilon G_{Al})^{3/2} \left(\frac{\langle r \rangle V_p}{0.18 G_{Al} b} \right)^{1/2} \quad (\text{Eq. 6.2})$$

where $\chi = 2.6$ is a constant [52], ε is the lattice parameter misfit whose value is approximated by $\frac{2}{3}\delta$. δ is a composition-related factor of the lattice parameter mismatch between the matrix and the precipitate. In this case, it determined to be 1.32 for Al_3Sc [11]; with respect to the δ value for $\text{Al}_3(\text{Sc}, \text{Zr})$ precipitates investigated in the present work, whose value cannot be obtained directly since the exact number does not exist in the

literature. As discussed in the Chapter 5, the concentrations of Zr and Sc in composite SZ58 were estimated to be 0.2 and 0.3wt.%, respectively, yielding the atomic ratio of Zr:Sc of 4.05. Based on a series of composition-dependent lattice parameter misfit values given in Ref [23], the δ value for the $Al_3(Sc,Zr)$ is determined to be 1.22%. Modulus strengthening and coherency strengthening take place in parallel, usually their influences on the material are combined [24].

Thirdly, order strengthening occurs where antiphase boundaries (APB) are introduced when the ordered precipitates are sheared by dislocations. The strength increment due to order strengthening, $\Delta\sigma_{os}$, is given by [52]

$$\Delta\sigma_{os} = M \cdot 0.81 \frac{\gamma_{APB}}{2b} \left(\frac{3\pi V_p}{8} \right)^{1/2} \quad (\text{Eq. 6.3})$$

where $\gamma_{APB} \sim 0.5 \text{ J m}^{-2}$ is the APB energy of the precipitate phase (the average value for Al_3Sc [194-196] is taken for both precipitates).

When the precipitates grow and coarsen at a given temperature beyond a critical size, they finally become unshearable. Hence the dislocations have to bypass them leaving dislocation loops around each particle. In this condition, another precipitate bypass mechanism, i.e. Orowan dislocation looping, controls the increase of strength. The corresponding Orowan stress, $\Delta\sigma_{om}$, is given by [33]:

$$\Delta\sigma_{om} = M \frac{0.4G_{Al}b \ln(2R/b)}{\pi L_{p-p} \sqrt{1-\nu}} \quad (\text{Eq. 6.4})$$

where $\nu = 0.345$ is the Poisson's ratio for Al [60], $R = \frac{\pi}{4}\langle r \rangle$ is the mean radius of a circular crosssection in a random plane for a spherical precipitate [61], and L_{p-p} is the inter-precipitate spacing [52, 61], given by:

$$L_{p-p} = \sqrt{\frac{2\pi}{3V_p}} \cdot \langle r \rangle - 2R = \left(\sqrt{\frac{2\pi}{3V_p}} - \frac{\pi}{2} \right) \langle r \rangle \quad (\text{Eq. 6.5})$$

Utilizing Equations (6.1)–(6.5), the yield stress increment due to the presence of nano-size precipitates is calculated and Figure 6.9 displays the calculated and measured increment in yield strength as a function of mean radius of precipitates, $\langle r \rangle$, in the two composites S58 and SZ58. The measured values of the increments in microhardness yield stress were calculated by subtracting the as-homogenized hardness from the peak aged hardness and multiplying by the conversion factor of 1/3 [197]. As shown in Figure 6.9, the maximum increments of strength (~ 100 MPa) for the two materials are obtained at the lowest values of $\langle r \rangle$ (aged at 450 °C for 5 min) and decrease monotonically thereafter with the increase in $\langle r \rangle$.

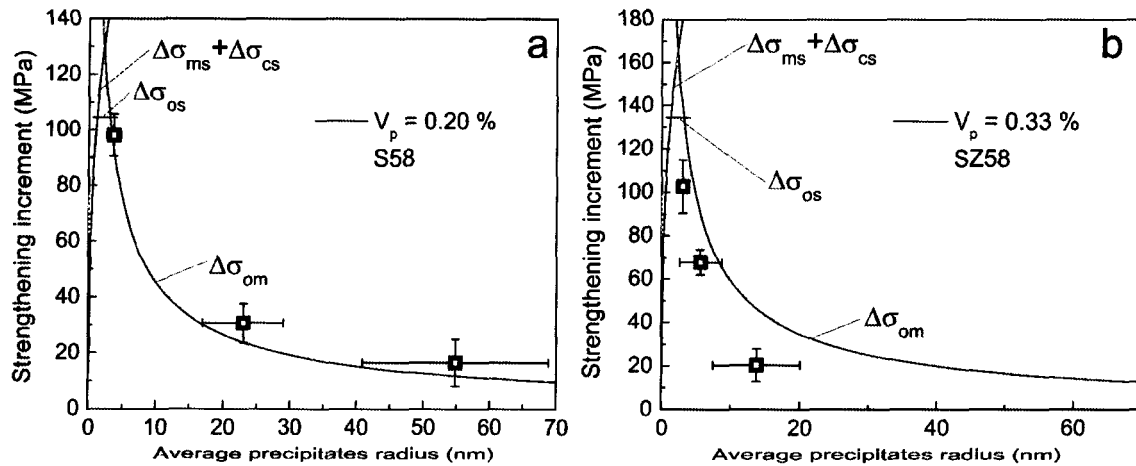


Figure 6.9 Microhardness yield stress increment as a function of the average precipitate radius $\langle r \rangle$ for the composite: **a** S58 ($V_p = 0.20\%$), and **b** SZ58 ($V_p = 0.33\%$). The lines represent the theoretical predictions of Eqs. (6.1)–(6.5) for $V_p = 0.20$ and 0.33% .

As suggested in Ref [23], the increment in strengthening due to precipitate shearing is controlled by (a) the sum of modulus and coherency strengthening ($\Delta\sigma_{ms} + \Delta\sigma_{cs}$), or (b) the order strengthening $\Delta\sigma_{os}$. Referring to the S58 composite, the strength increase is controlled by ($\Delta\sigma_{ms} + \Delta\sigma_{cs}$) when $\langle r \rangle$ is less than 1.0 nm, then by $\Delta\sigma_{os}$ during the stage when $\langle r \rangle$ is in the range of 1.0 to 3.1 nm. For the SZ58 composite, ($\Delta\sigma_{ms} + \Delta\sigma_{cs}$) is dominant for $\langle r \rangle$ less than 1.4 nm and $\Delta\sigma_{os}$ for $\langle r \rangle$ between 1.4 and 2.8 nm. Since the precipitate shearing and Orowan bypass mechanisms are in parallel, strengthening is given by the smallest values of these strengthening modes. Equations (6.1)–(6.5) and Figure 6.9 predict that the critical values between the shearing and Orowan modes are 3.1 and 2.8 nm for the S58 and SZ58 composites, respectively. Apparently, since all measurements of $\langle r \rangle$ are larger than the critical value, Orowan bypass mechanism is the main controlling mechanism for both

composites. The observations in Figure 6.9 also indicate that the experimental data in S58 are in excellent accordance with theoretical expectations, while the measurements for SZ58 exhibit fair agreement with the prediction except at the largest precipitate radius.

6.4 Summary

In this chapter, a series of Al–Sc and Al–Sc–Zr metal matrix composites with a reinforcement of 15 vol.% B₄C were isothermally aged at 300, 350, 400 and 450 °C. The effects of Sc and Zr on the aging behavior, precipitation strengthening and precipitate coarsening of these composite materials during the aging process were investigated. The results and findings are summarized as follows:

The addition of Sc to Al–B₄C composites provides a considerable precipitation hardening of the composite matrix for all aging temperatures investigated. The precipitation hardening effect increases with increasing Sc content and decreases with increase in aging temperature. The Sc-containing composites are thermally stable up to 300 °C and at higher temperatures, rapid softening of the matrix takes place.

The combined addition of Sc and Zr to Al–B₄C composites produces a remarkable synergistic effect with respect to strengthening. The addition of Zr not only provides an increase in strength at peak aging but also improves the thermal stability at all temperatures investigated.

The ratio of Zr:Sc has an important impact on the precipitation hardening and thermal stability. As the Zr:Sc ratio increases, the precipitation hardening efficiency increases and

the softening resistance improves. Al–Sc–Zr composites with a high Zr:Sc ratio (≥ 1) show excellent thermal stability up to 400°C. The overaging in such materials is delayed by ~100°C compared with the Zr-free composites containing the same level of Sc.

During aging, Al–Sc and Al–Sc–Zr composites yield two types of nano-size precipitates, Al_3Sc and $\text{Al}_3(\text{Sc},\text{Zr})$ respectively, with different coarsening rates. The Zr addition in Al–Sc–Zr composites increases the volume fraction of precipitates, which is a major contribution to the additional increase in the strength. Moreover, $\text{Al}_3(\text{Sc},\text{Zr})$ in Al–Sc–Zr composites exhibits a much better coarsening resistance than Al_3Sc in Al–Sc composites.

Orowan bypassing mechanism is the main controlling mechanism for the precipitation hardening of Al_3Sc and $\text{Al}_3(\text{Sc},\text{Zr})$ precipitates. The strengthening increment (calculated from microhardness) as a function of average precipitate radius for both precipitates at a given temperature shows a good agreement with the theoretical predictions of the Orowan model.

CHAPTER 7

THERMAL STABILITY OF MECHANICAL PROPERTIES AT ELEVATED TEMPERATURE

Chapter 7

Thermal stability of mechanical properties at elevated temperature

7.1 Introduction

It has been demonstrated that the precipitation of nano-scale Al_3Sc or $\text{Al}_3(\text{Sc}, \text{Zr})$ precipitates results in a pronounced strengthening response at all as-cast and aged conditions investigated. However, to date, there is very limited information on the long-term thermal stability of Al-based MMCs available in the open literature. In Al-based particulate reinforced composites, there are a number of factors, including the Al matrix, reinforcement particles and other structural components. Several strengthening contributions can influence the overall strength of the composite materials [198]:

- Grain boundary strengthening. It is well accepted that grain boundaries act as barriers to dislocation motion.
- Load transfer from the matrix to the reinforcement through interface. Basically the ceramic reinforcements have high stiffness and Young's modulus compared to the

metal matrix. If the load on the matrix could effectively transfer on the reinforcement through the interface, the improvement of strength is definitely expected [1, 199, 200].

- Precipitation strengthening. The strengthening resulting from the precipitates can be controlled by two mechanisms, i.e. shearing mechanism and Orowan bypass mechanism, depending on the size of the precipitates. Shearing mechanism is applied in the case of fine, coherent precipitates [31], while the Orowan dislocation mechanism is preferred for explaining the strengthening effect of larger precipitates [23, 24, 198].
- Solution strengthening. This involves a considerable amount of dissolved atoms in the Al matrix. In the case of our AA1100 matrix base composites with minor alloying additions, this strengthening mechanism has a negligible contribution.

The aim of this chapter is to study the precipitation strengthening response, thermal stability of mechanical properties and microstructure evolution of two experimental Al-B₄C composites alloyed with Sc and Zr (S40 and SZ40). A long annealing process up to 2000 hrs at the temperature range from 250 to 350°C were performed (Table 3.5). The threshold temperatures for the short-term stability (few hundreds hours) as well as the long-term stability (several thousands hours) are determined for both composites.

7.2 Results

7.2.1 Age hardening response

After homogenization at 640°C, two composites SZ40 and S40 were aged at different temperatures up to 200 hours to examine their precipitation strengthening response. Figure 7.1 shows the Vickers hardness vs. aging time curves of the two composites. In general, the aging curves exhibit the expected three regions of a classic aging response: (a) a period with a rapid increase in hardness values (underaging); (b) a plateau at high hardness values (peak aging); and (c) a decrease in the hardness with time (overaging). For both materials, the higher the aging temperature, the shorter the underaging period and the lower the peak hardness.

For the composite containing Sc (S40), aging at 300°C produces the maximum peak hardness of 58 HV which remains constant for up to 50 h. As the aging time is increased further, a slight softening within 10% reduction from the peak value is noticeable. At higher aging temperatures, there is a continuous decrease in hardness after reaching the peak value, which suggests that the Al₃Sc precipitates are coarsening with time, and leading to overaging. At such high temperatures, the strengthening effect is virtually lost after 100 to 200 h exposure.

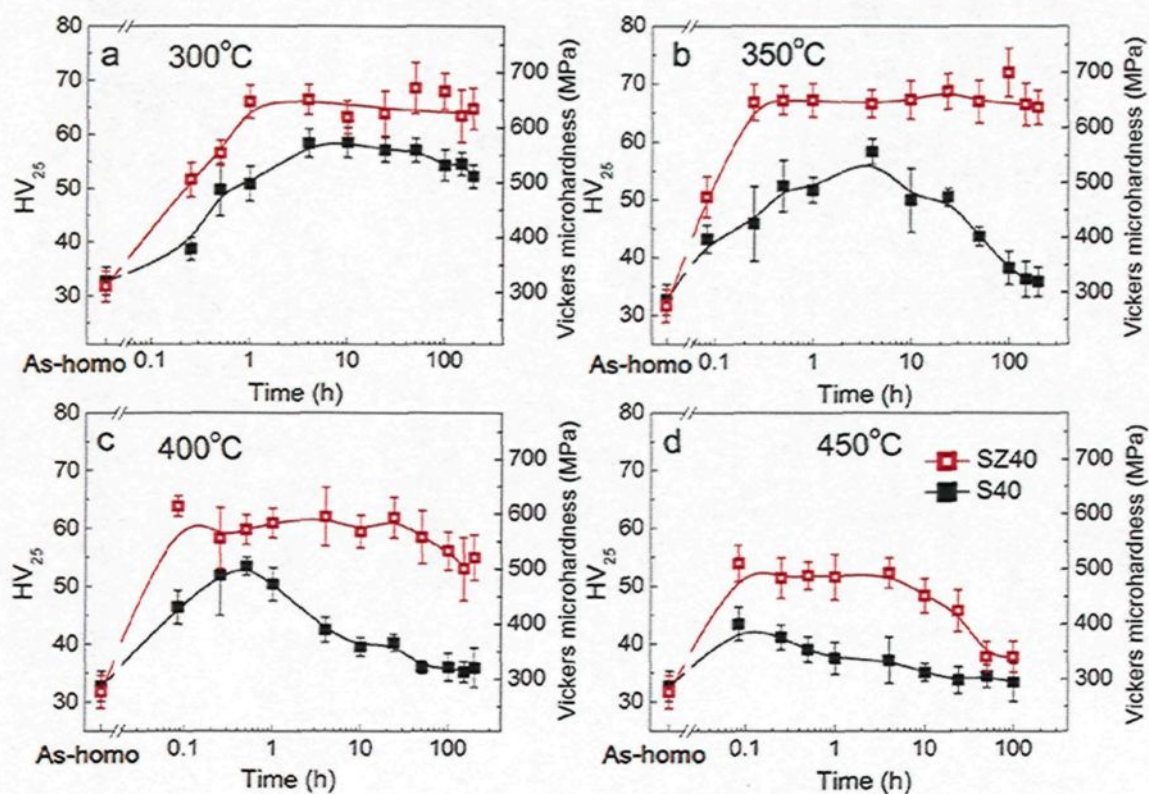


Figure 7.1 Vickers hardness vs. aging time at: **a** 300 °C, **b** 350 °C, **c** 400 °C and **d** 450 °C for composites SZ40 and S40.

The peak hardness of the composite containing both Sc and Zr (SZ40) is substantially higher than the composite containing only Sc (S40) at all temperatures investigated. Upon aging at 300 and 350°C, it reaches the maximum peak hardness of 67 HV and a plateau of the peak aging remains constant up to 200 h. As the aging temperature increases to 400°C, the composite SZ40 has a plateau of the peak aging up to 50 h and exhibits only a slight overaging from 50 to 200 h, which indicates that $\text{Al}_3(\text{Sc,Zr})$ precipitates are coarsening resistant up to 400°C for a short-term exposure. The aging curve of SZ40 at 400°C is very similar to the aging curve of S40 at 300°C, which demonstrates that the Zr addition delays

the overaging by $\sim 100^\circ\text{C}$. It means, in the practical term, that it raises the maximum service temperature of the composite material by $\sim 100^\circ\text{C}$. It is interesting to note that even at 450°C where the overaging occurs, there is still a perceptible strengthening effect up to 10 h for the composite SZ40, which provides a safety margin for the material when used at high temperature.

Compared with the composite containing only Sc (S40), the composite containing both Sc and Zr (SZ40) displays remarkably higher peak hardness and for longer durations at all temperatures (Figure 7.1). Results clearly show that the addition of Zr to the Sc-containing composite enhances the strengthening effect and increases the overaging resistance at elevated temperatures. In prior studies by the authors, it has been demonstrated that at the same Sc levels, Zr additions increase remarkably the volume fraction of the dispersed precipitates in both as-cast and aged conditions, and thus improve the overall strength of the material. On the other hand, it is reported by several researchers [118, 131, 201] that the addition of slow diffusing element Zr, which is soluble in Al_3Sc to form coherent $\text{Al}_3(\text{Sc,Zr})$, increases the coarsening resistance of the dispersed precipitates and thus improve the resistance to overaging of the material at high temperature.

As mentioned before, in Al- B_4C composites some of the Sc and Zr will react with B_4C and will be consumed at the interfaces. Therefore, the accurate amount of Sc and Zr retained in the matrix for the precipitation strengthening is unknown. Comparing the achievable peak microhardness at 300°C with that reported for binary Al-Sc alloy, it is estimated that approximately 0.2 wt.% Sc remains in the Al matrix of both composites. The

amount of Zr that is soluble in the Al matrix of the composite SZ40 may lie in the range of 0.15–0.20 wt.%.

It should be mentioned that although the two composites S40 and SZ40 contained 1.5 wt.% Ti, the Ti did not have any impact on the precipitation strengthening. During the liquid stage of fabricating Al-B₄C composites, it was necessary to add Ti in order to prevent B₄C degradation and increase the castability [5]. Almost all Ti was located at the interfaces between aluminum and B₄C particles in the form of a dense and protective TiB₂ layer [25, 26].

7.2.2 Long time annealing

7.2.2.1 Hardness

After the peak aging to generate the maximum precipitation strength in the matrix, the composites SZ40 and S40 were annealed at different temperatures to assess the thermal stability of the mechanical properties for long holding times. Figure 7.2 displays plots of the Vickers hardness and Rockwell hardness as a function of annealing time at different temperatures for the two composites. The initial value in Figure 7.2 is the hardness value in the peak aging condition. It is interesting to notice that when annealing at 300°C, the hardness of the composite SZ40 matrix slightly increases from the initial value during the first 200 h and then maintains a long plateau for the remaining annealing period. In the case of holding at 350 °C, a slow softening process in the composite SZ40 matrix becomes obvious after annealing for 500 h. The hardness value decreases from 60 HV at 200 h to 46 HV after 2000 h. The composite S40 exhibits a good softening resistance at 250°C, i.e.

after 2000 h holding, the material displays identical properties as in the initial peak aging condition (Figure 7.2 b). However, as the annealing temperature increases to 300°C, the hardness decreases remarkably in the first 500 h holding period. After 500 h, the slow softening becomes dominant. The value of the hardness declines from 55 HV at 200 h to 40 HV after 2000 h.

The Rockwell hardness of both composites exhibits a similar tendency as that of Vickers hardness during the annealing period. The Vickers microhardness reveals the hardening effect of the aluminum matrix of the composites while the Rockwell macrohardness displays the overall strength of the composite material. The same trend of both hardness types indicates that the change in mechanical properties of the aluminum matrix controls the softening resistance of the composite materials during the annealing.

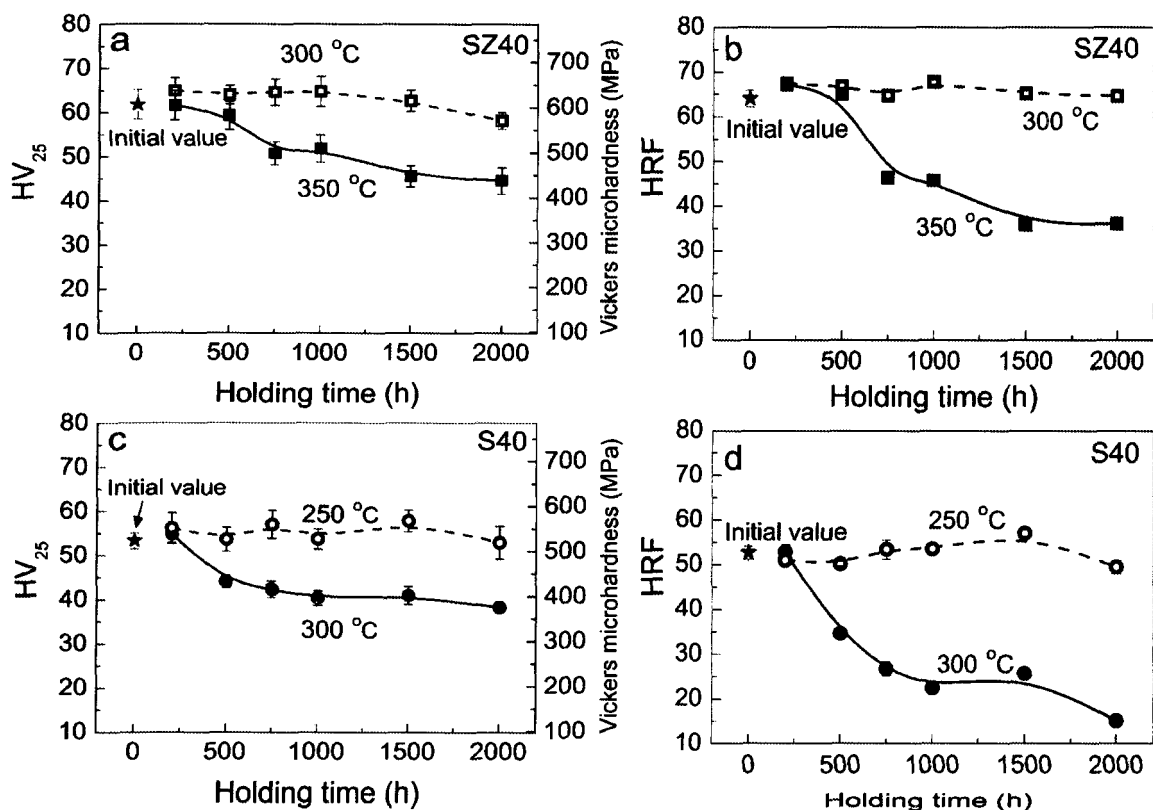


Figure 7.2 Hardness vs. annealing time. Vickers hardness: a composite SZ40 and c composite S40; Rockwell hardness: b SZ40 and d S40. The initial values of both SZ40 and S40 are from the peak aging at 350 and 300°C for 10h, respectively.

7.2.2.2 Yield and compressive strengths

The typical true stress-strain curves of the composites obtained from the compression tests on different conditions, as an example of SZ40, are shown in Figure 7.3. Based on the true stress-strain curve, the 0.2% offset yield strength and the compressive strength at true strain of 0.3 are determined.

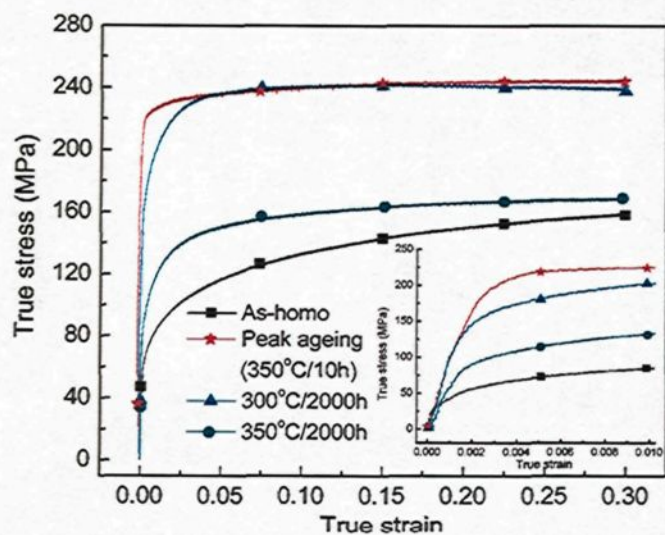


Figure 7.3 True stress–strain curves of SZ40 from compression tests in different conditions.

Figure 7.4 demonstrates the evolution of the mechanical properties of the two composites during long-term annealing at different temperatures. As reference points, Figure 7.4 also gives the initial and as-homogenized values, which are the yield and compressive strengths of the materials on the peak aging and as-homogenization conditions. Generally, the tendency of the variation of the compressive strength with annealing time is similar to that of the yield strength for the two composites (Figure 7.4), where the values of compressive strength are approximately 70 to 80 MPa higher than those of the yield strengths.

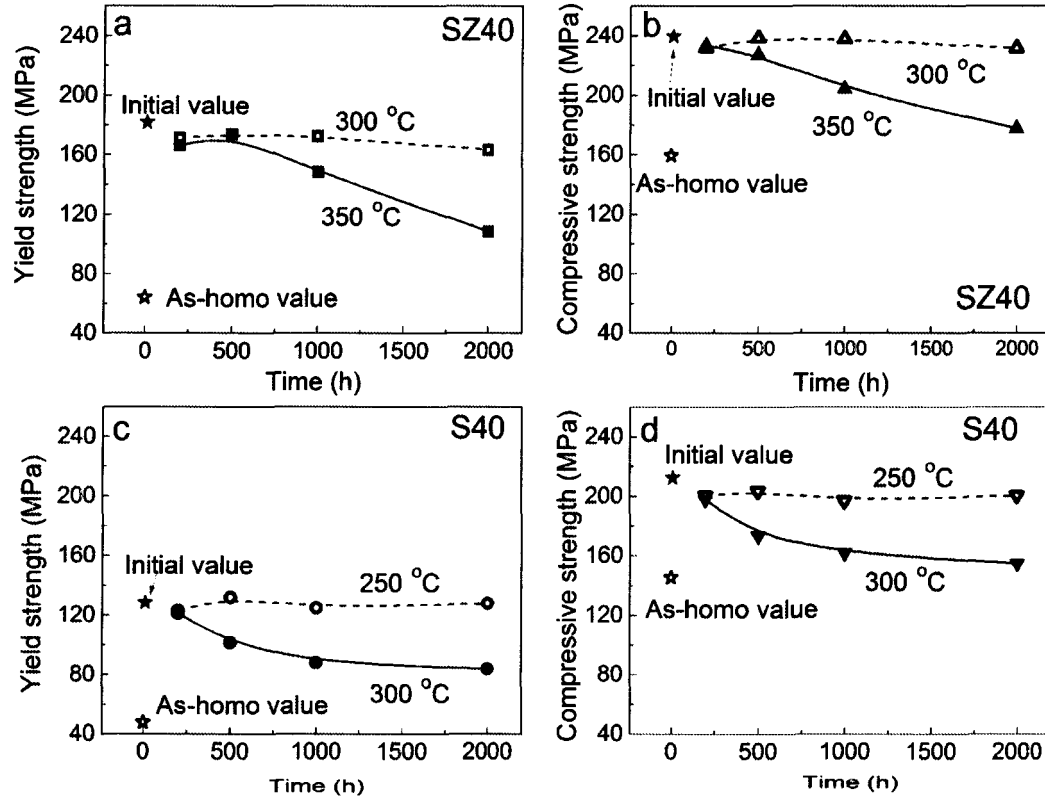


Figure 7.4 Yield and compressive strengths vs. annealing time, **a** yield strength of SZ40, **b** compressive strength of SZ40, **c** yield strength of S40, **d** compressive strength of S40.

Moreover, the yield and compressive strengths of the composites in the peak aging condition are significantly higher than those of the as-homogenized condition, attributing to the precipitation strengthening of Al_3Sc or $\text{Al}_3(\text{Sc}, \text{Zr})$ after aging. In addition, the effect of the precipitation strengthening of the composite with Zr (SZ40) is stronger than that without Zr (S40) due to the increase in volume fraction of the dispersed precipitate phase [118]. In general, both materials maintain the mechanical properties stable in the lower exposure temperatures (300°C for SZ40 and 250°C for S40), while the strengths decrease with extending the holding time at higher temperatures (350°C for SZ40 and 300°C for

S40). For example, the yield and compressive strengths of the composite SZ40 at 350°C display a clear decrease after 500 h. The yield strength falls from 164 MPa at the beginning of the holding to 108 MPa after 2000 h exposure, which represents a drop of ~34% in the initial value. It suggests that the $\text{Al}_3(\text{Sc,Zr})$ precipitates are slowly coarsening during long holding periods at higher temperature (350°C), which weakens the precipitation strengthening effect. Nevertheless, the composite containing both Sc and Zr (SZ40) still retains considerable strength after 2000 h at 350°C and is still stronger than any other conventional precipitation strengthened Al alloy for similar condition known to the authors. For the composite S40, the yield strength decreases from 128 MPa at the beginning to 84 MPa after 2000 h exposure at 300°C, which accounts for an approximate loss of 34% in the mechanical properties. It results from the progressively coarsening of Al_3Sc precipitates during long holding periods at higher temperature (300°C).

In brief, for long-term service at elevated temperatures (several thousands of hours), the mechanical properties of the composite SZ40 are stable up to 300°C, while the composite S40 exhibits a good softening resistance up to 250°C. Combined with the results in Figure 7.1, it is reasonable to consider that the threshold for short-term stability (within few hundreds of hours) of the composite SZ40 lies in ~400°C, whilst the threshold value of the composite S40 is limited to ~300°C due to the less softening resistance.

It is evident that the addition of Zr in the Sc-containing composite (SZ40) is shown to significantly retard the softening effect. It has been reported by other researchers [118, 121, 131] that Zr substitutes for Sc in Al_3Sc precipitates to form $\text{Al}_3(\text{Sc,Zr})$ precipitates which

are composed of an Al_3Sc core and a Zr-enriched shell. This shell acts as a barrier to Sc diffusion because the diffusion rate of Zr in aluminum is much lower than that of Sc. For example, the diffusivity of Zr in Al is over four orders of magnitude smaller than that of Sc in Al at 300°C : $D_{\text{Zr}} = 6.10 \times 10^{-24} \text{ m}^2/\text{s}$ and $D_{\text{Sc}} = 9.58 \times 10^{-20} \text{ m}^2/\text{s}$ [124]. Zirconium is thus very effective in stabilizing the precipitates, and therefore, improves both short- and long-term thermal stabilities of the material at elevated temperatures.

7.2.3 Microstructural analysis

The analysis focuses on the aluminum grain structure, the interfaces between B_4C particles and aluminum as well as the precipitates (size and distribution), which could have an impact on the stability of the mechanical properties.

7.2.3.1 Grain structure

Due to the presence of a large quantity of B_4C particles, it is often difficult to clearly reveal the grain structure of the aluminum matrix in an Al-based MMC by conventional optical metallography. Therefore, the electron backscatter diffraction technique (EBSD) was applied to reveal the grain morphology and size in the Al- B_4C composites. The grain structures of the SZ40 composite without annealing (only peak-aged) and after 2000 h annealing at 350°C , as an example, are shown in Figure 7.5. The black regions in the figure are the B_4C particles and the other colors represent the different orientation of grains. It is obvious that the grains in both conditions are equiaxed. The average grain sizes measured without annealing and after 2000 h annealing are 43 and 51 μm , respectively (Table 7.1). It is apparent that a slight grain coarsening occurs after a long period of annealing at 350°C .

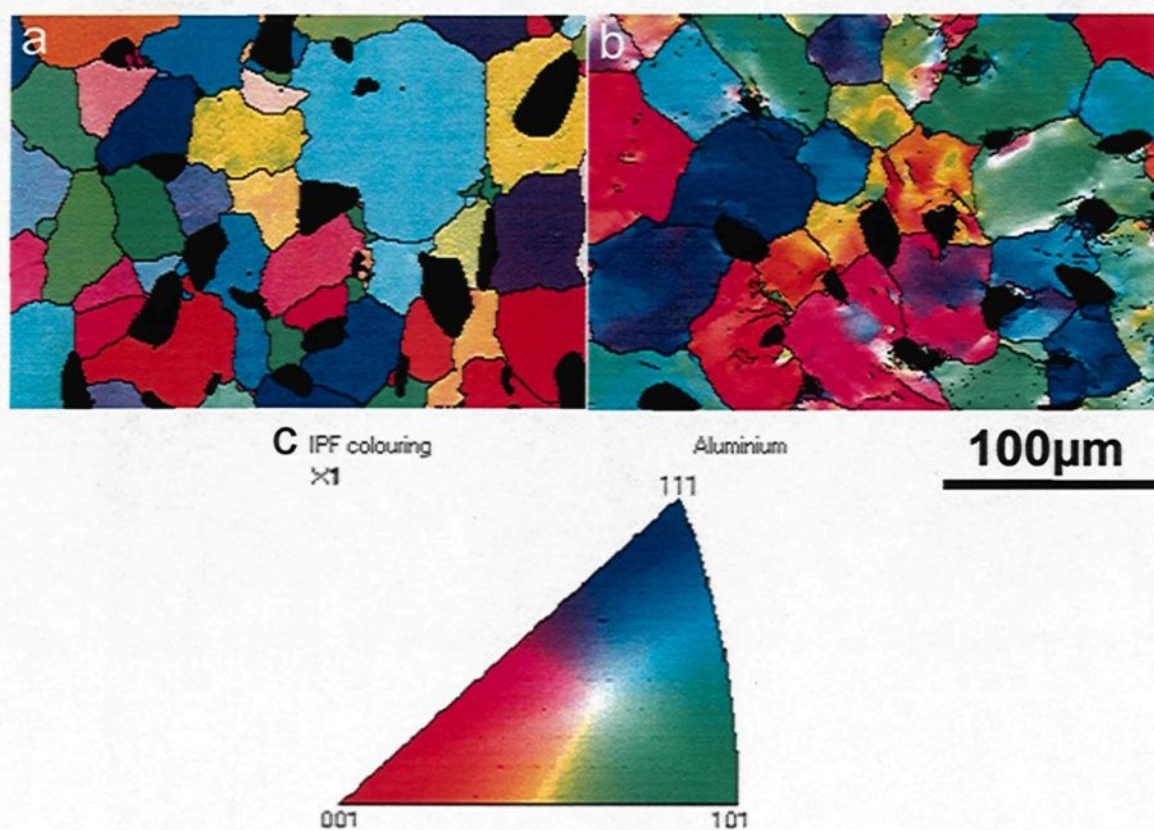


Figure 7.5 EBSD micrograph of SZ40 composite after: **a** aging at 350°C for 10 h, **b** annealing at 350°C for 2000 h.

Table 7.1 Grain size of SZ40 in different conditions

Annealing condition	Grain size (μm)
Peak aging (350°C for 10 h)	43 ± 17
Annealing at 350 °C for 2000 h	51 ± 20

7.2.3.2 Interfaces

Figure 7.6 presents optical micrographs of the two composites SZ40 and S40 in different conditions. The B_4C particles are uniformly distributed in the matrix. Some

reaction products (mainly TiB_2) are found to be attached to or surrounding the B_4C particles. The straight interfaces between the ceramic particles and the matrix indicate that no serious interfacial reactions are detectable after 2000 h holding at both temperatures of 300 and 350°C.

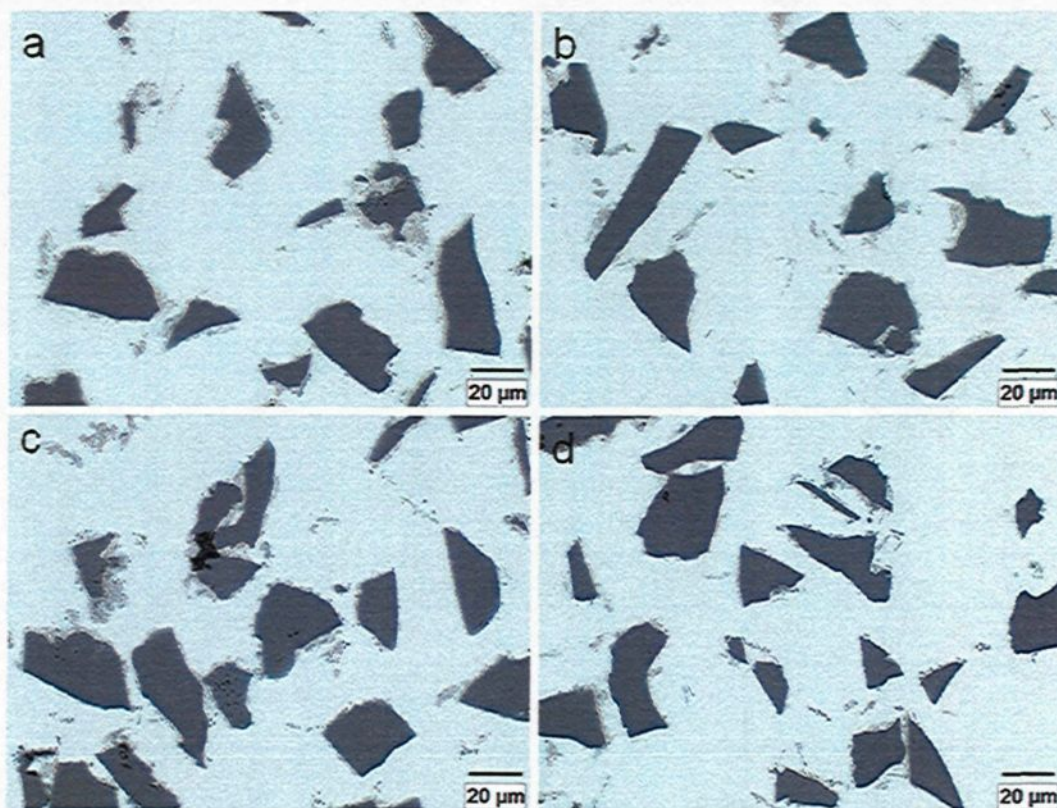


Figure 7.6 Optical micrographs of **a** S40 peak aging, **b** SZ40 peak aging, **c** S40 annealing at 300 °C for 2000 h, and **d** SZ40 annealing at 350 °C for 2000 h.

Detailed information on the interfaces and B_4C particles observed by SEM is presented in Figure 7.7. The surface of B_4C is completely enclosed with a protective layer that consisted of some reaction-induced phases, such as TiB_2 and Al_3BC . Compared with

the micrographs without annealing (Figure 7.7 a and b), it is found that the morphologies of the interfaces and B_4C particles remain unchanged after 2000 h at both temperatures of 300 and 350 °C. No obviously zig-zagged interfaces are observed, which further proves that no severe interfacial reactions and hence no serious degradation of B_4C took place during long annealing period.

7.2.3.3 Precipitate coarsening

To understand the softening resistance of these composites for extended long-term usage at elevated temperatures, specimens of the composite SZ40 annealed at the highest temperature (350°C) were examined by TEM. Figure 7.8 a shows the TEM dark-field microimage of the composite SZ40 in the peak-aged condition. Fine $Al_3(Sc,Zr)$ precipitates with an average radius of 2.6 nm are generated after aging, and those particles are uniformly distributed in high density in the aluminum matrix. Most of the precipitates have a spheroidal shape and few of them are needle-like (Figure 7-8 a). After 2000 h annealing at 350°C, the coarsening of the dispersed precipitates is obvious. The average radius of the precipitates increases to 5.1 nm and a few particles even grow up to 40 nm in size (Figure 7-8 b). The particle size distributions (PSD) of $Al_3(Sc,Zr)$ precipitates at peak aging and after 2000h annealing, are presented in Figure 7.9. After peak aging, the percentage of precipitates whose radii are in the range of 1~4 nm is approximate 96% of overall precipitates, however, the ratio of fine precipitates in the same population reduces to 55% after 2000h annealing. It indicates that the precipitates are slowly but progressively coarsening during long-term annealing and some of the precipitates grow faster than the others (Figure 7.8 and 7.9).

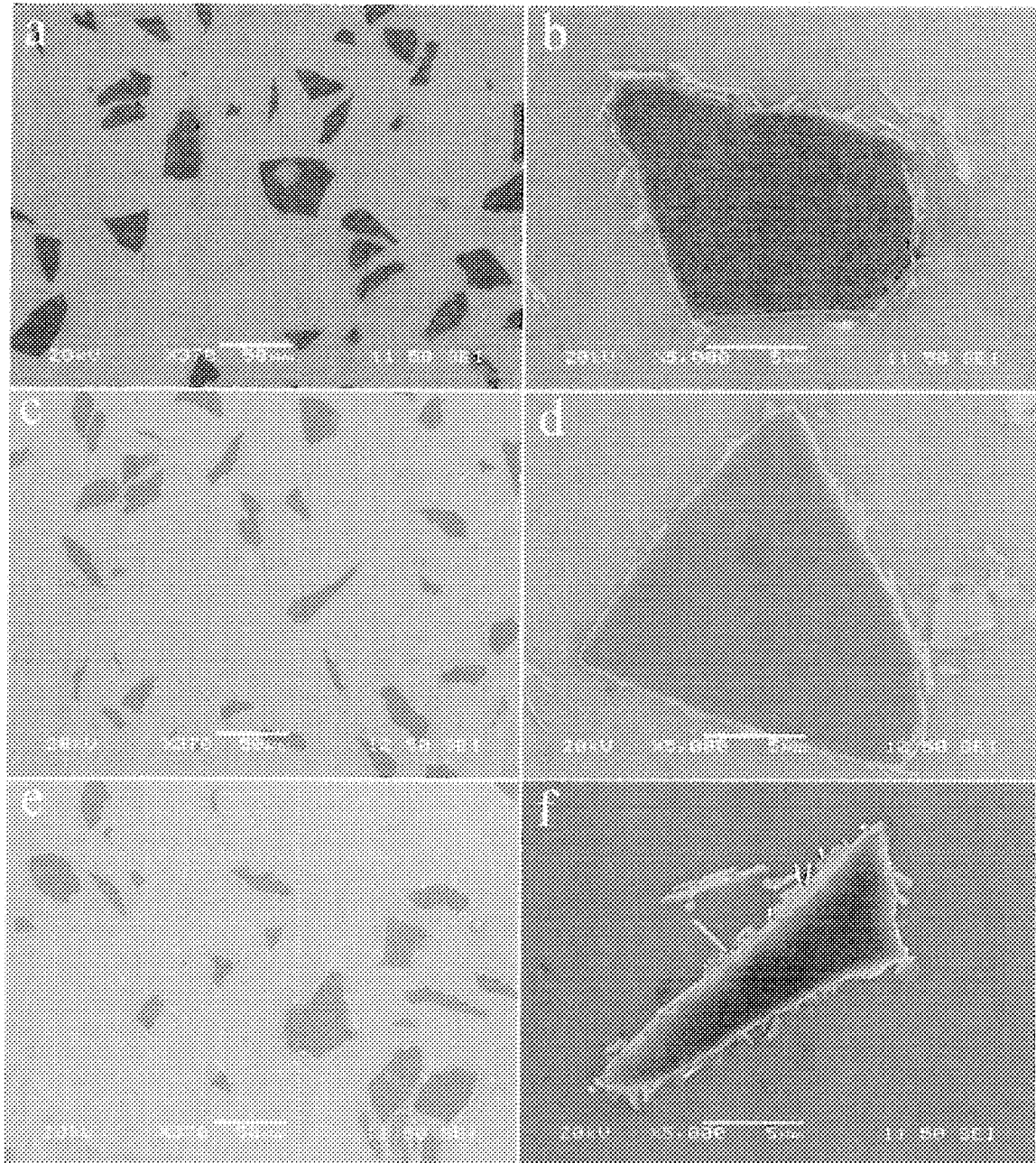


Figure 7.7 SEM micrographs of composite SZ40 revealing the morphologies of the interfaces and B₄C particles in the condition of: **a** and **b** peak aging; **c** and **d** annealing at 300°C for 2000h; **e** and **f** annealing at 350°C for 2000 h.

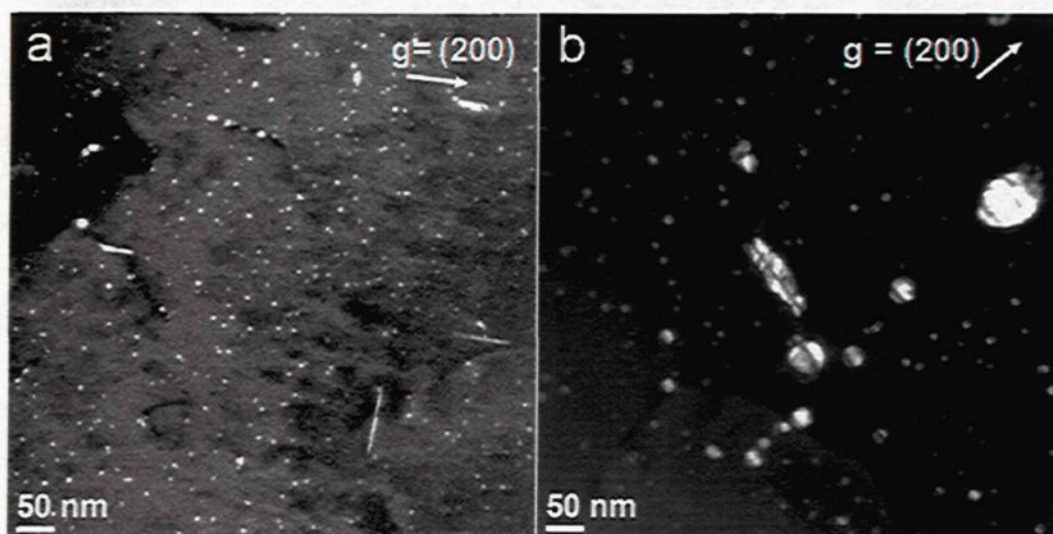


Figure 7.8 TEM dark-field images showing the precipitates in composite SZ40: **a** upon peak aging, and **b** after 2000 h annealing at 350°C.

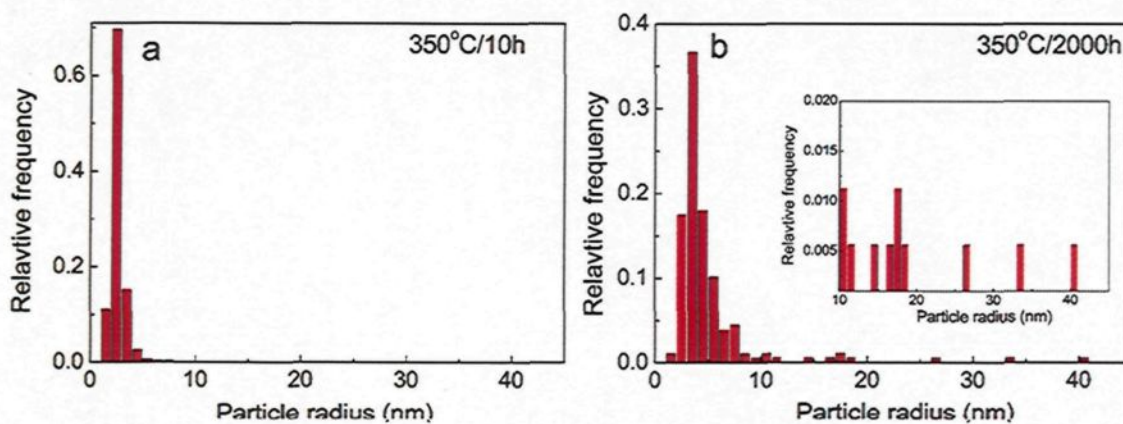


Figure 7.9 Particle size distributions of $\text{Al}_3(\text{Sc,Zr})$ precipitates in composite SZ40: **a** after peak aging, and **b** after 2000 h annealing at 350°C. The inset in **b** shows an enlargement of the PSD in the particle radius range of 10 to 45 nm.

7.3 Discussion

7.3.1 Effect of the grain size on mechanical properties

It is observed that the grain size become slightly larger after long time annealing at 350°C for 2000 h (Table 7.1). For polycrystalline materials, it is well known that grain boundaries act as an obstacle to dislocation movement and hence strengthen the material. In general, the increment in yield strength related to the change of grain size can be described by the Hall-Petch equation:

$$\Delta\sigma_{PH} = k_{PH}d^{-1/2} \quad (\text{Eq. 7.1})$$

where, d is the average grain size of material, and k_{PH} is a constant related to the specific alloy and the range in grain size [202, 203].

Equation 7.1 was applied to evaluate the contribution of the grain size to the yield strength of the composites. Here, the value of the constant k_{PH} , used for the calculation is 25 MPa $\mu\text{m}^{-1/2}$, which is appropriate for pure aluminum with a grain size range between 15 to 240 μm [204]. The results of the calculated $\Delta\sigma_{PH}$ of composite SZ40 are shown in Table 7.2.

Table 7.2 Increment of yield stress caused by grain size

Annealing condition	Grain size (μm)	Increment of yield strength $\Delta\sigma_{PH}$ (MPa)
Peak aging (350°C for 10 h)	43	3.8
Annealing at 350 °C for 2000 h	51	3.5

According to the calculation, the difference grain size results in a difference of less than 1 MPa in the yield stress. Therefore, the effect of a slight grain coarsening on the yield strength during long term annealing is negligible.

7.3.2 Effect of the interfaces on mechanical properties

The presence of a large quantity of B_4C particles in the Al matrix can also increase the strength of the composite, due to the ceramic reinforcement B_4C having a much higher stiffness and Young's modulus than the matrix. The mechanical properties of commercial purity aluminum (AA1100) and Al-15% B_4C composites at ambient temperature are listed in Table 7.3. Comparing an unalloyed Al-15% B_4C composite with AA1100 alloy, it is found that the contribution of the 15% B_4C particles to the yield strength is approximate 20 MPa. This contribution is related to the load transfer from the weaker matrix to the ceramic reinforcement particles via the interfaces [41, 43]. Therefore, the stability of the interfaces and B_4C particles play a role in the thermal stability of the mechanical properties of composites during long term annealing. Based on the microstructure observations (Figure 7.6 and 7.7) , the interfaces between B_4C particles and the Al matrix remain unchanged during 2000 h annealing at 300 to 350°C, and no serious degradation of B_4C takes place during the annealing. Theoretically, B_4C particles are not thermodynamically stable in the aluminum matrix. However, at such low temperatures (below 500°C), the decomposition of B_4C in solid aluminum through a dense protective layer in the interface is practically difficult [28, 152]. Therefore, the contribution of B_4C particles on the material strengthening is independent of the annealing temperature and time. The B_4C particles and

their interfaces in the composites have no effect on the variation of mechanical properties during long time annealing.

Table 7.3 Mechanical properties of aluminum and Al-B₄C composites at ambient temperature.

Matrix material	Heat-treatment condition		Yield strength (MPa)	Ref
	Condition	Parameters		
AA1100	Full-annealed	–	35	[176]
AA1100+15 vol.%B ₄ C	Full-annealed	–	55	[176]
SZ40	Peak aging	350°C, 10h	182	This work
	Annealing	300°C, 2000h	164	
	Annealing	350°C, 2000h	108	
S40	Peak aging	300°C, 10h	128	
	Annealing	250°C, 2000h	128	
	Annealing	300°C, 2000h	84	

7.3.3 Effect of precipitate coarsening on mechanical properties

The nano-size precipitates, Al₃Sc or Al₃(Sc,Zr), are generated in the composite S40 and SZ40 through the aging process (Figure 7.8). These precipitates significantly improve the mechanical properties of the composites (Table 7.3). The precipitation-strengthening is based on the phenomenon that precipitates act as obstacles to retard the motion of dislocations. The precipitates may either be cut by dislocations (precipitate shearing mechanism) or they are hard and large enough to resist shearing so that the dislocation can only precipitate bypass them [31, 52]. Except other strengthening mechanisms (grain-,

particle-, solid solution strengthening), precipitate shearing or Orowan looping mechanism can generally explain the ambient temperature strength in precipitate-strengthened materials [22]. In addition, it is well established that the volume fraction and dimensions of precipitates greatly influence the precipitation-strengthening effect in the material [205]. As mentioned above, the aluminum grain size, the B_4C particles and their interfaces have no remarkable effect on the variation of mechanical properties during annealing. However, at higher temperatures (300°C for S40 and 350°C for SZ40), the mechanical properties of the composites decrease considerably with extended annealing times (Figure 7.4 and Table 7.3). Figure 7.8 and 7.9 indicate that this softening effect is directly related to the precipitate coarsening which occurs during long term annealing.

Precipitate shearing is the main strengthening mechanism when the mean radius of precipitates is less than 2.8 nm in the composite Al- B_4C containing Sc and Zr, while Orowan bypass process is the operating mechanism when the mean size is larger than the critical value of 2.8 nm as was shown in Chapter 6. After the peak aging the mean radius of precipitates is 2.6 nm in SZ40 (Fig. 7.8a), and the strength of the material is controlled by shearing mechanism. However, as precipitate coarsening occurs at higher temperature, i.e., at 350°C for SZ40 composite (Figure 7.8 and 7.9), the mean radius of the precipitates is increased to 5.1 nm after 2000h annealing. Some of the precipitates even reached over 40 nm in diameter. In this condition, Orowan looping is the main operating mechanism. It is widely accepted that the strengthening effect decreases monotonically with increasing mean radius of precipitates under the Orowan looping mechanism [19, 23, 24], which results in the observed decrease of mechanical properties. Moreover, it is well known that the higher

the annealing temperature, the faster the precipitate coarsening, due to the faster diffusion of all elements in the matrix at the higher temperature. Thus, the thermal stability of the mechanical properties of the composites decreases with increase in annealing temperature.

7.4 Summary

Alloying with Sc or Sc and Zr displays a significant precipitation hardening in Al-15vol.% B₄C composites. Upon aging at 300°C, the composite containing Sc (S40) reaches a peak hardness of 58 HV. The composite containing both Sc and Zr (SZ40) produces a peak hardness of 67 HV at 300 to 350°C. Zr addition to the Sc-containing composite delays the overaging by ~100°C compared with the composite containing only Sc (S40).

The threshold for short-term stability (within few hundreds hours) of the composite containing Sc and Zr (SZ40) lies at ~400°C, while the value of the threshold of the composite containing Sc (S40) is limited to ~300°C due to lower softening resistance of the latter.

For long-term thermal stability (several thousands hours), the mechanical properties of the composite SZ40 are stable up to 300°C, while the composite S40 exhibits a good softening resistance up to 250°C. At higher temperatures (350°C for SZ40 and 300°C for S40) the strengths of the composites decrease with prolonged holding time. Nevertheless, both composites still retain reasonable strength after 2000 h annealing at higher temperatures.

The addition of Zr enhances the strengthening effect and the mechanical properties of the composite SZ40 containing Sc and Zr are higher than those of the composite S40 containing only Sc at all temperatures investigated.

The aluminum grain size, the B₄C particles, and their interfaces have no remarkable effect on the variation of mechanical properties of the composites during annealing. The reduction in the mechanical properties of the composites during long term annealing at higher temperatures is dominated by precipitate coarsening.

CHAPTER 8

HOT ROLLING OF SC AND ZR CONTAINING

COMPOSITES AND THE POST-ROLLING

HEAT TREATMENT

Chapter 8

Hot rolling of Sc and Zr containing composites and the post-rolling heat treatment

8.1 Introduction

As a neutron shielding material, Al-B₄C composites are used to fabricate the inside baskets of the transport and storage casks for the spent nuclear fuels. For this purpose, the cast ingots or billets are usually subjected to secondary transformation operations such as forging, extrusion and rolling to obtain the proper shape, size and mechanical properties. Moreover, these hot deformation techniques tend to favor the mechanical properties of composites in terms of homogenizing the reinforcement distribution, declustering agglomerates, eliminating porosity, and yielding a fine matrix grain structure [37, 206, 207]. However, the processability of hot deformation of Sc- and Zr-containing Al-B₄C composites and their impact on mechanical properties are not clear yet. In this chapter, the mechanical properties, the microstructure and the post-rolling heat treatment of two composites (S58 and SZ58) after hot rolling were examined in this study.

8.2 Results

8.2.1 The hot rolling processability of composites

The cast ingots of two composites, S58 and SZ58, with dimensions of $28 \times 40 \times 80$ mm were hot-rolled. The thickness of the cast ingot was reduced from the original 30 mm to a final thickness of 2 mm with a total deformation of 93% (see 3.5). Both materials possessed a good processability of hot rolling in the temperature range of 400 to 500°C. Only very light edge cracks occurred in the intermediate rolling plates during multi-rolling passes. The final 2 mm rolling sheets were produced with good surface quality. No major defects such as cracks, porosity, or deep scratches were found in the final rolling sheets (Fig. 3.4).

8.2.2 Microhardness of hot-rolled composites

To evaluate the influence of hot rolling on mechanical properties, the Vickers hardness of the cast ingot prior to rolling and of the final rolled sheet were measured. The details of the hot rolling procedure of both composites are listed in Appendix B. The results show that the microhardness of the as-rolled sheets of S58 and SZ58 are HV 32 and HV 36, respectively. On the other hand, the microhardness of the cast ingots of both composites (S58 and SZ58) prior to rolling (homogenized) are HV 30 and HV 34, respectively. It is evident that there is no remarkable difference in the microhardness before and after rolling.

8.2.3 Influence of the post-rolling heat treatment on the microhardness of hot-rolled composites

Post-rolling heat treatments were performed on the final rolled sheets in order to increase the mechanical properties. In the post-rolling heat treatment, the similar homogenization and aging treatments as those used for the as-cast composites (Table 8.1) were applied to the rolled sheets (SZ58 and S58). After the homogenization treatment, a slight enhancement of hardness was found for both materials, which might result from the thermal residual stress owing to the mismatch of thermal expansion coefficient between the matrix metal and ceramic reinforcements, and the solid solution strengthening (Figure 8.1).

Table 8.1 Parameters of the heat treatment

Composite	Final rolled sheets		As-cast composites	
	Homogenization	Aging	Homogenization	Aging
S58	640°C/24h (Quenched into water)	300°C for 1 to 100h	635°C/24h	300°C for 1 to 100h
SZ58	640°C/24h (Quenched into water)	300°C for 1 to 100h	640°C/96h	300°C for 1 to 100h

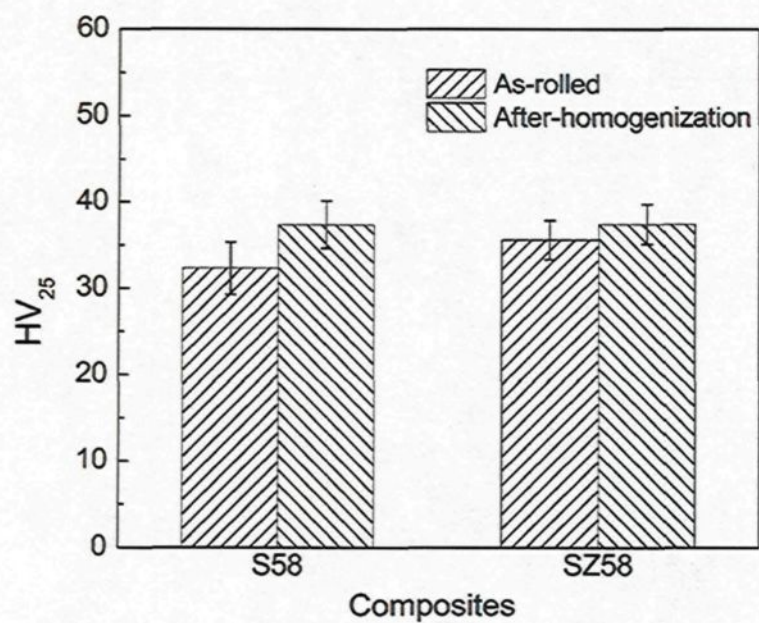


Figure 8.1 Vickers hardness of composite S58 and SZ58 in as-rolled condition and after solution treatment.

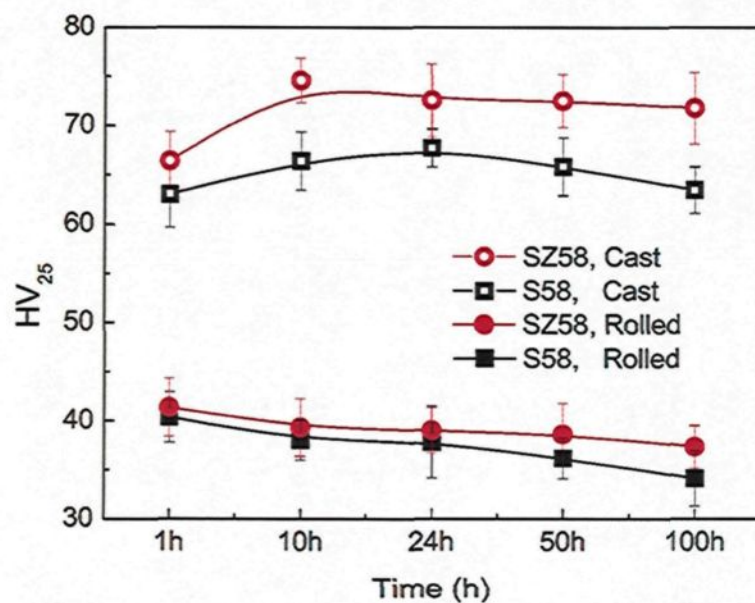


Figure 8.2 Comparison of aging responses of composite S58 and SZ58 at 300 °C prior and after hot rolling.

Figure 8.2 shows the aging responses of the rolled composite sheets in comparison with cast composites. It is very surprising to note that there is no aging response and precipitation strengthening after hot rolling. It is obvious that, under similar heat treatment conditions, the hardness of hot rolled composites is much lower than that of the cast ones and the hardness values further decrease as the aging period is prolonged.

The absence of an aging response in Sc-containing aluminum alloys after application of the hot rolling process has been reported [208]. It was found that hot rolling above a specific temperature (such as 380°C in Ref [208]) leads to precipitation during the rolling process [208, 209] and decreases the potential strengthening effect in the subsequent aging treatment [208].

Two possibilities may be considered to be responsible for the lack of aging responses in Sc- and Zr-containing composites after the post-rolling heat treatment: 1) the precipitates Al_3Sc or $\text{Al}_3(\text{Sc,Zr})$ are formed and coarsen to a critical size during the multi-passes of the hot rolling process, and which are no longer able to dissolve in the homogenization treatment; 2) there is something unknown happened in the hot rolling process and/or the post-rolling heat treatment.

In order to verify the first hypothesis, the S58 as-cast composite samples were first homogenization treated at 640°C for 24 h then aged at 450°C for 100 h to obtain large and coarse Al_3Sc precipitates. Results presented in Chapter 6 indicate that, in this overaging condition, the mean radius of the Al_3Sc precipitates reached above 50nm. Afterwards, these samples were re-treated at 640°C for 24 h then aged at 300°C for 1 and 10 h. As one can

see from Figure 8.3, after the first aging process, the composite matrix almost completely loses its precipitation-strength due to the coarsening of the precipitates. The subsequent re-homogenization plus aging treatment bring back the hardness of the composite to the normal values that are expected from Al_3Sc precipitation hardening. Thus, it means that the unrolled composites containing coarse precipitates are able to form the supersaturated solid solution in the repeated homogenization treatment stage, as well as to re-precipitate the strengthening particles during the subsequent aging stage.

Following the second hypothesis, the as-rolled S58 samples were homogenized at 640 °C for different times, followed by isothermal aging at 300 °C for 10 and 24 h. It can be clearly seen from the results of Figure 8.4 that the homogenization treatment time plays an important role in the precipitation strengthening of the rolled samples. The aging time (10 vs 24 h) has no impact on the hardness. The hardness of the rolled composite rapidly decreases as the homogenization time is extended. The shorter the homogenization time, the higher the hardness of the rolled composite. At the half hour homogenization condition, the hardness of the rolled S58 composite approaches the normal values observed after aging that are expected due to Al_3Sc precipitation hardening. This indicates that the rolled composites are very sensitive to the duration of the homogenization treatment time.

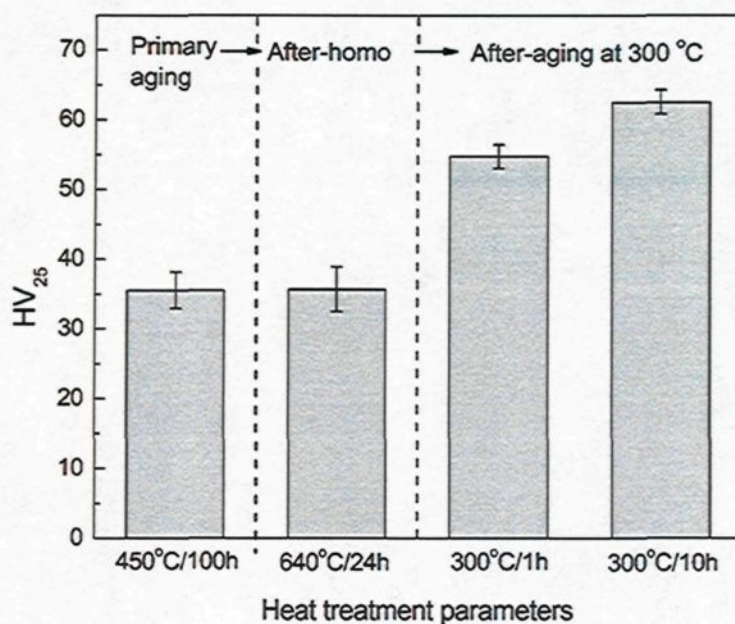


Figure 8.3 Hardness evolution as a function of heat treatment of the as-cast samples of composite S58.

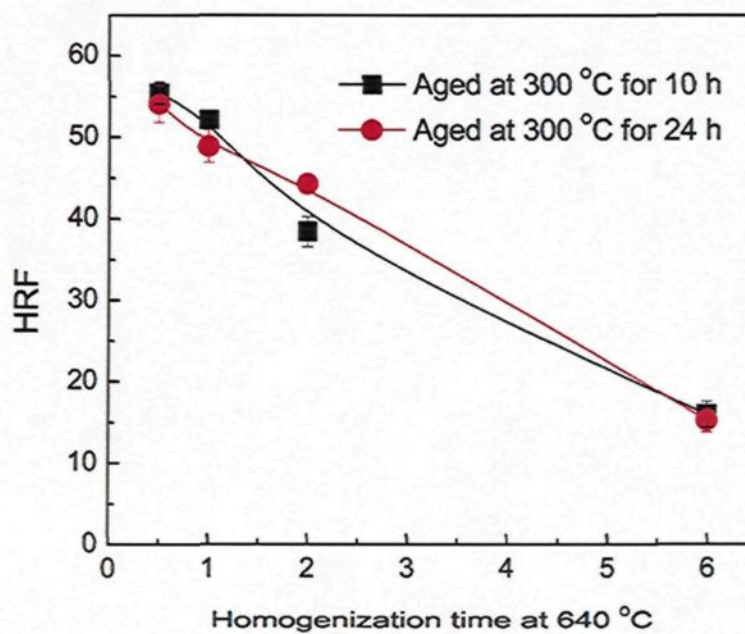


Figure 8.4 Influence of the homogenization treatment time on the precipitation strengthening of as-rolled S58 composites.

8.2.4 Microstructural evolution

Observations on the as-rolled microstructures demonstrate that the multi-pass rolling makes the reinforcements to rotate somewhat and rearrange along the rolling direction (Figure 8.5). Meanwhile, severe deformation (a total of 93% deformation) during multi-pass hot rolling results in the separation of the reaction products (most of them are TiB_2) from the B_4C ceramic particles. Moreover, it is found that the dense and protective reaction layer on some B_4C particles is damaged and a part of the layer is peeled away from the B_4C surfaces (Figure 8.6). It is well known from the results of Chapters 4 and 5 that this dense protective layer plays an important role in limiting the interfacial reactions and the consumption of Sc at the interface.

The TEM and STEM images shown in Figure 8.7 a & b illustrate the Al_3Sc precipitates in the as-rolled S58 composite. It is evident that a number of Al_3Sc precipitates with an average radius of ~ 50 nm existed in the matrix of the as-rolled sample, which indicates that the nanoscale Al_3Sc particles precipitated and coarsened during rolling process. It is also observed that the Al_3Sc precipitates of the rolled composite disappear neither after the homogenization at 640°C for 24 h and nor after the subsequent aging at 300°C for 10 h (Figure 8.7 c & d).

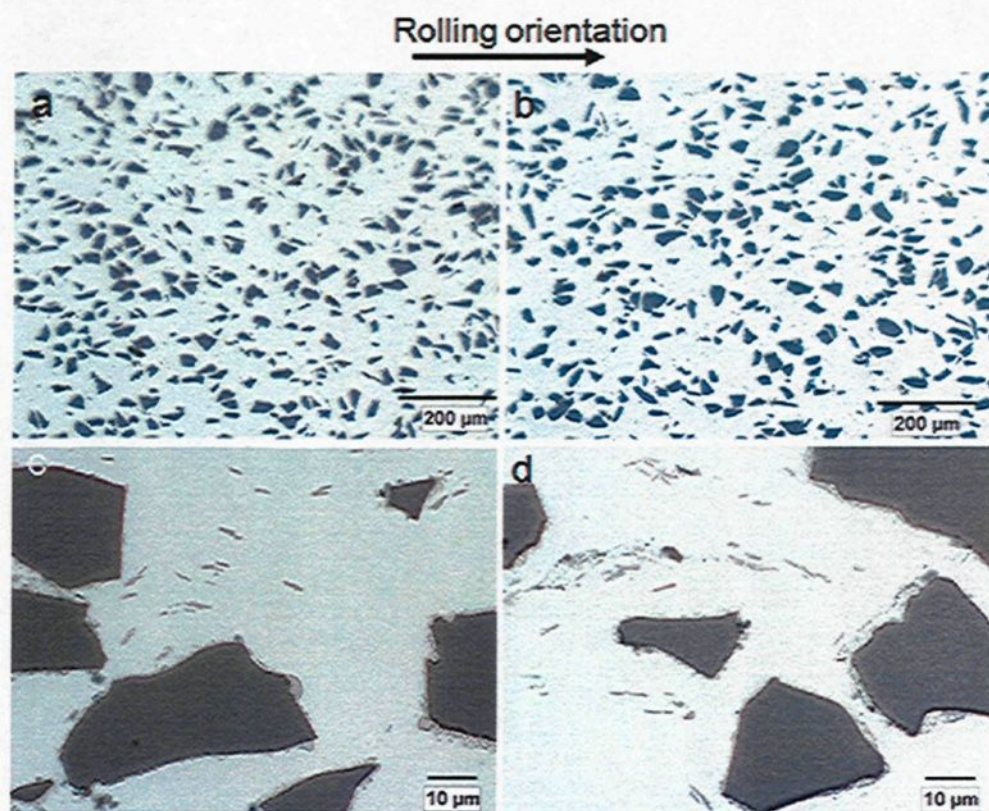


Figure 8.5 Optical microstructures of as-rolled composites S58 (a & c) and SZ58 (b & d), showing the distribution of B_4C particles and reaction products in the aluminum matrix.

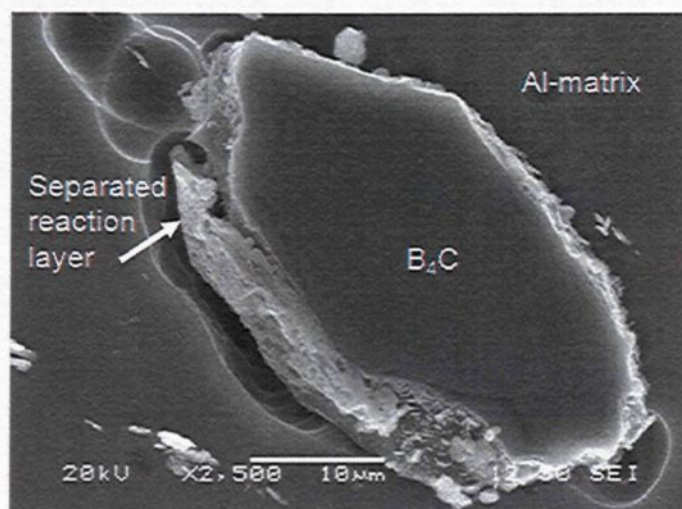


Figure 8.6 SEM image of as-rolled composite S58 after deep etching.

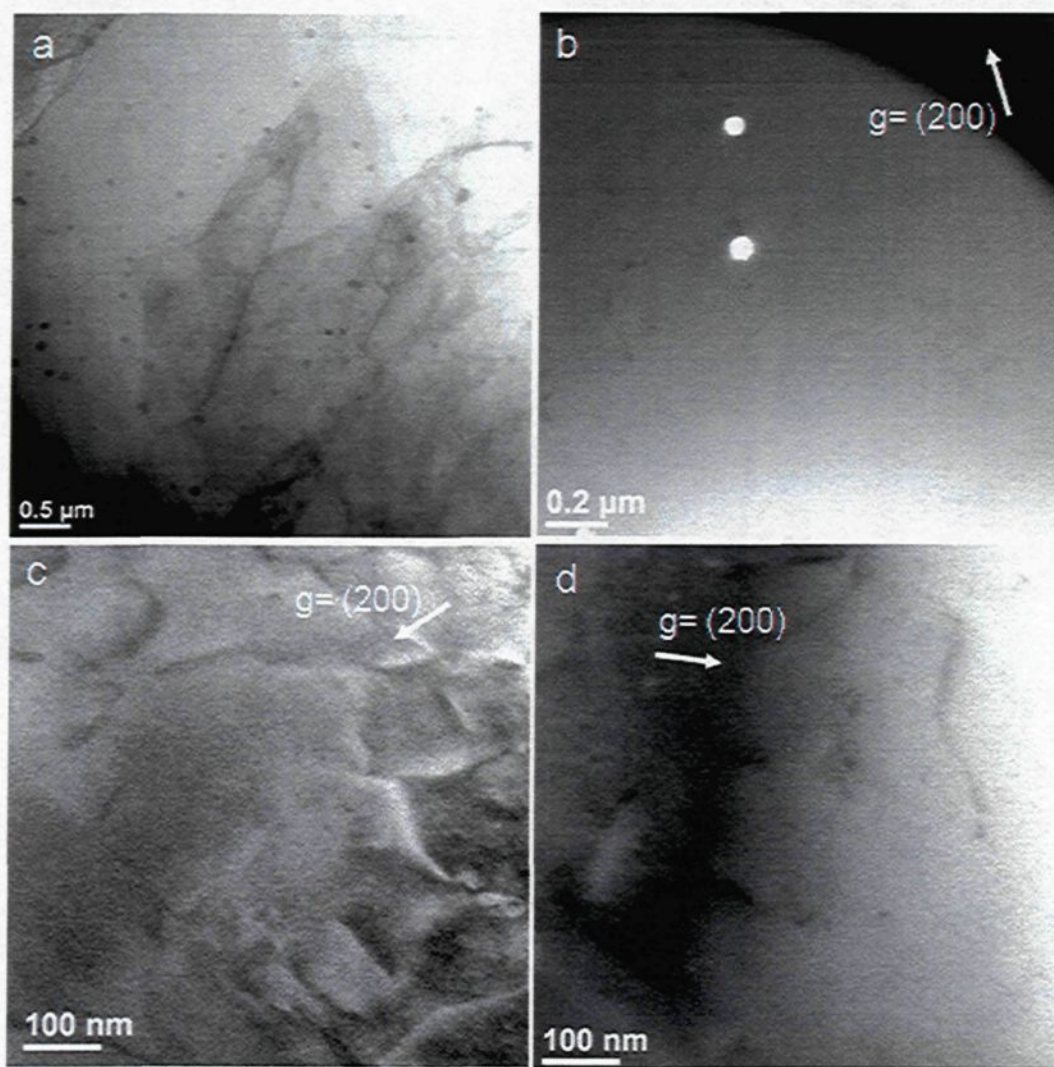


Figure 8.7 The observation of precipitates formed in the matrix of composite S58 after rolling: **a** Bright-field STEM image showing that a large amount of precipitates existed in the matrix of the as-rolled samples. **b** Dark-field TEM image showing the typical morphology of precipitates in as-rolled condition. **c** The absence of precipitates after homogenization treatment at 640°C for 24 h, and **d** following aging process at 300°C for 10 h

8.3 Discussion

In the present work, the Al-B₄C composites containing Sc and Zr were hot-rolled with a total deformation rate of 93%. Then, the post-rolling heat treatments were applied to regain the precipitation strengthening of the composites. However, the results show that the longer the homogenization time, the lower the mechanical properties of the composites are (Figure 8.7). When the homogenization time is longer than six hours, for example, the rolled samples almost completely lose their potential for strengthening due to the lack of Al₃Sc precipitates in the matrix which is necessary to strengthen the matrix. However, this phenomenon is not observed in the as-cast composites for the same heat treatment conditions.

As discussed in Chapter 4, scandium has a strong tendency to react with B₄C particles. This interfacial reaction can be limited when a TiB₂ protective layer completely covers the B₄C particle surface. According to the SEM observations, the hot rolling process leads to the damage of the pre-existing protective layers. This might cause a partial exposure of fresh B₄C surfaces to the matrix alloy. Therefore, it is reasonable to believe that an interfacial reaction could take place between the Al alloy matrix and the uncovered parts of the B₄C particle surfaces. Moreover, the homogenization treatment of hot-rolled composites was carried out at temperature as high as 640 °C, leading to a high diffusivity of Sc in the Al-matrix. In addition, hot rolling may introduce more crystal defects such as dislocations in the rolled materials [210]. These defects could favor solute atom diffusion in the matrix [211]. Therefore, with a longer homogenization time, more solute Sc atoms

would move towards the interfaces to react with the B_4C . This possible reaction would result in the consumption of Sc at the interfaces and consequently reduce the precipitation strengthening during the subsequent aging process.

It is worth mentioning here that, in order to understand this phenomenon and to improve the mechanical properties of hot rolled composites containing Sc and Zr, there are still many unknown. A further study from both process and materials are thus required.

8.4 Summary

In this chapter, the microstructure and mechanical properties of the composites S58 and SZ58 in the hot-rolled and post-rolling heat treatment conditions were studied. Results indicate that Sc- and Zr-containing composites possess a good processability of hot rolling. However, it is found that when the same heat treatment as that used for the cast composites is applied, there is no aging response/precipitation strengthening for the rolled sheets of the same materials. Microstructural observations reveal that hot rolling modifies the particle distribution and the protective layer on the B_4C particle surfaces. The further research revealed that homogenization period at 640 °C exhibits significant influence on the mechanical property obtained in the subsequent aging process. The shorter the homogenization time, the stronger the hardening effect. Therefore, decreasing the homogenization time favours the property restoration of hot rolled material. It may be explained that the protective layer on the B_4C surface was damaged during hot rolling, resulting in the consequent consumption of Sc in the interfacial reactions occurred during the subsequent homogenization treatment.

CHAPTER 9

CONCLUSIONS AND SUGGESTIONS

FOR FUTURE WORK

Chapter 9

Conclusions and Suggestions for Future Work

9.1 Conclusions

In this thesis, a series of novel, thermally stable Al–B₄C metal matrix composites for high temperature applications were developed. The influence of Sc and Zr on the interfacial reactions, the microstructures in the as-cast and aged conditions, the aging response and precipitation strengthening at elevated temperatures, the mechanical properties as well as the long-term thermal stability of Al–15vol.% B₄C composites were investigated. From the experimental results obtained and their analyses, the following conclusions were drawn, which categorized in five parts corresponding to the different aspects that were studied.

1. Effect of Sc, Zr and Ti on the interfacial reactions

B₄C plates were immersed in liquid aluminum alloyed with Sc, Zr and Ti at 730°C. The influences of alloying elements on the interfacial microstructure and reaction products in terms of individual and combined additions were examined.

- All three alloying elements, *i.e.* Sc, Zr and Ti, react with B_4C in liquid Al to form interfacial layers which all consist of two distinctive layers: a fine-crystal layer close to the B_4C and a coarse crystal layer near the Al-matrix.
- The interfacial reactions and the reaction products in each system were identified. The phases Al_3BC , Al_3ScC_3 and ScB_2 were identified as reaction products in the $B_4C/Al-Sc$ system; phases Al_3BC and ZrB_2 in the $B_4C/Al-Zr$ system, as well as Al_3BC and TiB_2 in the $B_4C/Al-Ti$ and $B_4C/Al-Sc-Zr-Ti$ systems were respectively confirmed.
- When Sc, Zr and Ti are introduced in combination, the reaction between Ti and B_4C dominates as the interfacial reaction in $B_4C/Al-Sc-Zr-Ti$ systems, which provides an effective protection to the B_4C particles and reducing the consumption of Sc and Zr at the interface.

2. As-cast microstructure and precipitation evolution in Al- B_4C composites

Sc and Zr were introduced into Al-15vol.% B_4C composites presaturated by Ti and eight experimental composites with different Sc and Zr levels were prepared via a conventional casting technique. The interfacial microstructure, precipitation of Al_3Sc and $Al_3(Sc,Zr)$ as well as the precipitation strengthening effect in the as-cast and peak-aged conditions were studied.

- When Sc is added to the Ti-presaturated Al- B_4C composites, Sc reacts with B_4C and is partially consumed at the interface. When Zr is added in combination with Sc to Al- B_4C composites, traces Zr are detected in interfacial region while the major part of the Zr is retained in the matrix.

- In both Al–Sc and Al–Sc–Zr composites, the *in-situ* interfacial layer formed which covers the B₄C surfaces constitutes two sublayers: a fine crystal layer consisting of Al₃BC, TiB₂ and ScB₂ that is close to the B₄C, and a coarse crystal layer made up of TiB₂ and Al₃ScC₃ towards the Al-matrix.
- Precipitation of nanoscale Al₃Sc and Al₃(Sc,Zr) precipitates are observed in the Sc-containing and Sc-Zr-containing as-cast composite microstructures, respectively, leading to a significant increase in the matrix hardness.
- To achieve an equivalent strengthening effect of Sc in binary Al–Sc alloys, approximately double the amount of Sc is required in the case of Al–B₄C composites.

3. Precipitation strengthening during isothermal aging at 300–450 °C

A series of Al–Sc and Al–Sc–Zr composites with a reinforcement of 15 vol.% B₄C were isothermally aged at 300, 350, 400 and 450 °C for up to 200 h. The effect of Sc and Zr on the aging behavior, precipitation strengthening and precipitate coarsening of composite materials during the aging process were investigated.

- The addition of Sc generates considerable precipitation hardening in the matrix of the composites for aging temperatures from 300 to 450 °C. The precipitation hardening effect increases with the increase of Sc content and decreases with aging temperature. The combination of alloying Sc and Zr in Al–B₄C composites produces a remarkable synergistic effect.
- In the case of the short-term holding (within 200 hrs), the Al–Sc composites are thermally stable up to 300 °C. Al–Sc–Zr composites with a high Zr:Sc ratio (≥ 1) show excellent thermal stability of the strength up to 400°C.

- During aging, Al–Sc and Al–Sc–Zr composites yield two types of nano-size precipitates, Al_3Sc and $\text{Al}_3(\text{Sc,Zr})$, respectively. The diffusivity of Zr in the Al-matrix is significantly smaller than that of Sc, which explains the better coarsening resistance of the $\text{Al}_3(\text{Sc,Zr})$ precipitates.
- The strength increment (calculated from microhardness) as a function of average precipitate radius for both precipitate types at a given temperature shows a good agreement with the theoretical predictions of the Orowan bypassing mechanism. This mechanism is dominating the mechanism for the precipitation hardening of Al_3Sc and $\text{Al}_3(\text{Sc,Zr})$ precipitates.

4. Thermal stability of mechanical properties at elevated temperature

Two experimental composites with 0.4 wt.% Sc and 0.4 wt.% Sc+ 0.24 wt.% Zr were selected to examine the long-term thermal stability of mechanical properties at elevated temperatures of 250 to 350°C for times up to 2000h.

- As the holding time is extended to 2000h, the mechanical properties of the Sc+Zr containing composite are stable up to 300°C, while the Sc-containing composite exhibits a good softening resistance up to 250°C.
- The strengths of both composites decrease with increasing temperatures and prolonged annealing time. The reduction in the mechanical properties of the composites during long term annealing at higher temperatures is dominated by precipitate coarsening.

5. Hot rolling and the post-rolling heat treatment

The influence of hot rolling process and post-rolling heat treatment on the mechanical properties of two experimental composites containing 0.58 wt.% Sc and 0.58 wt.% Sc+0.24 wt.% Zr were studied.

- Composites S58 and SZ58 were hot-rolled to the final 2 mm sheets with good surface quality and both composites possess a good processability of hot rolling.
- When the same heat treatment as that used for the cast composites is applied, no aging response and precipitation strengthening is observed for the rolled sheets of the same materials.
- Homogenization period at 640 °C exhibits significant influence on the mechanical property obtained in the subsequent aging process. The shorter the homogenization time, the stronger the hardening effect. This phenomenon may be related to the damaging of the protective layer on the B₄C surfaces during hot rolling and to further consumption of Sc in the interfacial reactions that occur during homogenization treatment.

9.2 Suggestions for future work

This thesis has shown that Sc and Zr, as the additives introduced in the Al–B₄C composites, could yield good performance in strengthening effect and thermal stability. However, as a new developed material, many questions remain. Additional understanding of the matrix behaviors of the composites could lead to further improvements in the properties. Several possible extensions of this project are proposed:

- **The accurate evaluations of the Sc and Zr concentrations in the matrix for each composites.** In Chapter 5, we roughly evaluated the concentration of these two alloying elements, Sc and Zr, contained in the matrix alloys. Since the contents of the alloying elements are strong related to the property and the stability at elevated temperature, the accurate evaluation of the concentrations of alloying elements in each system are expected.
- **A further study on the phenomenon that the absence of precipitation-hardening effect in hot rolled composites.** In Chapter 8, two hot rolled composites were found to show neither the aging response nor the precipitation-hardening effect in the aging process. According to the preliminary study, it is assumed that the the protective layer on the B₄C surface was damaged during hot rolling, resulting in the consequent consumption of Sc in the interfacial reactions occurred during the subsequent homogenization treatment. However, to prove this hypothesis, more observations need to be done.
- **The optimization of post-rolling heat treatment.** Based on the results so-far, post-rolling heat treatments, including homogenization treatment and the subsequent aging process, provide a critical influence on the mechanical properties of rolled materials. The optimization of these post-rolling treatment is important and thus necessary.
- **Further improvement on the mechanical properties of the composites.** In this project, we tested two composites' properties and obtained the highest yield stress value of ~180 MPa. A Further improvement on mechanical properties seems to be

very attractive. Therefore, replacing the 1xxx by 5xxx series Al alloys as the matrix alloys would be of interest. Since 5xxx series alloys are controlled by the solid solution strengthening mechanism which promises stable increase in the strength at elevated temperature, the properties of composite are expected to be enhanced without the loss of their thermal stability.

APPENDIX

Appendix A

Polishing procedure for Al–B₄C composites

A Successful grinding and polishing procedure produces a surface that accurately represents the structure and contributes to a clear and visual observation of the microstructure. Given that the polishing procedure for Al–B₄C composites is not well established, a brief description of the procedure used in this study is provided below.

For the optical microscopy, it is recommended that the specimen size be limited to dimensions of 2 × 2 cm. A larger size of the specimen requires a longer preparation time and of more difficult to obtain a good surface quality. After cutting a metallographic specimen of appropriate size, mounting of the specimen is often necessary for subsequent handling and metallographic polishing. The corresponding parameters are listed in Table A.1. The details of the polishing procedure used to prepare metallographic specimens of the Al–B₄C composite are listed in Table A.2.

Table A.1 Parameters selection for mounting of specimens

Sample Size (mm)		Force (kN)	Heating time (min)	Cooling time (min)
Diameter	Thickness			
50	18–22	30	5–6	4

Table A.2 Polishing procedure and parameter s

Steps	Polishing procedure		Polishing cloth	Parameters selection				Lubricant
	Polishing Compound	Speed		Speed (o/m)	Force (N) / Dir.	Time	Water	
1	SiC grinding paper (120 grit)	/	/	120	120N/↑↑	20 s × 2	on	/
2	DP-Suspension (15μm)	1 drop every 5 seconds	ANAMET Jay polishing cloth (white)	150	220N/↑↑	13 min	off	DP-Lubricant Blue
3	DP-Suspension (6μm)			150	220N/↑↑	8 min	off	DP-Lubricant Blue
4	DP-Suspension (3μm)			150	210N/↑↑	10 min × 2	off	DP-Lubricant Blue
5	DP-Suspension (1μm)			150	200N/↑↑	10 min	off	DP-Lubricant Red

Appendix B

Procedure of hot rolling

Two cast ingots for each composite, S58 and SZ58, both with a dimension of $28 \times 40 \times 80$ mm were hot-rolled on a laboratory scale rolling mill (STANAT CX-100). Due to the limited capacity of the small mill, multi-passes were applied. The thickness of the cast ingot was reduced from its original value of ~ 28 mm to a final thickness of 2 mm with a total deformation rate of 93%. Before the rolling, the cast ingots of S58 and SZ58 were homogenized at 635 for 24 h and 640 °C for 96 h, respectively. Prior to the rolling and the interval between two steps, the ingot were preheated to 500 °C for 5 to 30 minutes, depending on the thickness of intermediate plates. At two points, when the thickness reduced to 12.75 and 4 mm, respectively, each rolled plate was cut into two pieces. The details of the hot-rolling procedure are given in Appendix B.

Table B.1 Hot-rolling procedure and parameters

Step	Thickness, mm	Decrease, mm	mm/pass	Pass number	Deformation ratio, %	Preheat temperature, °C	Pieces of rolling
1	27.8	5.8	1	6	0.209	500°C	2
2	22	4	1	4	0.182	500°C	2
3	18	3	0.75	4	0.167	500°C	2
4	15	2.25	0.75	3	0.150	500°C	2
5	12.75	2.25	0.75	3	0.176	500°C	2
6	Cutting						6
7	10.5	1	1	1	0.095	500°C	6
8	9.5	0.75	0.75	1	0.079	500°C	6
9	8.5	0.75	0.75	1	0.088	500°C	6
10	8	0.75	0.75	1	0.094	500°C	6
11	7.25	0.75	0.75	1	0.103	500°C	6
12	6.5	0.75	0.75	1	0.115	500°C	6
13	5.75	0.75	0.75	1	0.130	500°C	6
14	5	0.5	0.5	1	0.100	500°C	6
15	4.5	0.5	0.5	1	0.111	500°C	6
16	4	0.5	0.5	1	0.125	500°C	6
17	Cutting						12
18	3.5	0.5	0.5	1	0.143	500°C	12
19	3	0.25	0.25	1	0.083	500°C	12
20	2.75	0.25	0.25	1	0.091	500°C	12
21	2.5	0.25	0.25	1	0.100	500°C	12
22	2.25	0.25	0.25	1	0.111	500°C	12
23	2						12

REFERENCES

1. I. A. Ibrahim, F. A. Mohamed, and E. J. Lavernia, "Particulate Reinforced Metal Matrix Composites – A Review", *Journal of Materials Science*, 1991, **26**(5): 1137-1156.
2. D. E. Alman, U.S. Department of Energy, and Albany Research Center, "Properties of Metal-Matrix Composites", in *ASM Handbook. Volume 21, Composites*. 2001, Material Park, Ohio: ASM International. pp. 838-858.
3. R. M. Mohanty, K. Balasubramanian, and S. K. Seshadri, "Boron Carbide-Reinforced Aluminium 1100 Matrix Composites: Fabrication and Properties", *Materials Science and Engineering A*, 2008, **498**(1-2): 42-52.
4. J. Kusui, K. Hayashi, K. Iwasa, M. Iwase, "Development of Basket for Transport/Storage Cask Using Square Tube Made of Aluminium Alloy Containing Neutron Absorbing Materials", in *14th International Symposium on the Packaging and Transportation of Radioactive Materials 2004*: Berlin, Germany. Paper # 100.
5. X. G. Chen, "Application of Al-B₄C Metal Matrix Composites in the Nuclear Industry for Neutron Absorber Materials", in *Proceedings of solidification processing of metal matrix composites*, N. Gupta and W. H. Hunt, Editors. 2006, TMS 2006: San Antonio, USA. pp. 343-350.
6. X. G. Chen and R. Hark, "Development of Al-30%B₄C Metal Matrix Composites for Neutron Absorber Material", in *TMS Annual Meeting*, 2008, New Orleans, LA. pp. 3-9.
7. G. Bonnet, V. Rohr, X.-G. Chen, J.-L. Bernier, R. Chiocca, and H. Issard, "Use of Alcan's Al-B₄C Metal Matrix Composites as Neutron Absorber Material in Tn International's Transportation and Storage Casks ", *Packaging, Transport, Storage and Security of Radioactive Material*, 2009, **20**(3): 98-102.
8. T. Yamazaki, K. Sanada, T. Nishiyama, H. Ishii, "Development of Neutron Absorber (MaxusTM) for High Burn-up Spent Nuclear Fuel", in *15th International Symposium on the Packaging and Transportation of Radioactive Materials (PATRAM 2007)*. 2007: Miami, Florida, USA. Paper # 228.

9. D. Zhao, F. R. Tuler, and D. J. Lloyd, "Fracture at Elevated-Temperatures in a Particle-Reinforced Composite", *Acta Metallurgica et Materialia*, 1994, **42**(7): 2525-2533.
10. J. G. Kaufman, *Properties of Aluminum Alloys: Tensile, Creep, and Fatigue Data at High and Low Temperatures*. 1999, Materials Park, Ohio: ASM International p. 109.
11. K. E. Knippling, D. C. Dunand, and D. N. Seidman, "Criteria for Developing Castable, Creep-Resistant Aluminum-Based Alloys – A Review", *Zeitschrift Fur Metallkunde*, 2006, **97**(3): 246-265.
12. D. Vojtech, "Challenges for Research and Development of New Aluminum Alloys", *Metallurgija*, 2010, **49**(3): 181-185.
13. Z. H. Zhang, M. F. Bian, and Y. Wang, "Microstructural Characterization of a Rapidly Solidified Al–Sr–Ti Alloy", *Materials Research Bulletin*, 2002, **37**(14): 2303-2314.
14. A. Majumdar and B. C. Muddle, "Microstructure in Rapidly Solidified Al–Ti Alloys", *Materials Science and Engineering A*, 1993, **169**(1-2): 135-147.
15. E. Y. Gutmanas, O. Botstein, and A. Lawley, "Elevated Temperature Stability of Powder Processed Al–Fe–Ni", *International Journal of Powder Metallurgy*, 2000, **36**(2): 47-55.
16. A. Ziani and G. Michot, "Rapidly Solidified Al–Cr–Fe Alloys for Elevated-Temperature Applications: Mechanical Properties and Thermal Stability.2", *International Journal of Non-Equilibrium Processing*, 1997, **10**(1): 59-82.
17. G. W. Meetham, "High-Temperature Materials – A General Review", *Journal of Materials Science*, 1991, **26**(4): 853-860.
18. J. Royset, N. Ryum, D. Bettella, A. Tocco, Z. H. Jia, J. K. Solberg, *et al.*, "On the Addition of Precipitation- and Work-Hardening in an Al–Sc Alloy", *Materials Science and Engineering A*, 2008, **483-484**: 175-178.

19. E. A. Marquis, D. N. Seidman, and D. C. Dunand, "Precipitation Strengthening at Ambient and Elevated Temperatures of Heat-Treatable Al(Sc) Alloys", *Acta Materialia*, 2002, **50**(16): 4021-4035.
20. B. A. Parker, Z. F. Zhou, and P. Nolle, "The Effect of Small Additions of Scandium on the Properties of Aluminum-Alloys", *Journal of Materials Science*, 1995, **30**(2): 452-458.
21. V. V. Zakharov, "Effect of Scandium on the Structure and Properties of Aluminum Alloys", *Metal Science and Heat Treatment*, 2003, **45**(7-8): 246-253.
22. V. V. Zakharov, "Effect of Scandium on the Structure and Properties of Aluminum Alloys", *Metal Science and Heat Treatment*, 2003, **45**(7-8): 246-253.
22. K. E. Knipling, D. N. Seidman, and D. C. Dunand, "Ambient- and High-Temperature Mechanical Properties of Isochronally Aged Al-0.06Sc, Al-0.06Zr and Al-0.06Sc-0.06Zr (at.%) Alloys", *Acta Materialia*, 2011, **59**: 943-954.
23. C. B. Fuller, D. N. Seidman, and D. C. Dunand, "Mechanical Properties of Al(Sc,Zr) Alloys at Ambient and Elevated Temperatures", *Acta Materialia*, 2003, **51**(16): 4803-4814.
24. K. E. Knipling, R. A. Karnesky, C. P. Lee, D. C. Dunand, and D. N. Seidman, "Precipitation Evolution in Al-0.1Sc, Al-0.1Zr and Al-0.1Sc-0.1Zr (at.%) Alloys During Isochronal Aging", *Acta Materialia*, 2010, **58**(15): 5184-5195.
25. Z. Zhang, X. G. Chen, and A. Charette, "Fluidity and Microstructure of an Al-10% B₄C Composite", *Journal of Materials Science*, 2009, **44**(2): 492-501.
26. Z. Zhang, K. Fortin, A. Charette, and X. G. Chen, "Effect of Titanium on Microstructure and Fluidity of Al-B₄C Composites", *Journal of Materials Science*, 2011, **46**(9): 3176-3185.
27. J. K. Jung and S. Kang, "Advances in Manufacturing Boron Carbide-Aluminum Composites", *Journal of the American Ceramic Society*, 2004, **87**(1): 47-54.

28. J. C. Viala, J. Bouix, G. Gonzalez, and C. Esnouf, "Chemical Reactivity of Aluminium with Boron Carbide", *Journal of Materials Science*, 1997, **32**(17): 4559-4573.
29. X. G. Chen, "Interface Reaction of Boron Carbide in Aluminum Matrix Composites and Its Control", in *EPD Congress 2005*, M. E. Schlesinger, Editor. 2005, TMS 2005. pp. 101-106.
30. P. Haasen, "Chapter 23 . Mechanical Properties of Solid Solutions", in *Physical Metallurgy*, R. W. Cahn, P. Haasen, Eds. 1996, Amsterdam: Elsevier Science. pp. 2010-2073.
31. G. E. Dieter and D. Bacon, *Mechanical Metallurgy*. 1988, London: McGraw-Hill. pp. 212-220, 229-233.
32. E. Nembach, *Particle Strengthening of Metals and Alloys*. 1997, New York: Wiley. pp. 63-144.
33. A. S. Argon and E. Orowan, *Physics of Strength and Plasticity*. 1969, Cambridge: M.I.T. Press. pp. 113-131.
34. A. Kelly and R. Nicholson, *Strengthening Methods in Crystals*. 1971, Amsterdam; New York: Elsevier Pub. Co. pp. 12-120.
35. M. K. Surappa, "Aluminium Matrix Composites: Challenges and Opportunities", *Sadhana-Academy Proceedings in Engineering Sciences*, 2003, **28**: 319-334.
36. N. Chawla and Y. L. Shen, "Mechanical Behavior of Particle Reinforced Metal Matrix Composites", *Advanced Engineering Materials*, 2001, **3**(6): 357-370.
37. R. Asthana, "Properties of Cast Composites", in *Solidification Processing of Reinforced Metals*. 1998, Zurich-Uetikon: Trans Tech Publications Ltd. pp. 351-398.
38. A. R. Chambers, "The Machinability of Light Alloy MMCs", *Composites Part A-Applied Science and Manufacturing*, 1996, **27**(2): 143-147.

39. T. W. Clyne and P. J. Withers, *An Introduction to Metal Matrix Composites*. Cambridge Solid State Science Series. 1993, Cambridge [England]: New York, NY, USA : Cambridge University Press. pp. 1-9.
40. D. B. Miracle, S. L. Donaldson, and ASM International Handbook Committee, *ASM Handbook. Volume 21, Composites*. 2001, Material Park, Ohio: ASM International. pp. 3-18, 19-26, 51-55
41. M. Taya, "Strengthening Mechanisms of Metal Matrix Composites", *Materials Transactions JIM*, 1991, **32**(1): 1-19.
42. M. Taya, K. E. Lulay, and D. J. Lloyd, "Strengthening of A Particulate Metal Matrix Composite by Quenching", *Acta Metallurgica*, 1991, **39**(1): 73-87.
43. M. E. Smagorinski, P. G. Tsantrizos, S. Grenier, T. Brzezinski, and G. Kim, "The Properties and Microstructure of Al-Based Composites Reinforced with Ceramic Particles", *Materials Science and Engineering A*, 1998, **244**(1): 86-90.
44. O. Ryen, O. Nijs, E. Sjolander, B. Holmedal, H. E. Ekstrom, and E. Nes, "Strengthening Mechanisms in Solid Solution Aluminum Alloys", *Metallurgical and Materials Transactions A*, 2006, **37A**(6): 1999-2006.
45. S. L. Kakani and A. Kakani, *Material Science*. 2004, New Delhi: New Age International. p. 101.
46. W. D. Callister, *Materials Science and Engineering : An Introduction*. 2007, New York: John Wiley & Sons. pp. 188-189.
47. N. Hansen, "Polycrystalline Strengthening", *Metallurgical Transactions A*, 1985, **16**(12): 2167-2190.
48. B. Q. Han and E. J. Lavernia, "High-Temperature Behavior of a Cryomilled Ultrafine-Grained Al-7.5% Mg Alloy", *Materials Science and Engineering A*, 2005, **410-411**: 417-421.

49. B. Q. Han and E. J. Lavernia, "Enhanced Tensile Ductility in a Nanostructured Al-7.5%Mg Alloy", *Materials Science & Technology*, 2005, **21**(7): 855-860.
50. F. Zhou, X. Z. Liao, Y. T. Zhu, S. Dallek, and E. J. Lavernia, "Microstructural Evolution During Recovery and Recrystallization of a Nanocrystalline Al-Mg Alloy Prepared by Cryogenic Ball Milling", *Acta Materialia*, 2003, **51**(10): 2777-2791.
51. B. Q. Han, E. J. Lavernia, and F. A. Mohamed, "Mechanical Behavior of a Cryomilled near-Nanostructured Al-Mg-Sc Alloy", *Metallurgical and Materials Transactions A*, 2005, **36A**(2): 345-355.
52. A. J. Ardell, "Precipitation Hardening", *Metallurgical Transactions A*, 1985, **16**: 2131-2165.
53. R. E. Smallman and A. H. W. Ngan, *Physical Metallurgy and Advanced Materials*. 2007, London: Elsevier. pp. 332-339, 394-399.
54. M. Ahlers, "Stacking Fault Energy and Mechanical Properties", *Metallurgical Transactions*, 1970, **1**(9): 2415-2428.
55. P. B. Hirsch and A. Kelly, "Stacking-Fault Strengthening", *Philosophical Magazine*, 1965, **12**(119): 881-900.
56. E. Nembach, "Precipitation Hardening Caused by a Difference in Shear Modulus between Particle and Matrix", *Physica Status Solidi A*, 1983, **78**(2): 571-581.
57. B. Joos and M. S. Duesbery, "The Peierls Stress of Dislocations: An Analytic Formula", *Physical Review Letters*, 1997, **78**(2): 266-269.
58. V. P. Kisel, "Mechanism of Formation and Mechanical-Behavior of Tilt Grain-Boundaries", *Physica Status Solidi A* 1995, **149**(1): 61-68.
59. N. S. Kissel and V. P. Kisel, "Microscopic Mechanisms of Low-Temperature Yield Stress Anomaly in Solids", *Materials Science and Engineering A*, 2001, **309**: 97-101.

60. M. A. Meyers, K. K. Chawla, *Mechanical Metallurgy: Principles and Applications*. 1984, Paramus, NJ: Englewood Cliffs. pp. 329-332.
61. J. H. Westbrook, R. L. Fleischer, and Knovel, Eds. *Structural Applications of Intermetallic Compounds*. Vol. 3. 2000, Wiley: New York. p. 269.
62. R. D. Doherty, "Chapter 15 . Diffusive Phase Transformiom in the Solid State", in *Physical Metallurgy*, R. W. Cahn and P. Haasen, Eds. 1996, Netherlands: Elsevier Science. pp. 1434-1451.
63. I. M. Lifshitz and V. V. Slyozov, "The Kinetics of Precipitation from Supersaturated Solid Solutions", *Journal of Physics and Chemistry of Solids*, 1961, **19**(1-2): 35-50.
64. C. Wagner, "Theorie Der Alterung Von Niederschlagen Durch Umlosen (Ostwald-Reifung)", *Zeitschrift Für Elektrochemie*, 1961, **65**(7-8): 581-591.
65. A. J. Ardell, "Microstructural Stability at Elevated Temperatures", *Journal of the European Ceramic Society*, 1999, **19**(13-14): 2217-2231.
66. P. W. Voorhees, "The Theory of Ostwald Ripening", *Journal of Statistical Physics*, 1985, **38**(1-2): 231-252.
67. C. Watanabe, T. Kondo, and R. Monzen, "Coarsening of Al₃Sc Precipitates in an Al-0.28 Wt Pct Sc Alloy", *Metallurgical and Materials Transactions A*, 2004, **35A**(9): 3003-3008.
68. E. A. Marquis and D. N. Seidman, "Nanoscale Structural Evolution of Al₃ Sc Precipitates in Al(Sc) Alloys", *Acta Materialia*, 2001, **49**(11): 1909-1919.
69. C. J. Kuehmann and P. W. Voorhees, "Ostwald Ripening in Ternary Alloys", *Metallurgical and Materials Transactions A*, 1996, **27**(4): 937-943.

70. R. A. Karnesky, D. C. Dunand, and D. N. Seidman, "Evolution of Nanoscale Precipitates in Al Microalloyed with Sc and Er", *Acta Materialia*, 2009, **57**(14): 4022-4031.
71. E. A. Marquis and D. N. Seidman, "Coarsening Kinetics of Nanoscale Al₃Sc Precipitates in an Al–Mg–Sc Alloy", *Acta Materialia*, 2005, **53**(15): 4259-4268.
72. C. B. Fuller and D. N. Seidman, "Temporal Evolution of the Nanostructure of Al(Sc,Zr) Alloys: Part II–Coarsening of Al₃(Sc_{1-x}Zr_x) Precipitates", *Acta Materialia*, 2005, **53**(20): 5415-5428.
73. M. E. Drits, L. L. Rokhlin, and N. I. Nikitina, "Phase-Equilibria in Magnesium-Rich Mg–Y–Sc Alloys", *Russian Metallurgy*, 1976, (4): 187-190.
74. V. L. Kononenko and S. V. Golubev, "Phase-Diagrams of Binary-Systems of Aluminum with La, Ce, Pr, Nd, Sm, Eu, Yb, Sc and Y", *Russian Metallurgy*, 1990, (2): 193-195.
75. H. Luo, L. Shawa, L. C. Zhang, and D. Miracle, "On Tension/Compression Asymmetry of an Extruded Nanocrystalline Al–Fe–Cr–Ti Alloy", *Materials Science and Engineering A*, 2005, **409**: 249-256.
76. M. Zedalis and M. E. Fine, "Lattice-Parameter Variation of Al₃(Ti,V,Zr,Hf) in Al-2 at-Percent (Ti,V,Zr,Hf) Alloys", *Scripta Metallurgica*, 1983, **17**(10): 1247-1251.
77. J. F. Nie and B. C. Muddle, "High Temperature Precipitation Hardening in a Rapidly Quenched Al–Ti–Ni Alloy I. Precipitation Hardening Response", *Materials Science and Engineering A*, 1996, **221**: 11-21.
78. V. G. Davydov, T. D. Rostova, V. V. Zakharov, Y. A. Filatov, and V. I. Yelagin, "Scientific Principles of Making an Alloying Addition of Scandium to Aluminium Alloys", *Materials Science and Engineering A*, 2000, **280**(1): 30-36.
79. L. A. Willey, "Aluminum Scandium Alloy " USA Patent 3619181, 1971.

80. M. E. Drits, E. S. Kadaner, Dobatkin.Tv, and N. I. Turkina, "Scandium–Aluminum Interactions in Aluminum-Rich Side of Al–Sc System", *Russian Metallurgy*, 1973, (4): 152-154.
81. M. E. Drits, L. S. Toropova, Y. G. Bykov, F. L. Gushchina, V. I. Elagin, and Y. A. Filatov, "Metastable State Diagram of the Al–Sc System in the Range Rich in Aluminum", *Russian Metallurgy*, 1983, (1): 150-153.
82. V. I. Elagin, V.V. Zakharov, A.A. Petrova, E.V. Vyshegorodtseva "Influence of Scandium on the Structure and Properties of Al–Zn–Mg Alloys", *Russian Metallurgy*, 1983, (4): 143-146.
83. V. I. Elagin, V. V. Zakharov, and T. D. Rostova, "Some Features of Decomposition for the Solid-Solution of Scandium in Aluminum", *Metal Science and Heat Treatment*, 1983, **25**(7-8): 546-549.
84. V. I. Elagin, V. V. Zakharov, and T. D. Rostova, "Scandium-Alloyed Aluminum-Alloys", *Metal Science and Heat Treatment*, 1992, **34**(1-2): 37-45.
85. V. I. Elagin, V. V. Zakharov, and T. D. Rostova, "Effect of Scandium on the Structure and Properties of Alloy Al–5.5% Zn–2.0% Mg", *Metal Science and Heat Treatment*, 1994, **36**(7-8): 375-380.
86. Y. Harada and D. C. Dunand, "Microstructure of Al₃ Sc with Ternary Transition-Metal Additions", *Materials Science and Engineering A*, 2002, **329-331**: 686-695.
87. M. van Dalen, "Microstructure and Creep Properties of Al-Sc Alloys Micro-Alloyed with Lanthanides (Yb or Gd) and Transition Metals (Ti or Zr)," Ph.D. Thesis , Materials Science and Engineering, Northwestern University, Evanston, 2007.
88. B. Forbord, L. Auran, W. Lefebvre, H. Hallem, and K. Marthinsen, "Rapid Precipitation of Dispersoids During Extrusion of an Al–0.91 wt.% Mn–0.13 wt.% Zr–0.17 wt.% Sc–Alloy", *Materials Science and Engineering A*, 2006, **424**(1-2): 174-180.
89. J. Royset and N. Ryum, "Scandium in Aluminium Alloys", *International Materials Reviews*, 2005, **50**(1): 19-44.

90. S. I. Fujikawa, M. Sugaya, H. Takei, and K. Hirano, "Solid Solubility and Residual Resistivity of Scandium in Aluminum", *Journal of the Less-Common Metals*, 1979, **63**(1): 87-97.
91. J. L. Murray, "The Al–Sc (Aluminum–Scandium) System", *Journal of Phase Equilibria*, 1998, **19**(4): 380-384.
92. L. S. Toropova, *Advanced Aluminum Alloys Containing Scandium : Structure and Properties*. 1998, Amsterdam, The Netherlands: Gordon and Breach Science Publishers. pp. 6-20, 55-59, 69-94, 133-151.
93. A. F. Norman, P. B. Prangnell, and R. S. McEwen, "The Solidification Behaviour of Dilute Aluminium–Scandium Alloys", *Acta Materialia*, 1998, **46**(16): 5715-5732.
94. R. W. Hyland, "Homogeneous Nucleation Kinetics of Al₃Sc in a Dilute Al–Sc Alloy", *Metallurgical Transactions A*, 1992, **23**(7): 1947-1955.
95. G. M. Novotny and A. J. Ardell, "Precipitation of Al₃Sc in Binary Al–Sc Alloys", *Materials Science and Engineering A*, 2001, **318**(1-2): 144-154.
96. N. Sano, Y. Hasegawa, K. Hono, H. Jo, K. Hirano, H. W. Pickering, *et al.*, "Precipitation Process of Al-Sc Alloys", *Journal de Physique*, 1987, **48**(C-6): 337-342.
97. S. Iwamura and Y. Miura, "Loss in Coherency and Coarsening Behavior of Al₃Sc Precipitates", *Acta Materialia*, 2004, **52**(3): 591-600.
98. T. G. Nieh, L. M. Hsiung, J. Wadsworth, and R. Kaibyshev, "High Strain Rate Superplasticity in a Continuously Recrystallized Al–6%Mg–0.3%Sc Alloy", *Acta Materialia*, 1998, **46**(8): 2789-2800.
99. T. G. Nieh, R. Kaibyshev, L. M. Hsiung, N. Nguyen, and J. Wadsworth, "Subgrain Formation and Evolution During the Deformation of an Al–Mg–Sc Alloy at Elevated Temperatures", *Scripta Materialia*, 1997, **36**(9): 1011-1016.

100. J. S. Vetrano, S. M. Bruemmer, L. M. Pawlowski, and I. M. Robertson, "Influence of the Particle Size on Recrystallization and Grain Growth in Al–Mg–X Alloys", *Materials Science and Engineering A*, 1997, **238**: 101-107.
101. N. Blake and M. A. Hopkins, "Constitution and Age Hardening of Al–Sc Alloys", *Journal of Materials Science*, 1985, **20**(8): 2861-2867.
102. K. B. Hyde, A. F. Norman, and P. B. Prangnell, "The Effect of Cooling Rate on the Morphology of Primary Al₃Sc Intermetallic Particles in Al–Sc Alloys", *Acta Materialia*, 2001, **49**(8): 1327-1337.
103. V. Singh, K. S. Prasad, and A. A. Gokhale, "Effect of Minor Sc Additions on Structure, Age Hardening and Tensile Properties of Aluminium Alloy AA8090 Plate", *Scripta Materialia*, 2004, **50**(6): 903-908.
104. R. A. Karnesky, M. E. van Dalen, D. C. Dunand, and D. N. Seidman, "Effects of Substituting Rare-Earth Elements for Scandium in a Precipitation-Strengthened Al–0.08 at. %Sc Alloy", *Scripta Materialia*, 2006, **55**(5): 437-440.
105. E. A. Marquis, D. N. Seidman, and D. C. Dunand, "Effect of Mg Addition on the Creep and Yield Behavior of an Al–Sc Alloy", *Acta Materialia*, 2003, **51**(16): 4751-4760.
106. M. E. Drits, J. Dutkiewicz, L. S. Toropova, and J. Salawa, "The Effect of Solution Treatment on the Aging Processes of Al–Sc Alloys", *Crystal Research and Technology*, 1984, **19**(10): 1325-1330.
107. V. I. Z. Elagin, V V; Pavlenko, S G; Rostova, T D "Influence of Zirconium Additions on Aging of Aluminum–Scandium Alloys. (Translation) ", *Physics of Metals and Metallography*, 1985, **60**(1): 88-92.
108. H. H. Jo and S. I. Fujikawa, "Kinetics of Precipitation in Al–Sc Alloys and Low-Temperature Solid Solubility of Scandium in Aluminum Studied by Electrical-Resistivity Measurements", *Materials Science and Engineering A*, 1993, **171**(1-2): 151-161.

109. M. Nakayama, A. Furuta, and Y. Miura, "Precipitation of Al₃Sc in Al-0.23 mass% Sc Alloy", *Materials Transactions JIM*, 1997, **38**(10): 852-857.
110. O. Beeri, D. C. Dunand, and D. N. Seidman, "Roles of Impurities on Precipitation Kinetics of Dilute Al-Sc Alloys", *Materials Science and Engineering A*, 2010, **527**(15): 3501-3509.
111. V. G. Davydov, V. I. Elagin, V. V. Zakharov, and T. D. Rostova, "Alloying Aluminum Alloys with Scandium and Zirconium Additives", *Metal Science and Heat Treatment*, 1996, **38**(7-8): 347-352.
112. B. Forbord, H. Hallem, J. Royset, and K. Marthinsen, "Thermal Stability of Al₃(Sc_xZr_{1-x})-Dispersoids in Extruded Aluminium Alloys", *Materials Science and Engineering A*, 2008, **475**(1-2): 241-248.
113. Y. W. Riddle and T. H. Sanders, "A Study of Coarsening, Recrystallization, and Morphology of Microstructure in Al-Sc-(Zr)-(Mg) Alloys", *Metallurgical And Materials Transactions A*, 2004, **35A**(1): 341-350.
114. N. A. Belov, A. N. Alabin, D. G. Eskin, and V. V. Istomin-Kastrovskii, "Optimization of Hardening of Al-Zr-Sc Cast Alloys", *Journal of Materials Science*, 2006, **41**: 5890-5899.
115. N. A. Belov, D. G. Eskin, and A. A. Aksenov, *Multicomponent Phase Diagrams : Applications for Commercial Aluminum Alloys*. 2005, Amsterdam; Boston: Elsevier. p. 292.
116. R. Galun, B. L. Mordike, T. Maiwald, B. Smola, R. Mergen, M. Manner, *et al.*, "Microstructure and Age-Hardening Effects of Aluminium Alloys with Additions of Scandium and Zirconium", *Zeitschrift für Metallkunde*, 2004, **95**(12): 1142-1146.
117. A. N. Kamardinkin, T. V. Dobatkina, and T. D. Rostova, "Isothermal Sections of the Al-Sc-Zr System at 550 and 600°C in the Region Enriched in Aluminum", *Russian Metallurgy*, 1991, (2): 216-218.

118. C. B. Fuller, J. L. Murray, and D. N. Seidman, "Temporal Evolution of the Nanostructure of Al(Sc,Zr) Alloys: Part I - Chemical Compositions of $Al_3(Sc_{1-x}Zr_x)$ Precipitates", *Acta Materialia*, 2005, **53**(20): 5401-5413.
119. P. N. Raju, K. S. Rao, G. M. Reddy, M. Kamaraj, and K. P. Rao, "Microstructure and High Temperature Stability of Age Hardenable AA2219 Aluminium Alloy Modified by Sc, Mg and Zr Additions", *Materials Science and Engineering A*, 2007, **464**(1-2): 192-201.
120. K. Yu, W. X. Li, S. R. Li, and J. Zhao, "Mechanical Properties and Microstructure of Aluminum Alloy 2618 with $Al_3(Sc,Zr)$ Phases", *Materials Science and Engineering A*, 2004, **368**(1-2): 88-93.
121. E. Clouet, L. Lae, T. Epicier, W. Lefebvre, M. Nastar, and A. Deschamps, "Complex Precipitation Pathways in Multicomponent Alloys", *Nature Materials*, 2006, **5**(6): 482-488.
122. A. Tolley, V. Radmilovic, and U. Dahmen, "Segregation in $Al_3(Sc,Zr)$ Precipitates in Al-Sc-Zr Alloys", *Scripta Materialia*, 2005, **52**(7): 621-625.
123. S. I. Fujikawa, "Impurity Diffusion of Scandium in Aluminum", *Defect and Diffusion Forum*, 1997, **143**: 115-120.
124. E. Clouet, A. Barbu, L. Lae, and G. Martin, "Precipitation Kinetics of Al_3Zr and Al_3Sc in Aluminum Alloys Modeled with Cluster Dynamics", *Acta Mater.*, 2005, **53**: 2313-2325.
125. O. N. Senkov, M. R. Shagiev, S. V. Senkova, and D. B. Miracle, "Precipitation of $Al_3(Sc,Zr)$ Particles in an Al-Zn-Mg-Cu-Sc-Zr Alloy During Conventional Solution Heat Treatment and Its Effect on Tensile Properties", *Acta Materialia*, 2008, **56**(15): 3723-3738.
126. C. B. Fuller, A. R. Krause, D. C. Dunand, and D. N. Seidman, "Microstructure and Mechanical Properties of a 5754 Aluminum Alloy Modified by Sc and Zr Additions", *Materials Science and Engineering A*, 2002, **338**(1-2): 8-16.

127. K. E. Knipling, D. C. Dunand, and D. N. Seidman, "Atom Probe Tomographic Studies of Precipitation in Al-0.1Zr-0.1Ti (at.%) Alloys", *Microscopy and Microanalysis*, 2007, **13**(6): 503-516.
128. P. Malek, M. Janecek, and B. Smola, "Structure and Properties of Melt-Spun Al-Zr-Ti Alloys IV. Microstructure and Microhardness Stability at Elevated Temperatures", *Kovove Materialy-Metallic Materials*, 2000, **38**(3): 160-177.
129. M. E. van Dalen, D. C. Dunand, and D. N. Seidman, "Effects of Ti Additions on the Nanostructure and Creep Properties of Precipitation-Strengthened Al-Sc Alloys", *Acta Materialia*, 2005, **53**(15): 4225-4235.
130. K. B. Hyde, A. F. Norman, and P. B. Prangnell, "The Effect of Ti on Grain Refinement in Al-Sc Alloys", in *Aluminum Alloys 2002: Their Physical and Mechanical Properties Pts 1-3*. 2002, Zurich-Uetikon: Trans Tech Publications Ltd. pp. 39-44.
131. B. Forbord, W. Lefebvre, F. Danoix, H. Hallem, and K. Marthinsen, "Three Dimensional Atom Probe Investigation on the Formation of Al₃(Sc,Zr)-Dispersoids in Aluminium Alloys", *Scripta Materialia*, 2004, **51**(4): 333-337.
132. T. S. Srivatsan, T. S. Sudarshan, and E. J. Lavernia, "Processing of Discontinuously-Reinforced Metal-Matrix Composites by Rapid Solidification", *Progress in Materials Science*, 1995, **39**(4-5): 317-409.
133. S. Suresh, A. Mortensen, and A. Needleman, *Fundamentals of Metal-Matrix Composites*. 1993, Boston; London; Oxford [etc.]: Butterworth-Heinemann. pp. 297-326.
134. N. Chawla and K. K. Chawla, *Metal Matrix Composites*. 2006, New York: Springer. pp. 1-42.
135. R. Asthana, "Processing Effects on the Engineering Properties of Cast Metal-Matrix Composites", *Advanced Performance Materials*, 1998, **5**(3): 213-255.

136. T. M. Lillo, "Enhancing Ductility of Al6061 + 10 wt.% B₄C through Equal-Channel Angular Extrusion Processing", *Materials Science and Engineering A*, 2005, **410**: 443-446.
137. G. M. Bond and O. T. Inal, "Shock-Compacted Aluminum Boron-Carbide Composites", *Composites Engineering*, 1995, **5**(1): 9-16.
138. J. Hemanth, "Tribological Behavior of Cryogenically Treated B₄Cp/Al-12% Si Composites", *Wear*, 2005, **258**: 1732-1744.
139. F. Thevenot, "Boron Carbide – A Comprehensive Review", *Journal of the European Ceramic Society*, 1990, (6): 205-225.
140. X. G. Chen, "Interface Reaction of Boron Carbide in Aluminum Matrix Composites and Its Control", in *EPD Congress 2005*, 2005: TMS pp. 101-106.
141. M. T. Gericke, J. D. Bowman, R. D. Carlini, T. E. Chupp, K. P. Coulter, M. Dabaghyan, *et al.*, "Commissioning of the NPDGamma Detector Array: Counting Statistics in Current Mode Operation and Parity Violation in the Capture of Cold Neutrons on B₄C and Al-27", *Journal of Research of the National Institute of Standards and Technology*, 2005, **110**(3): 215-219.
142. J. C. Ye, J. H. He, and J. M. Schoenung, "Cryomilling for the Fabrication of a Particulate B₄C Reinforced Al Nanocomposite: Part I. Effects of Process Conditions on Structure", *Metallurgical and Materials Transactions A*, 2006, **37**(10): 3099-3109.
143. S. K. Jinkwan Jung, "Advances in Manufacturing Boron Carbide-Aluminum Composites", *Journal of the American Ceramic Society*, 2004, **87**(1): 47-54.
144. K. B. Lee, H. S. Sim, S. Y. Cho, and H. Kwon, "Reaction Products of Al-Mg: B₄ C Composite Fabricated by Pressureless Infiltration Technique", *Materials Science and Engineering A*, 2001, **302**: 227-234.
145. K. B. Lee, H. S. Sim, H. R. Yang, and H. Kwon, "On Carbide Particle Reinforced Al Composites Fabricated by Pressureless Infiltration Technique", *Materials Science Forum*, 2005, **475-479**: 971-974.

146. A. R. Kennedy, "The Microstructure and Mechanical Properties of Al-Si-B₄C Metal Matrix Composites", *Journal of Materials Science*, 2002, **37**: 317-323.
147. L. L. N. Frage, N. Frumin, M. Gelbstein, M.P. Dariel, "Manufacturing B₄C-(Al,Si) Composite Materials by Metal Alloy Infiltration", *Journal of Materials Processing Technology*, 2003, **143-144**: 486-490 .
148. J. C. Ye, Z. Lee, B. Ahn, J. H. He, S. R. Nutt, and J. M. Schoenung, "Cryomilling for the Fabrication of a Particulate B₄C Reinforced Al Nanocomposite: Part II. Mechanisms for Microstructural Evolution", *Metallurgical and Materials Transactions A*, 2006, **37A**(10): 3111-3117.
149. C. Ponzi, "Metal Matrix Composite Fabrication Processes for High Performance Aerospace Structures", *Composites Manufacturing*, 1992, **3**(1): 32-42.
150. T. S. Srivatsan, I. A. Ibrahim, F. A. Mohamed, and E. J. Lavernia, "Processing Techniques for Particulate-Reinforced Metal Aluminium Matrix Composites", *Journal of Materials Science*, 1991, **26**(22): 5965-5978.
151. J. Zhou and J. Duszczuk, "Prevention of Stick-Stip Tearing of a Duralcan AA6061-Matrix Composite During Extrusion", *Journal of Materials Science Letters*, 1998, **17**(19): 1617-1619.
152. Z. Zhang, X. G. Chen, and A. Charette, "Particle Distribution and Interfacial Reactions of Al-7%Si-10%B₄C Die Casting Composite", *Journal of Materials Science*, 2007, **42**(17): 7354-7362.
153. A. Mortensen, J. A. Cornie, and M. C. Flemings, "Solidification Processing of Metal-Matrix Composites", *Journal of Metals*, 1988, **40**(2): 12-19.
154. R. Asthana, "Interfaces in Cast Composites", in *Solidification Processing of Reinforced Metals*. 1998, Zurich-Uetikon: Transtec Publications Ltd. pp. 301-350.
155. F. Delannay, L. Froyen, and A. Deruyttere, "The Wetting of Solids by Molten Metals and Its Relation to the Preparation of Metal-Matrix Composites", *Journal of Materials Science*, 1987, **22**(1): 1-16.

156. D. C. Halverson, A. J. Pyzik, I. A. Aksay, and W. E. Snowden, "Processing of Boron Carbide-Aluminum Composites", *Journal of the American Ceramic Society*, 1989, **72**(5): 775-780.
157. Q. L. Lin, P. Shen, F. Qiu, D. Zhang, and Q. C. Jiang, "Wetting of Polycrystalline B₄C by Molten Al at 1173–1473 K", *Scripta Materialia*, 2009, **60**(11): 960-963.
158. C. R. Manning and T. B. Gurganus, "Wetting of Binary Aluminum Alloys in Contact with Be, B₄C, and Graphite", *Journal of the American Ceramic Society*, 1969, **52**(3): 115-118.
159. A. R. Kennedy and B. Brampton, "The Reactive Wetting and Incorporation of B₄C Particles into Molten Aluminium", *Scripta Materialia*, 2001, **44**(7): 1077-1082.
160. Z. Zhang, K. Fortin, A. Charette, X.-G. Chen, "Effect of Titanium on Castability of Al-B₄C Composites", in *Aluminium Alloys: Their Physical and Mechanical Properties (ICAA 11)*, J. Hirsch, G. Gottstein, B. Skrotzki, Eds. 2008, Aachen, Germany: Wiley-VCH pp. 434-440.
161. C. T. Mutale, W. J. Krafick, and D. A. Weirauch, "Direct Observation of Wetting and Spreading of Molten Aluminum on TiB₂ in the Presence of a Molten Flux from the Aluminum Melting Point up to 1033 K (760 Degrees C)", *Metallurgical and Materials Transactions B*, 2010, **41**(6): 1368-1374.
162. D. A. Weirauch, W. J. Krafick, G. Ackart, and P. D. Ownby, "The Wettability of Titanium Diboride by Molten Aluminum Drops", *Journal of Materials Science*, 2005, **40**(9-10): 2301-2306.
163. M. Sarikaya, T. Laoui, D. L. Milius, and I. A. Aksay, "Identification of a New Phase in the Al-B-C Ternary by High-Resolution Transmission Electron Microscopy", in *45th Annual Meeting of the Electron Microscopy Society of America*, G. W. Bailey, Editor. 1987, San Francisco Press: San Francisco, CA. pp. 168-169.
164. A. J. Pyzik and D. R. Beaman, "Al-B-C Phase Development and Effects on Mechanical-Properties of B₄C/Al-Derived Composites", *Journal of the American Ceramic Society*, 1995, **78**(2): 305-312.

165. J. C. Viala, G. Gonzales, and J. Bouix, "Composition and Lattice Parameters of a New Aluminium-Rich Borocarbide", *Journal of Materials Science Letters*, 1992, **11**(10): 711-714.
166. J. C. Viala, F. Bosselet, V. Laurent, and Y. Lepetitcorps, "Mechanism and Kinetics of the Chemical Interaction between Liquid Aluminium and Silicon-Carbide Single Crystals", *Journal of Materials Science*, 1993, **28**(19): 5301-5312.
167. J. C. Viala, "Interface Chemistry of Aluminium/Refractory Carbide Couples", in *Proc. 41st Annual Conference of Metallurgists of CIM*, R. A. L. Drew, M.D. Pugh, M. Brochu, Editor. 2002: Montréal, Québec, Canada. pp. 63-78.
168. M. Kouzeli, C. San Marchi, and A. Mortensen, "Effect of Reaction on the Tensile Behavior of Infiltrated Boron Carbide-Aluminum Composites", *Materials Science and Engineering A*, 2002, **337**(1-2): 264-273.
169. G. Arslan, F. Kara, and S. Turan, "Quantitative X-Ray Diffraction Analysis of Reactive Infiltrated Boron Carbide-Aluminium Composites", *Journal of the European Ceramic Society*, 2003, **23**(8): 1243-1255.
170. P. Rogl, H. Bittermann, and H. Duschaneck, "Boron - Carbon -Titanium", in *Ternary Alloy Systems Phase Diagrams, Crystallographic and Thermodynamic Data*, G. Effenberg and S. Ilyenko, Editors. 2006, Kempten: Springer. pp.68-89.
171. W. B. Johnson, A. S. Nagelberg, and E. Breval, "Kinetics of Formation of a Platelet-Reinforced Ceramic Composite Prepared by the Directed Reaction of Zirconium with Boron Carbide", *Journal of the American Ceramic Society*, 1991, **74**(9): 2093-2101.
172. W. B. Johnson, T. D. Claar, and G. H. Schiroky, "Preparation and Processing of Platelet-Reinforced Ceramics by the Directed Reaction of Zirconium with Boron Carbide", in *A Collection of Papers Presented at the 13th Annual Conference on Composites and Advanced Ceramic Materials, Part 1 of 2: Ceramic Engineering and Science Proceedings*, J. B. Wachtman, Ed. 1989, Hoboken, NJ, United States: John Wiley & Sons, Inc. pp. 588-598.

173. G. J. Zhang, M. Ando, J. F. Yang, T. Ohji, and S. Kanzaki, "Boron Carbide and Nitride as Reactants for *in-situ* Synthesis of Boride-Containing Ceramic Composites", *Journal of the European Ceramic Society*, 2004, **24**: 171-178.
174. G. Arslan, F. Kara, and S. Turan, "Reaction Model for the Boron Carbide/Aluminium System", in *Euro Ceramics VIII, Pts 1-3*. 2004, Zurich-Uetikon: Trans Tech Publications Ltd. pp. 1059-1062.
175. X. G. Chen, M. da Silva, P. Gougeon, and L. St-Georges, "Microstructure and Mechanical Properties of Friction Stir Welded AA6063-B₄C Metal Matrix Composites", *Materials Science and Engineering A*, 2009, **518**(1-2): 174-184.
176. A. Machiels and R. Lambert, "Handbook of Neutron Absorber Materials". 2006, Electric Power Research Institute.
177. L. T. Jiang, G. H. Wu, D. L. Sun, Q. Zhang, J. F. Chen, and N. Kouno, "Microstructure and Mechanical Behavior of Sub-Micro Particulate-Reinforced Al Matrix Composites", *Journal of Materials Science Letters*, 2002, **21**(8): 609-611.
178. H. Zhang, K. T. Ramesh, and E. S. C. Chin, "High Strain Rate Response of Aluminum 6092/B₄C Composites", *Materials Science and Engineering A*, 2004, **384**(1-2): 26-34.
179. S. Ghosh, S. K. Naskar, and A. Basumallick, "Effect of Hot Rolling on the Properties of *in Situ* Ti-Aluminide and Alumina-Reinforced Aluminum Matrix Composite", *Materials and Manufacturing Processes*, 2007, **22**(5-6): 683-686.
180. W. M. Zhong, G. Lesperance, and M. Suery, "Effect of Thermomechanical Processing on the Microstructure and Mechanical Properties of Al-Mg (5083)/SiCp and Al-Mg (5083)/Al₂O₃p Composites. Part 2: Tensile Properties at Different Temperatures", *Materials Science and Engineering A*, 1996, **214**(1-2): 93-103.
181. T. M. Lillo, "Enhancing Ductility of Al6061+10 wt.% B₄C through Equal-Channel Angular Extrusion Processing", *Materials Science and Engineering A*, 2005, **410**: 443-446.

182. C. J. Simensen, "Comments on the Solubility of Carbon in Molten Aluminum", *Metallurgical and Materials Transactions A*, 1989, **20**(1): 191-191.
183. M. E. van Dalen, D. N. Seidman, and D. C. Dunand, "Creep- and Coarsening Properties of Al-0.06 at.% Sc-0.06 at.% Ti at 300-450 °C", *Acta Materialia*, 2008, **56**(16): 4369-4377.
184. S. Otani and Y. Ishizawa, "Preparation of ZrB₂ Single Crystals by the Floating Zone Method", *Journal of Crystal Growth*, 1996, **165**(3): 319-322.
185. G. Levchenko, A. Lyashchenk, V. Baumerb, A. Evdokimov, V. Filippova, Y. Paderno, *et al.*, "Preparation and Some Properties of ScB₂ Single Crystals", *Journal of Solid State Chemistry*, 2006, **179**: 2949-2953.
186. T. F. Morgeneyer, M. J. Starink, S. C. Wang, and I. Sinclair, "Quench Sensitivity of Toughness in an Al Alloy: Direct Observation and Analysis of Failure Initiation at the Precipitate-Free Zone", *Acta Materialia*, 2008, **56**(12): 2872-2884.
187. A. Tolley, D. Mitlin, V. Radmilovic, and U. Dahmen, "Transmission Electron Microscopy Analysis of Grain Boundary Precipitate-Free-Zones (PFZs) in an AlCuSiGe Alloy", *Materials Science and Engineering A*, 2005, **412**(1-2): 204-213.
188. K. E. Knipling, D. C. Dunand, and D. N. Seidman, "Precipitation Evolution in Al-Zr and Al-Zr-Ti Alloys During Isothermal Aging at 375-425 °C", *Acta Materialia*, 2008, **56**(1): 114-127.
189. "Thermo-Calc Version 5", Thermo-Calc software AB. 2008: Sweden.
190. A. K. Lohar, B. Mondal, D. Rafaja, V. Klemm, and S. C. Panigrahi, "Microstructural Investigations on As-Cast and Annealed Al-Sc and Al-Sc-Zr Alloys", *Materials Characterization*, 2009, **60**(11): 1387-1394.
191. R. U. Vaidya and A. K. Zurek, "Effect of the Matrix Ageing Conditions on the Low Strain Rate Response of a B₄C Particle Reinforced 6061 Aluminium Matrix Composite", *Journal of Materials Science Letters*, 1996, **15**(5): 385-387.

192. H. J. Frost and M. F. Ashby, *Deformation-Mechanism Maps: The Plasticity and Creep of Metals and Ceramics*. 1982, New York: Pergamon Press.
193. R. W. Hyland and R. C. Stiffler, "Determination of the Elastic Constants of Polycrystalline Al_3Sc ", *Scripta Metallurgica*, 1991, **25**(2): 473-477.
194. E. P. George, J. A. Horton, W. D. Porter, and J. H. Schneibel, "Brittle Cleavage of L_{12} Trialuminides", *Journal of Materials Research*, 1990, **5**(8): 1639-1648.
195. C. L. Fu, "Electronic, Elastic, and Fracture Properties of Trialuminide Alloys - Al_3Sc and Al_3Ti ", *Journal of Materials Research*, 1990, **5**(5): 971-979.
196. K. Fukunaga, T. Shouji, and Y. Miura, "Temperature Dependence of Dislocation Structure of L_{12} - Al_3Sc ", *Materials Science and Engineering A*, 1997, **240**: 202-205.
197. D. Tabor, "The Physical Meaning of Indentation and Scratch Hardness", *British Journal of Applied Physics*, 1956, **7**(5): 159-166.
198. M. J. Starink, P. Wang, I. Sinclair, and P. J. Gregson, "Microstructure and Strengthening of Al-Li-Cu-Mg Alloys and MMCs: II. Modelling of Yield Strength", *Acta Mater.*, 1999, **47**(14): 3855-3868.
199. M. J. Hadianfard, Y. W. Mai, and J. C. Healy, "Effect of Ceramic Reinforcement on the Aging Behavior of an Aluminum-Alloy", *Journal of Materials Science*, 1993, **28**(13): 3665-3669.
200. L. L. Mishnaevsky, "Functionally Gradient Metal Matrix Composites: Numerical Analysis of the Microstructure-Strength Relationships", *Composites Science and Technology*, 2006, **66**(11-12): 1873-1887.
201. J. D. Robson, "A New Model for Prediction of Dispersoid Precipitation in Aluminium Alloys Containing Zirconium and Scandium", *Acta Mater.*, 2004, **52**(6): 1409-1421.

202. Y. S. Sato, M. Urata, H. Kokawa, and K. Ikeda, "Hall-Petch Relationship in Friction Stir Welds of Equal Channel Angular-Pressed Aluminium Alloys", *Materials Science and Engineering A*, 2003, **354**(1-2): 298-305.
203. T. Shanmugasundaram, M. Heilmaier, B. S. Murty, and V. S. Sarma, "On the Hall-Petch Relationship in a Nanostructured Al-Cu Alloy", *Materials Science and Engineering A*, 2010, **527**(29-30): 7821-7825.
204. N. Hansen, "Effect of Grain-Size and Strain on Tensile Flow-Stress of Aluminum at Room-Temperature", *Acta. Mater.*, 1977, **25**(8): 863-869.
205. G. E. Totten and D. S. MacKenzie, *Handbook of Aluminum Vol. 1 Physical Metallurgy and Process*. 2003, New York; Basel: M. Dekker. pp. 263-269.
206. S. M. Lee, *Handbook of Composite Reinforcements*. 1992, Hoboken: John Wiley & Sons, Incorporated. pp. 377-390.
207. D. J. Lloyd, "Particle-Reinforced Aluminum and Magnesium Matrix Composites", *International Materials Reviews*, 1994, **39**(1): 1-23.
208. M. S. Kaiser, S. Datta, A. Roychowdhury, and M. K. Banerjee, "Age Hardening Behavior of Wrought Al-Mg-Sc Alloy", *Materials and Manufacturing Processes*, 2008, **23**(1): 74-81.
209. Z. G. Chen, S. P. Ringer, Z. Q. Zheng, and J. Zhong, "Microstructural Evolution in Al-Sc and Al-Sc-Zr Alloys", in *2006 BIMW: 2006 Beijing International Materials Week, Pts 1-4 - Magnesium - Aluminium Materials - Aerospace Materials - Superconducting and Functional Materials*, S. Long, et al., Eds. 2007, Stafa-Zurich: Trans Tech Publications Ltd. pp. 629-632.
210. J. P. Hirth, "Chapter 20 . Dislocations", in *Physical Metallurgy*, R. W. Cahn and P. Haasen, Editors. 1996, Amsterdam: Elsevier Science. pp. 1863-1869.
211. K. K. Chawla, "Metal Matrix Composite", in *Materials Science and Technology : A Comprehensive Treatment Vol.13: Structure and Properties of Composites*, R. W. Cahn, P. Haasen, E. J. Kramer, and T.-W. Chou, Eds. 1993, Weinheim; Cambridge: VCH. pp. 158-159.